FIBER OPTIC SENSORS FOR *IN SITU* MONITORING DURING THERMAL ABLATION OF TUMORS

Madina Jelbuldina

A thesis submitted in partial fulfilment of the requirement of
Nazarbayev University for the degree of
Doctor of Philosophy in Science, Engineering and Technology

July 2021

ABSTRACT

High-temperature tumor ablation, or hyperthermia, is a minimally invasive therapy applied to treat benign and malignant tumors in different organs, most commonly for small and mid-size hepatic tumors.

The modern clinical standards determine 60 °C as a threshold for the almost immediate thermal coagulation of biological tissues. In order to perform the procedure effectively and avoid burning of healthy tissue, the limitations of ablation procedure have to be overcome. The limitations are related to incomplete ablation, the lack of the real time control of the procedure and inability to treat large size tumors. Real-time monitoring of the temperature dose within the target zone provides information about the amount of damaged tissue, hence allowing a clinician to regulate TA settings and to control procedural outcomes.

In this work two technological solutions is proposed to overcome the limitations of TA: (1) real-time detection of the temperature profiles *in situ* by means of fiber optic sensors that offer significant advantages over conventional thermometry techniques – thermocouples and imaging; (2) nanoparticles introduced *in situ*, which can mediate the thermal treatment by stabilizing and modifying the thermal, electrical, and optical properties of the tissue and increase the size of treatable tumors.

The overall goal of the thesis was to develop fiber optic based sensing for the multi-point real time temperature monitoring during thermal ablation.

This thesis presents a comparative study of sensing performance of 3 fiber optic sensing technologies, for the application of RF ablation. Temperature distribution during HIFU thermal treatment is performed *ex vivo* on a sample of breast fibroadenoma with the help of FBG sensors.

Next goal is to investigate the effect of nanoparticles on the outcomes of *ex vivo* TA with *in-situ* thermal profiling by means of fiber optic sensors. FBG based sensory system was implemented to investigate the effects of magnetite (Fe_3O_4) nanoparticles with 2 mg/mL and 5 mg/mL concentrations on RFA and MWA procedures. Results are presented in the forms of thermal

maps, reporting the extension of lethal 60 °C isotherm by 20% for MWA, and by 60% for RFA.

The work presents results on thermal profiling by means of non-standard optical fibers, such as polymer fibers and fibers with enhanced scattering profile. Sensing performance of the chirped fiber Bragg grating fabricated on microstructured polymer optical fiber is investigated and validated during *ex vivo* RF ablation.

Finally, the thesis reports a novel setup based on MgO doped optical fibers that provides high resolution two dimensional temperature monitoring of thermal ablation. The setup utilizes specialty optical fibers with enhanced scattering profile (around 40 dB with respect to SMF) and allows for the OBR/OFDR interrogation of multiple fibers with a single scan. The proposed multiplexing configuration is validated in *ex vivo* laser ablation of liver phantom. Results of temperature measurements are two-dimensional thermal maps exhibiting high spatial resolution of 2.5 mm.

CONTENTS

LIST OF TABLES

LIST OF FIGURES

Figure 6.8 View of the laser beam focused on the liver phantom and the positioning of 4 MgO-doped fibers during LA (left); photo of the ablated tissue with 4 fibers in parallel, the distance between fibers is 5 mm.

Figure 6.9 Relative lengths of SMF extenders spliced to MgO-doped fibers

Figure 6.10 Two-dimensional thermal maps reporting temperature on the XY plane for different elapsed time (20 s, 30 s, 50 s, 70 s, 100 s, and 120 s).

Figure 6.11 Photographic image of the phantom after performing two laser ablations: with and with no MNPs.

Figure 6.12 Two-dimensional thermal maps, reporting temperature distribution on the XY plane for different elapsed time (30 s, 50 s, 70 s, and 100 s). **Top row** – pristine ablation (no NPs), **bottom row** - with injected MNPs solution. The plain considered is 15×40 mm, with 4 sensing elements spaced 5 mm on Y axis.

LIST OF ABBREVIATIONS

AFM	Atomic force microscopy
BDK	Benzyl dimethyl ketal
CFBG	Chirped FBG
CT	Computer tomography
DTG	Draw tower grating
EBF	Enhanced backscattering fibers
EM	Electromagnetic
***et al*.**	*lat*. et alii; meaning “and others”
FBG	Fiber Bragg grating
FDA	United States Food and Drug Administration
HCC	Hepatocellular carcinoma
HIFU	High intensity focused ultrasound
LA	Laser ablation
MNPs	Magnetite nanoparticles
MRI	Magnetic resonance imaging
MWA	Microwave ablation
NA	Numerical aperture
Nd:YAG	Neodymium-doped yttrium aluminum garnet
NPs	Nanoparticles
OBR	Optical backscatter reflectometer
OFDR	Optical frequency-domain reflectometry
OTDR	Optical time domain reflectometer
PMMA	Polymethyl methacrylate
POF	Polymer optical fibers
RFA	Radiofrequency ablation
SEM	Scanning electron microscope
SMF	Single mode fiber

TA	Thermal ablation
TC	Thermocouple
US	Ultrasound
WDM	Wavelength division multiplexing
XRD	X-ray diffraction analysis

AUTHOR'S DECLARATION

I hereby declare that the research presented in this thesis is the original work of the author, and that all sources used in researching it are fully acknowledged and all quotations properly identified. The thesis has not been previously submitted to this or any other university for a degree.

ACKNOWLEDGEMENT

I would like to express my sincere gratitude to my supervisor, Prof Daniele Tosi for supporting me with invaluable advice and positive attitude, and always encouraging me to do research. I'm thankful to School of Engineering and Digital science of Nazarbayev University, for their financial support and research facilities.

During my PhD study it was a great pleasure to work with great researches and colleagues, who became my friends: Takhmina Ayupova, Marzhan Sypabekova, Madina Shaimerdenova, Zhannat Ashikbayeva. I would especially like to thank Sanzhar Korganbayev, who shared his experience with me and was my lab buddy during three years, and Alina Korobeynik, for the synthesis of nanoparticles. I'm very thankful to Aliya Bekmurzayeva, Marzhan Sypabekova, for always being helpful.

I extend my gratitude to all former and current members of Prof Daniele's group, namely Prof Carlo Molardi, Sultan Sovetov, Aizhan Issatayeva, Aidana Beisenova, Kanat Dukenbayev (for helping with AFM measurements). I'm very thankful to our collaborators, namely Rui Min, Carlos Marques (fabrication of polymer CFBG), Zhazira Seidagaliyeva (clinical HIFU), Wilfried Blanc (fabrication of MgO-doped optical fibers), Alina Korobeynik (synthesis of nanoparticles) and co-supervisors (Zhandos Utegulov and Guido Perrone).

Thank you to Dr. Luis Rojas for improving our PhD program, it would not be possible to succeed in the program without your constant support and advice.

On a more personal level, I'm grateful to my friends for making these five years an interesting and exciting journey: Kamilya, Gulden, Bagda, Asem, Damira, Aigerim, Ainura.

CHAPTER 1

Introduction

1.1 Motivation and background

Among different cancer cure procedures, surgical resection remains the only option to the patients diagnosed with primary and secondary hepatic tumours, however very limited patients would be recommended to such a procedure [5], [6]. The obstructed access to the tumor, and associated with it incomplete resection, as well as invasiveness of the procedure, and frequent lethal cases motivate clinicians to utilize alternative tumor treatments.

Treatment of tumors with high temperatures has been introduced into medical practice more than a century ago, but only starting from 1980s ablation techniques consolidated into an independent technology to cure benign and malignant tumors [1]. Since then, energy-based ablation has been improved and extended its applications thanks to development of laparoscopic medical devices and imaging techniques [7], [8].

Interstitial thermal ablative techniques are currently performed in medical practice as a minimally-invasive alternative to traditional surgery in the treatment of benign and malignant tumors. Nowadays, percutaneous thermal ablation, or thermotherapy, is primarily used for the treatment of small, unresectable tumours, including liver [9], [10], kidney, lung and bone cancers [11], as well as soft-tissue tumours of breast [12], [13], adrenal glands, and head.

Being a minimally invasive technology, thermal ablation has demonstrated more favorable outcomes compared to surgical treatment [14]. The main advantages of thermal coagulation therapies are possibility to treat patients who cannot have surgery: elderly people, patients with health issues, or patients who have multiple tumors of small size. Other important advantages must be mentioned, such as less injury of the surrounding healthy tissue, lower morbidity rates, lower costs and shorter recovery period [15].

The term thermal ablation applies to the variety of treatments utilizing cooling or heating tumors within certain temperature ranges. Different types of cells are not equally susceptible to extreme temperatures, however, temperatures below −40°C and above 60°C are considered cytotoxic for most types of tissues [16]. Several types of energy sources are applied, such as radiofrequency (RF) current, microwave, laser, ultrasound and thermal conduction based devices. The most widely used thermal techniques in modern clinical practice are radiofrequency ablation (RFA) and microwave ablation (MWA), which employ high temperatures to induce cell necrosis, as well as cryoablation, that affects tumor through cooling down the tissue to low temperatures.

RFA technique has gained popularity due to its relative simplicity and the possibility to achieve large ablative lesions (up to 4-6 cm). This approach utilizes energy produced by RF generator and is mostly used in the treatment of hepatic tumors [17]. The simple configuration utilizes a percutaneous RF needle positioned into the target tissue, and a passive electrode, which is placed on the patient's skin [18]. Similar to RFA, MWA relies on the use of electromagnetic waves to produce heat up to 100 °C and higher. Heat is transferred into the target region through a microwave antenna. The main advantage of MWA over RFA is the possibility of treatment tissues with higher impedance like lung and bone [7]. The most common medical application of MWA is ablation of hepatocellular carcinoma [19], [20].

The principle of recently introduced therapies, like laser ablation and high-intensity focused ultrasound (HIFU) is overall similar to other hyperthermia methods, but are less common and not so well studied, as RFA or MWA. Among all high-temperature modalities the only non-invasive technique is HIFU, since it utilizes ultrasound waves, so no device has to be inserted into patient's body [21]. These acoustic waves are focused then in the specific target region to elevate local temperatures up to 60 °C, which causes coagulative necrosis [22]. Laser ablation (LA) generates electromagnetic heating, as do RFA and MWA, with the advantage of laser precision and efficiency during laser ablation. LA devices consist of a solid-state laser or fiber laser, coupled into optical fiber, and positioned in contact with the tissue [23], [24]. Limitations of this modality are related to light scattering and

absorption, so the ablation lesions are typically small and don't exceed 2 cm^2. LA is used often for thyroid and brain tumor treatments, and its performance is substantially dependent upon the absorption coefficient of the tissue [25], [26].

According to the semi-empirical equations derived by Sapareto et al. cell damage during hyperthermia is strongly related not only to temperature increment, but to the exposure time [27]. The proposed concept has been mathematically formulated in the thermal dose (TD) relationships via the Arrhenius rate analysis [28]. TD relationships were applied to different cells and tissues and it was shown that the rate of heat-induced cell death is almost linearly related to exposition time and exponentially dependent on the temperature increment (within specific temperature ranges) [29]. In order to quantify the amount of thermal damage, in 1984 Sapareto and Dewey [22] introduced the unit of thermal dose in the form of cumulative equivalent minutes at 43 °C (CEM43°C or t_{43}). Although the overall damage to tissue depends on tissue sensitivity, which has variations across species and different tissues and organs, as well as temperature and exposure time, multiple experiments revealed the breakpoint in the rate of cell death to be around 43 °C [30]. The application of thermal dose and thermal damage values have been validated for different temperature ranges: thermal doses of 120–240 min at 43 °C generate considerable tissue necrosis, but the sensitivity between tissue types is variable. A lethal temperature threshold was estimated around 50-55 °C for short treatment times (less than 5 min) based on different methodological approaches, which was consistent with the TD concept [31]. Irreversible damage to vital compartments of cells occur at temperatures as high as 60 °C and is accompanied with almost immediate tissue coagulation. By reaching 100 °C and above, the tissue due to its mostly watery content, undergoes vaporization and carbonization. A useful diagram (**Figure 1.1**) demonstrates stages of thermal injury of the tissue induced by temperatures higher than body temperature [32]. For successful ablation, the tissue temperature should be maintained in the ideal range to ablate tumor tissue adequately and avoid carbonization around the tip of the electrode due to excessive heating. To achieve this goal, an accurate temperature monitoring is necessary in situ throughout the course of ablation.

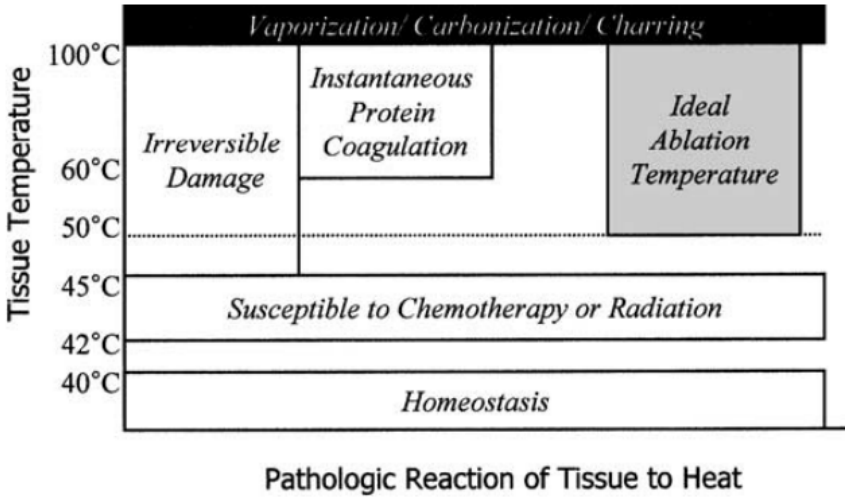

Figure 1.1 Biological response of the tissue to thermal effects. Adopted from [32].

In order to perform the TA procedure in a most efficient way, a combination of several factors have to be achieved. First is related to accurate positioning of the applicator inside the tumor, that is achieved through localization of the tumor and identification of its contours [33]. Next, the clinical settings of the device, such as power, duration, the amount of energy, should be adjusted for each patient not only prior to the ablation but throughout the course as well. Such a control is impossible without real time monitoring of the temperature dose within the target region. However, the current ablation technologies lack accurate real time monitoring, and this issue impedes a full clinical integration of thermal therapies [17]. This limitation is caused by the fact that precise temperature data is missing during ablation therapy. Temperature increase is a function of the tissue properties, such as thermal and electrical conductivity, absorption coefficients, and blood flow, which vary from patient to patient and even within a single organ [34]. The effects of blood flow are more pronounced over the longer duration of ablation because of the heat sink effect and the local variations in perfusion [35].

Thus, there is a high demand in accurate temperature profiling and real time thermal mapping as this will serve the goal of overcoming technological limitations of hyperthermic procedures through performing several tasks:

i) Estimate the amount of energy delivered to the treated area,

ii) Determine the volume of tissue that was coagulated;

iii) Based on the thermal maps provide the clinician data to adjust the settings of the ablation and/or terminate the procedure [36]

iv) Avoid damage to structures adjacent to the target area.

The appropriate temperature monitoring technique should meet the following requirements:

- Biocompatibility with human body;
- Minimal invasiveness;
- Compatibility with ablation tools and other medical devices (generators, applicators etc.);
- Appropriate spatial and temporal resolution, and
- Sufficient temperature accuracy.

Several temperature measurement methodologies are applied and studied recently to guide energy-based treatments in research, and more recently in clinical practice. These approaches are divided into thermocouples and imaging-based modalities (magnetic resonance imaging (MRI)-based techniques, ultrasound (US) imaging and X-ray computer tomography (CT) imaging modalities).

Contact-type temperature sensors have to be placed into the target tissue, usually in the way when sensors are attached to or embedded in the percutaneous ablation RF or MWA applicators, and are inexpensive modality providing relatively good accuracy, about 1 °C. Thermocouples consist of two metallic wires, and commercially available systems are presented in the form of single sensor or multisensory thermistor-based or thermocouple-based systems. Despite their low cost, significant drawbacks of thermocouples are related to high thermal conductivity of metallic wires which causes undesirable heating of the sensor itself. Extra heating leads to incorrectness of temperature readings. The measurements are also limited in space (within the closest proximity to the RF or MWA needle), as well as in number of measuring points. It is not possible to obtain two- or three-dimensional temperature distribution based on the thermocouples systems.

MRI is considered a standard thermal monitoring technology used during TA treatments and is the only FDA approved modality for non-invasive thermal ablation monitoring [36], [37]. Despite high resolution of MRI thermometry and the possibility of obtaining a 3D temperature map, significant drawbacks

related to MRI-based techniques are related to motion sensitivity and associated with it image distortions; non-compatibility with EM fields, meaning that most TA devices cannot be placed in the MR scanner. Requirements of high strength magnetic field and high costs of the equipment are also considered as disadvantages.

Another imaging modality commonly used for image guided ablation is ultrasound. The benefits of ultrasonic systems are their high temporal resolution, their availability, and their low cost. Still, ultrasound suffers from significant disadvantages, which include inferior image quality compared to MRI and CT, and limitations which arise from inability to image and treat with HIFU targets located behind overlying bones or structures containing gas, which obstruct the ultrasonic waves [38], [39].

X-ray CT, on the other hand, is a widely available imaging modality that offers high temporal resolution combined with high spatial resolution. It is substantially less expensive than MRI and provides images which are superior to ultrasound. Moreover, it can also image the brain and lungs, which ultrasound cannot, and does not impose any restrictions on the ablation equipment located within its vicinity as MRI does. Hence, it can potentially be utilized as a quantitative method for non-invasive monitoring of thermal ablation.

In relation to thermal ablation procedures, CT technique has been applied as a temperature monitoring tool during *ex vivo* RFA [40], [41], [40] and laser ablation [42], [43]. Variations of CT Hounsfield Unit with temperature as well as the effect of the tissue shrinking during *ex vivo* MWA was analyzed via CT imaging on the porcine phantoms [8], [44], [45]. All the experiments required a phantom to be placed in PMMA box [45] to reduce CT imaging artefacts, which is significant limitation for the real practical applications. Several investigations were focused on ex vivo HIFU ablation [46]. Brace et al. performed a comparative study of RFA and MWA on *in vivo* swine lungs, but the problem of high radiation from X-ray presents another limitation of CT thermometry [47].

Fiber optic sensors (FOSs) thanks to their exceptional characteristics are getting interest for the sensing applications in biomedical procedures. Made up of silica, FOSs are biocompatible and almost inert to most of the chemicals

[48], [49]. Due to the small diameter, around 100-200 microns, FOSs can be encapsulated into needles, flexible or semiflexible catheters and other surgical instruments [50]. Other important property is immunity to electromagnetic fields resulting in compatibility with MRI environment [51], and possibility to fabricate high-temperature resistant sensors. Fiber Bragg gratings (FBGs) have been reported as for multi-point temperature sensors during LA [52] as well as RFA, and MWA [53]. In addition, FBG arrays have been demonstrated to detect two dimensional thermal patterns of ablation procedures through wavelength-division multiplexing [54].

Moreover, chirped FBG (CFBG), particularly a linearly chirped FBG, has been recently used for biomedical applications in thermal ablation [3]. Its main advantage over a standard FBG array is the possibility for not only temporally but also spatially resolved measurements with a resolution as high as one millimeter over the grating length [16]. On the other hand, data analysis is associated with a more complex and time-consuming demodulation procedure [15, 16]. Recent works have been focused on developing quasi-distributed sensor systems [55] to achieve spatially resolved temperature sensing in radiofrequency ablation (RFA).

1.2 Objectives of the thesis

The overall goal of the thesis was to develop fiber optic based sensing for the multi-point real time temperature monitoring during thermal ablation. To achieve this goal, it has been divided into the following objectives:

1. Develop the FOS system to investigate thermal distribution during *ex vivo* radiofrequency ablation, compare the performance of different types of optical fiber sensors.
2. Study the temperature distribution during HIFU thermal treatment performed *ex vivo* on a sample of breast fibroadenoma with the help of FBG sensors.
3. Implement FBG based sensory system to investigate the effects of magnetite (Fe_3O_4) nanoparticles on RFA and MWA procedures.

Compare the results of experiments: in absence and after injection of nanoparticles solution.

4. Study the sensing performance of the chirped fiber Bragg grating fabricated on microstructured polymer optical fiber.
5. Develop the fiber optic multiplexing setup for the distributed measurements by utilizing fibers with enhanced scattering properties
6. Perform two-dimensional temperature mapping during laser ablation on *ex vivo* porcine liver by using non-standard fibers with enhanced scattering properties.

1.3 Structure of Thesis

Together with Introduction, this Thesis is divided into seven chapters.
Chapter 2 presents the overview, biophysical and technological aspects of minimally invasive thermal ablation procedures, and the challenges associated with them. Importance of real-time accurate monitoring during thermal ablation procedures is discussed. Finally, the Chapter covers common thermometry techniques used in TA, their limitations.

Chapter 3 is dedicated to role and application of optical fibers for the real time temperature monitoring during thermal therapies. Overview of important fiber optic sensors technologies is presented. Results on temperature profiling throughout the energy-based ablation procedures, like RFA, MWA, HIFU, are presented. Chapter 3 reports a comparative study of three fiber optic sensing methods, such as FBGs, CFBG and distributed sensor.

In Chapter 4 the effect of nanoparticles to improve the outcomes of TA is studied. Heat distribution during RFA and MWA is analyzed with the fiber Bragg grating sensory system and presented in the form of thermal maps. Results of thermal mapping are reported for pristine ablation, and after injection of nanoparticles.

Chapter 5 reports a CFBG inscribed into a microstructured polymer optical fiber for the temperature sensing application.

Chapter 6 presents results of the work involving specialty fiber optic sensors for the *in situ* monitoring during laser ablation. The Chapter reports a novel multiplexing setup based on enhanced backscattering fibers for the two-dimensional thermal profiling during laser ablation.

Thesis is then commenced with a Chapter 7, Conclusion and Future perspectives, which gives an overall summary of the work described in the above chapters as well as proposes possible future directions.

1.4 Role of collaborators

In an article on thermal profiling during HIFU ablation [56], methodology was developed by Zhazira Seidagaliyeva and Daniele Tosi; a fibroadenoma sample was prepared by Zhazira Seidagaliyeva; HIFU setup and ablation was performed by Zhazira Seidagaliyeva and Turlybek Tuganbekov; data analysis was performed by Sanzhar Korganbayev, Madina Jelbuldina and Sultan Sovetov.

For the Chapter 4 related to nanoparticle-mediated thermal ablation [57], [58] conceptualization belongs to Daniele Tosi, Madina Jelbuldina and Alina Korobeynik. Design of methodology was done by Madina Jelbuldina, Sanzhar Korganbayev and Daniele Tosi. Magnetite nanoparticles synthesis was done by Alina Korobeynik. Data analysis was performed by Sanzhar Korganbayev, Madina Jelbuldina and Daniele Tosi.

For a Chapter 5, and a paper on temperature measurements with mPOF CFBG fabrication of mPOF CFBG was done by Rui Min and Carlos Marques; design of experiment and setup was developed by Sanzhar Korganbayev, Madina Jelbuldina, Daniele Tosi; data analysis was performed by Sultan Sovetov, Sanzhar Korganbayev and Daniele Tosi.

The work on two-dimensional thermal mapping by means of enhanced backscattering optical fibers reported in Chapter 6 and published in [59], [60] conceptualization belongs to Daniele Tosi and Carlo Molardi; fabrication of specialty fibers with enhanced scattering profile was performed by Wilfried Blanc; multiplexing setup was prepared by Madina Jelbuldina, Aidana Beisenova, Aizhan Issatayeva and Carlo Molardi; Laser ablation setup was

prepared by Madina Jelbuldina and Azat Abdullayev; Data analysis was performed by Sanzhar Korganbayev, Arman Aitkulov and Daniele Tosi. Formal analysis was performed by Madina Jelbuldina, Carlo Molardi and Daniele Tosi.

1.5 Research articles

1. M. Jelbuldina, A. Korobeinyk, S. Korganbayev, V.J. Inglezakis and D. Tosi, “Fiber Bragg grating based temperature profiling in ferromagnetic nanoparticles-enhanced radiofrequency ablation”. *Optical Fiber Technology*, *43*, pp.145-152 (2018).
2. M. Jelbuldina, A. Korobeinyk, S. Korganbayev, D. Tosi, K. Dukenbayev and V.J. Inglezakis, “Real-Time Temperature Monitoring in Liver During Magnetite Nanoparticle-Enhanced Microwave Ablation With Fiber Bragg Grating Sensors: Ex Vivo Analysis”, *IEEE Sensors Journal*, *18*(19), pp.8005-8011 (2018).
3. M. Jelbuldina, S. Korganbayev, Z. Seidagaliyeva, S. Sovetov, T. Tuganbekov and D. Tosi, “Fiber Bragg Grating Sensor for Temperature Monitoring During HIFU Ablation of Ex Vivo Breast Fibroadenoma”, *IEEE Sensors Letters*, *3*(8), pp.1-4 (2019).
4. Z. Ashikbayeva, A. Aitkulov, M. Jelbuldina, A. Issatayeva, A. Beisenova, C. Molardi, P. Saccomandi, W. Blanc, V.J. Inglezakis and D. Tosi, “Distributed 2D temperature sensing during nanoparticles assisted laser ablation by means of high-scattering fiber sensors”, *Scientific Reports*, *10*(1), pp.1-12 (2020).
5. S. Korganbayev, R. Min, M. Jelbuldina, X. Hu, C. Caucheteur, O. Bang, B. Ortega, C. Marques and D. Tosi “Thermal profile detection through high-sensitivity fiber optic chirped Bragg grating on microstructured PMMA fiber,” *Journal of Lightwave Technology*, *36*(20), pp.4723-4729 (2018).
6. A. Beisenova, A. Issatayeva, S. Sovetov, S. Korganbayev, M. Jelbuldina, Z. Ashikbayeva, W. Blanc, E. Schena, S. Sales, C. Molardi and D. Tosi, “Multi-fiber distributed thermal profiling of minimally

invasive thermal ablation with scattering-level multiplexing in MgO-doped fibers", *Biomedical optics express*, *10*(3), pp.1282-1296 (2019).

Conference Publications

1. M. Jelbuldina, A. Issatayeva, A. Aitkulov, S. Korganbayev, A. Beisenova, N. Kulmukhanova, D. Koshen, C. Molardi and D. Tosi, "Multi-fiber distributed temperature profiling in ex vivo magnetite nanoparticle-mediated laser tissue ablation", In *Optical Interactions with Tissue and Cells XXXI* (Vol. 11238, p. 112380H). International Society for Optics and Photonics (2020 February).
2. M. Jelbuldina, S. Korganbayev, A. Korobeinyk, V.J. Inglezakis, and D. Tosi "Temperature Profiling of ex-vivo Organs during Ferromagnetic Nanoparticles-Enhanced Radiofrequency Ablation by Fiber Bragg Grating Arrays" In *2018 40th Annual International Conference of the IEEE Engineering in Medicine and Biology Society (EMBC)* (pp. 1-4), IEEE (2018 July).
3. M. Jelbuldina, S. Korganbayev, A.V. Korobeinyk, V.J. Inglezakis and D. Tosi "Fiber Bragg grating sensors for temperature monitoring during nanoparticle-assisted microwave ablation" In *Optical Fiber Sensors* (p. WF3). Optical Society of America (2018 September).
4. A. Issatayeva, A. Beisenova, S. Sovetov, S. Korganbayev, M. Jelbuldina, Z. Ashikbayeva, W. Blanc, C. Molardi and D. Tosi, "2D temperature sensing obtained by multiplexing of optical backscattering reflectometry," In *Optical Fibers and Sensors for Medical Diagnostics and Treatment Applications XX* (Vol. 11233, p. 112330T), International Society for Optics and Photonics (February 2020).
5. A. Issatayeva, A. Beisenova, S. Sovetov, S. Korganbayev, M. Jelbuldina, Z. Ashikbayeva, W. Blanc, E. Schena, S. Sales, C. Molardi and D. Tosi, 2019, November, "Multiplexing of distributed temperature sensing achieved by nanoparticle-doped fibers," In *Optics in Health Care and Biomedical Optics IX* (Vol. 11190, p. 111900H), International Society for Optics and Photonics (November 2019).

CHAPTER 2

Temperature monitoring during thermal therapies

Chapter 2 overviews modern thermal ablation modalities, their working principle, as well as technological limitations (Section 2.1). Next, motivation for the real-time temperature monitoring during thermal therapies is discussed (Section 2.2). Section 2.2 also overviews thermometry techniques which are currently applied in clinical practice, as well as the issues related to the conventional thermometry techniques.

2.1 Minimally invasive thermal therapies

2.1.1 General ablation principles

Tumor treatment with high temperatures has been introduced into medical practice more than a century ago, but it's only in the 1980s when tumor ablation started to evolve as an independent technology to treat benign and malignant tumors. This became possible thanks to development of cross-sectional imaging techniques and laparoscopic medical devices [1]. Since then, percutaneous energy-based ablation has significantly evolved and extended its applications to treatment of various types benign and malignant tumor, including liver, kidney, lung and bone cancers, as well as soft-tissue tumours of breast, adrenal glands, and head [7], [10], [12], [61]. Nowadays, percutaneous thermal ablation is primarily used for the treatment of small, unresectable tumours or for patients who are poor surgical candidates, for instance, their overall health is weak or they have multiple tumors of small sizes.

The term *thermal ablation*, or *hyperthermia* applies to procedures which utilize cooling or heating tumors within certain temperature ranges, thus inducing lethal damage to the cancer cells. Different types of cells are not equally

susceptible to extreme temperatures, however, temperatures below −40°C and above 60°C are considered cytotoxic for most types of tissues [16].

Being a minimally invasive technology, thermal ablation has demonstrated more favorable outcomes compared to surgical treatment, and at the same time it is therapeutically effective, for example, radiofrequency ablation for the treatment of hepatic tumor [14]. The overall advantages of ablation therapies are less injury of the surrounding healthy tissue, lower morbidity rates, lower costs and shorter recovery period [15]. Besides this the real time monitoring of the procedure through imaging, and the possibility to treat patients who cannot have surgery, such as elderly people, or patients who have multiple tumors of small size. The reasons for the growing interest in energy-based modalities and their increasing use in the clinical practice are related to several factors:

a. Different types of tumours are detected at an earlier stage;
b. The number of elderly patients is increasing;
c. Energy-based ablation technology is evolving and devices are improving, for example HIFU technology, cryoablation;
d. Imaging technologies are rapidly developed and are integrated into the minimally invasive hyperthermia systems;
e. Hyperthermia can improve the outcomes of radiotherapy and chemotherapy [62], [63].

These factors promote researchers of biomedical, engineering fields to further study thermal ablation techniques and to search the methods to improve the outcomes of the procedures. The efficacy and outcomes of thermal ablation have indeed to be improved due to drawbacks associated with it, such as limits of the ablative lesions [64], making the ablation suitable only for the small and mid-size tumors, as well as imperfection of the intra-procedural temperature monitoring techniques, that will be discussed thoroughly later in this chapter.

The most widely used thermal techniques in modern clinical practice are radiofrequency ablation (RFA) and microwave ablation (MWA), which employ high temperatures to induce cell necrosis, as well as cryoablation, that affects tumor through cooling down the tissue to low temperatures. **Figure 2.1** shows the timeline of development of different image-guided TA techniques.

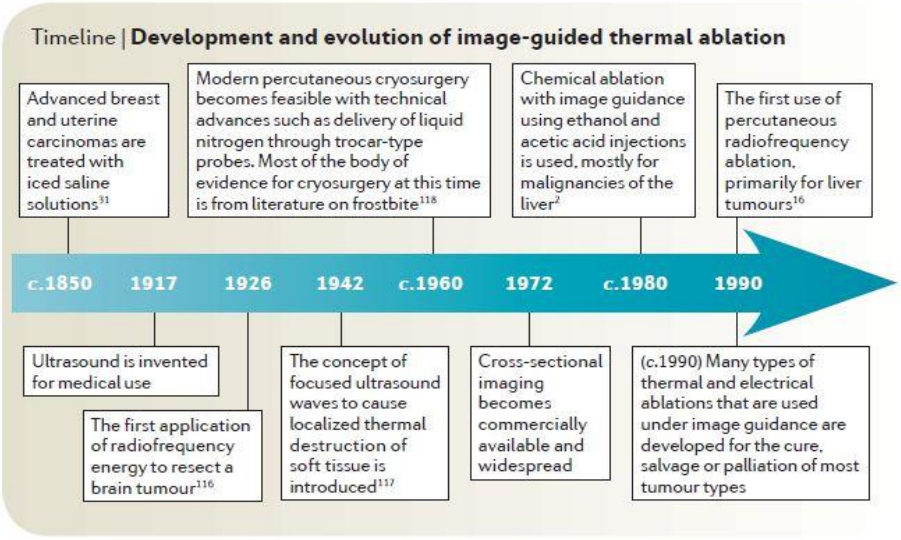

Figure 2.1 Development and evolution of image-guided thermal ablation techniques [1].

While multiple techniques provide hyperthermia therapy, they all rely on several physical principles on delivering heat energy to the body:

(i) Thermal conduction of heat, which flows from higher to lower temperature at a rate dependent on the thermal gradient and thermal properties of all contacting material.

(ii) Resistive or dielectric losses from an applied electromagnetic (EM) field. At radiofrequencies below 20 MHz, an electric potential difference between inserted and surface contacting electrodes creates an electric current. The amount of induced heat is defined by Joule law and is proportional to the tissue impedance and the electric current: $P = I^2R$.

(iii) Mechanical losses due to molecular oscillations induced by an applied ultrasound (US) acoustic wave.

Depending on the temperature range, tumor cell damage occurs through a certain mechanism. For example, increase in temperature up to 40°C will not induce a significant damage to the targeted tissue, due to the heat shock response. This is a response of the body characterized by increased blood flow that helps to prevent excess heating. Exposing the tissue to higher temperatures leads to random protein denaturation in cell nuclei and the subsequent cell death [28], [65]. Protein denaturation inside the nuclei is the predominant mechanism of the cell necrosis [66]. Applying thermal dosage of 42 °C – 46 °C for 10 minutes is sufficient to cause irreversible damage.

Temperatures as high as 60°C generally mark the lethal isotherm since above that level plasma membrane is melting which leads to instantaneous cell necrosis.

Cryotherapy, or cryoablation, on the contrary, relies on killing pathological tissues through inducing osmotic shock [67]. Cooling down the tissue to −40°C will destroy cellular metabolism.

Next sections of this Chapter are dedicated to mechanisms of each particular hyperthermia modality – RFA, MWA, HIFU and LA, as well as cryoablation. The advantages and disadvantages of the procedures as well as the areas of clinical use are also the topic of further discussion. Limitations of thermal ablation procedures are also presented. Section 2.2 covers common thermometry techniques utilized during TA, their drawbacks are discussed as well.

2.1.2 Radiofrequency ablation

Radiofrequency (RF) thermal ablation is currently being implemented as a standard treatment replacing surgical resection for the treatment of malignant hepatic lesions and hepatocellular carcinoma (HCC) [68], [69], since only 30% of patients with HCC and 20% patients with hepatic colorectal metastases (CRM) are qualified for surgical resection [70].

Percutaneous RFA system comprises a generator and one or multiple electrodes: a percutaneous metal rod which is directly placed into the target tumor tissue under the ultrasound (US) or other imaging guidance, and the grounding pad that is positioned on the patient's skin [71]. RF generator, operating typically below 1 MHz, generates electric field between two electrodes. The mechanism of tissue heating with RFA is based on resistive energy loss due to impedance of the biological tissue [33]. The RF generator acts as a voltage source, so the average power delivered can be calculated from Ohm's law: $P = V^2/Z$, where Z is the impedance of the tissue volume, adjacent to the electrode [18]. For example, liver is relatively conductive because of its high water and ion content, so it creates a low-impedance electrical current path. Conversely, aerated lung and fat have lower water and ion contents, so are associated with much higher electrical impedance. This

makes RF ablation challenging in lung since even electrically conductive tumors are surrounded by lung parenchyma [71].

The resistive heating, described by Ohm's law, leads to temperature increase and the following coagulative necrosis in the area surrounding the RF applicator tip. The heat then spreads outwards into adjacent tissue by conduction. In order to prevent the risk of tumor recurrence, it is necessary to produce the ablation lesion that extends 0.5 to 1.0 cm outside the tumor margin. Temperatures above 60 °C induce lethal cell injury, however, temperatures higher than 100 °C are less effective, due to tissue burns and vaporization of watery components, which leads to increase in the tissue impedance and therefore limits further electrical conduction through the remaining tissue [72]. Additionally, cytotoxic temperatures are difficult to maintain if the ablated tumor is near large blood vessels. This heat-sink effect is a commonly described limitation of RFA and occurs when heat that is absorbed by flowing blood or air is carried away from the area of ablation, thereby dissipating the hyperthermia and decreasing RFA efficacy; because of this, tumor tissue that is adjacent to vasculature is less susceptible to thermal damage.

Overall, RF ablation has found the greatest utility in treating small tumors (up to 3 cm diameter) in the liver and kidney. The advantage of RFA technique is the possibility to use deployable devices (umbrella or star-shaped array of deployed tines) or multiple-electrode systems to improve the efficacy of RF ablation and increase the ablated volume for medium tumors (up to 5 cm diameter). Such commercially available devices are depicted in **Figure 2.2** [73].

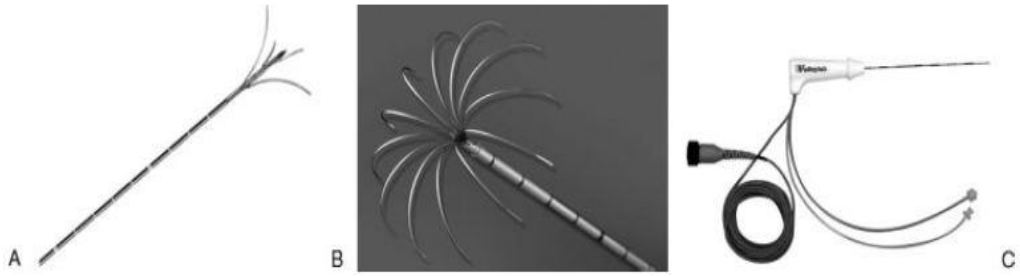

Figure 2.2 (A) 14-Gauge multitined StarBurst Talon RFA device (photo courtesy of Angio Dynamics). (B) 14-Gauge LeVeen needle showing 12 retractable electrodes

(photo courtesy of Boston Scientific). (C) 17-Gauge Cool-tip RF electrode (photo courtesy of Covidien).

2.1.3 Microwave Ablation

Microwave ablation (MWA) is a relatively newer modality that was developed in Japan [74], [75], and a common MWA system consists of a microwave generator, flexible coaxial cable, and microwave antenna. Similar to RFA, MWA relies on the use of electromagnetic energy to generate heat and to induce cell death through direct hyperthermic injury. Electromagnetic waves, usually in the range of 900–2500 MHz are delivered to the target tumor region through a percutaneous antenna. Electromagnetic (EM) field causes polar water molecules, which have weak unequal dipoles, to orient in alignment with the field [76]. High frequency oscillations of EM field induces rotative motions of water dipoles, which results in increase of the kinetic energy. Higher kinetic energy of water molecules implies temperature rise, and when sufficient temperature values are achieved, - the target tissue undergoes coagulative necrosis.

Unlike RFA, heat propagation mechanism during MWA does not rely on conduction or impedance of the tissue, which makes this technique suitable for treatment of tissues with higher impedance, like lungs and bone, and generally, more attractive than LA and RFA. Other advantages over RFA, include the ability to achieve better heating of larger tumor volumes and a lower susceptibility to heat-sink effects because higher temperatures are achieved within a shorter duration [77]. During RFA, the zone of active heating is limited to a few millimeters around the active electrode, and the remainder of the treated tissue is heated by thermal conduction. By contrast, MWA at certain frequencies can heat tissue up to 2 cm away from the antenna [18]. Multiple antennas can be connected simultaneously making possible the treatment of bigger tumors or several small tumors within the same course of ablation [77]. Among disadvantages are the system itself which is more technically complicated, and larger size of MWA cables. Moreover, the antenna is prone to overheating, so the system will require a cooling mechanism.

Modern technology allows integration of mechanisms of control into the ablation system: thermal control, field control, and wavelength control, that serve the goal of achieving a more reproducible and controlled ablation [78], [79]. Reports show utilizing MWA for the treatment of liver and renal tumor [80], and some data are also available about lung and pancreatic cancer [81], [82].

2.1.4 Laser ablation

Lasers play an important role in various medical applications related to ophthalmology, dentistry and skin treatment. The devices and systems used for laser tumor ablation are similar to those used for other clinical applications. The earliest work related to laser thermal ablation has been performed back in 1980s and was dedicated to the treatment of hepatic tumor [83]. Since then, treatment of cancer with laser has become a competitive modality applied to many types of tumors, however laser ablation is not so well studied and introduced into clinical practice like RFA or MWA [84].

During laser ablation temperature elevation and the subsequent thermal injury of the tissue is described by the mechanisms of laser-tissue interactions. Laser light interacts with various tissue components depending on the light wavelength, but most laser ablation devices operate at 800–1100 nm range to ensure better energy penetration. Such a wavelength range is explained by the presence of tissue specific chromophores inside the living cells, these chromophores absorb laser light predominantly at characteristic wavelengths 800 to 1100 nm.

A typical laser ablation system comprises a power source, laser medium, and a laser delivery fiber. In modern techniques laser delivery is performed trough a thin optical fiber and can be realized percutaneously or laparoscopically [23]. An optical fiber is introduced into a target tumor region through a needle or catheter, most commonly 13 to 15 gauge for modern quartz fibers. Diode laser (laser wavelength 980 nm) and Nd:YAG laser (working at 1064 nm) are commonly used for the hyperthermia application [85]. Laser light is energetic and is absorbed rapidly by the tissue near the applicator. This causes a rapid temperature elevation, and further heat propagates via scattering of the light and thermal conduction into adjacent tissues. The sufficient amount of energy

will induce lethal thermal injury. The amount of thermal damage during such therapy is defined by the optical properties of the target tissue [86], as well as the laser parameters, such as type of fiber applicator, laser wavelength and power.

As in case of RFA, carbonization limits the maximal zone of ablation, since the ablation lesion produced by a single applicator are not larger than 2 cm in diameter. The system utilizing multiple applicators or applicator with diffusing tip may help improve the outcome of LA [83]. External cooling may be used if the applied power is sufficient to cause applicator heating.

A significant advantage of applying laser fiber applicators is MRI compatibility, allowing for preprocedural planning and intraprocedural treatment monitoring using a variety of temperature-sensitive techniques. Clinical application of laser ablation includes treatment of hepatic tumor [23], breast carcinoma [87], benign prostatic hyperplasia, and cancer of the pancreas. In addition, modern LA systems can be incorporated with MRI and US tools to improve the safety and efficacy of the procedure through tumor localization, targeting and monitoring of the ablation [88].

2.1.5 High intensity focused ultrasound

During HIFU, through tissue as a high-energy acoustic wave [12]. HIFU transducers operate typically in the range 0.2 MHz to 3.5 MHz and deliver ultrasound energy with power densities in the range of 100–10000 $W \cdot cm^{-2}$ to the focal region. Such short but high intensity pulses induce temperature increase up to 60–95 °C within a few seconds without damaging adjacent tissues [12], [89]. The predominant mechanism of coagulative necrosis is thermal, i.e. conversion of acoustic energy into heat. In addition to thermal mechanism, cell death can be achieved through non-thermal effects, known as (boiling) histotripsy. For histotripsy, very short (micro- or millisecond long) acoustic pulses of high intensity (>5 times as high compared to thermal ablation) force bubbles in the tissue to oscillate and, subsequently, burst, causing mechanical damage to tissues at a subcellular level [89]. Currently, HIFU is used for the ablation of tumors in the liver, prostate, breast, and kidney, and benign thyroid nodules [2]. **Figure 2.3** illustrates a working principle of this technique.

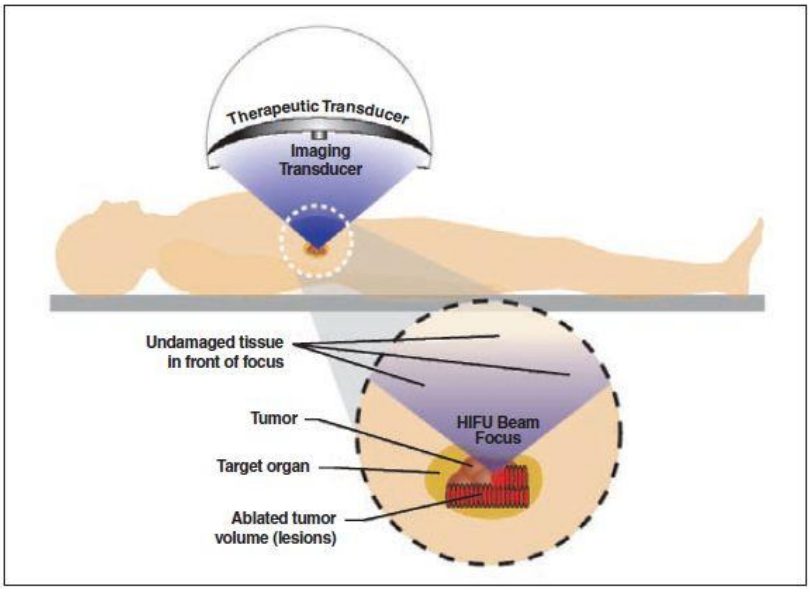

Figure 2.3 HIFU treatment of intraabdominal tumor. Adopted from [2].

The possibility to selectively damage tumor without the need for skin incision, as well as no bleeding and no radiation make HIFU an attractive option for patients with breast carcinomas [90]–[92]. Multiple clinical studies were successfully performed on HIFU treatment of breast cancer. Wu *et al.* showed complete necrosis of breast tumors of 2-4.8 cm in diameter by HIFU technique [91], [93]. Authors demonstrated a 95% five-year disease-free survival, and the cosmetic results were estimated as excellent by most of the patients. Li *et al.* reviewed 11 arms of breast cancer treatment using HIFU therapy during the period 2002-2010. The complete necrosis rates achieved with MRI-guided HIFU were 59%, while US-guided HIFU showed 96% of complete necrosis [92].

2.1.6 Cryoablation

In contrast to high temperature thermal ablation techniques, cryoablation, or cryotherapy, provides the destruction of a pathological tissues by freezing. Cooling down the tissue to −40°C will induce osmotic shock to the cells, and destroy cellular metabolism [67].

It has been used for cancers of the retina, skin, prostate, kidney, liver, breast, lung and bone [94]. This technique utilizes liquefied cryogenic gases (e.g., argon) injected inside the cryoprobe. There is a small chamber at the end of

the cryoprobe; under low pressure inside the chamber gas undergoes adiabatic expansion, resulting in a temperature drop to as low as –160°C and the formation of an iceball around the probe tip. Cell death is associated with cellular dehydration, as freezing of extracellular medium causes an osmotic gradient, cell shrinkage and distortion of the plasma membrane [95]. During the thaw, the intracellular compartment becomes hypertonic, and fluid shift causes the cell to burst [95]. Cell mortality occurs –40°C and –20°C, and studies show that this temperature needs to persist to 10 mm beyond the tumor boundary [67].

2.2 Thermometry for monitoring thermal ablation procedures

2.2.1 Introduction

In previous chapter I presented the overview of thermal ablation (TA) procedures, their working principles and limitations. In order to perform the TA procedure in a most efficient way, a combination of several factors have to be achieved. First is related to accurate positioning of the applicator inside the tumor, that is achieved through localization of the tumor and identification of its contours [33]. Next, the clinical settings of the device, such as power, duration, the amount of energy, should be adjusted for each patient not only prior to the ablation but throughout the course as well. Such a control is impossible without real time monitoring of the temperature dose within the target region. However, the current ablation technologies lack accurate real time monitoring, and this issue impedes a full clinical integration of thermal therapies [17]. This limitation is caused by the fact that precise temperature data is missing during ablation therapy. Temperature increase is a function of the tissue properties, such as thermal and electrical conductivity, absorption coefficients, and blood flow, which vary from patient to patient and even within a single organ [34]. The effects of blood flow are more pronounced over the longer duration of ablation because of the heat sink effect and the local variations in perfusion [35]. Thus, there is a high demand in accurate temperature profiling and real time thermal mapping as this will serve the goal of overcoming technological limitations of hyperthermal procedures through performing several tasks:

- Estimate the amount of energy delivered to the treated area;
- Determine the volume of tissue that was coagulated;
- Based on the thermal maps provide the clinician data to adjust the settings of the ablation and/or terminate the procedure [36]
- Avoid damage to structures adjacent to the target area.

2.2.2 Requirements for the sensors

The appropriate temperature monitoring technique should meet the following requirements:

- Biocompatibility with human body;
- Non-invasiveness;
- Compatibility with ablation tools and other medical devices (generators, applicators etc.);
- Appropriate spatial and temporal resolution, and
- Sufficient temperature accuracy.

In terms of the last two factors, it is worth noting that high-quality non-invasive thermometry implies sufficient spatial resolution and temperature accuracy for any particular type of the thermal therapy [96]. Mild temperature hyperthermia, for example, is characterized by relatively low temperature regimes of 42-44 °C, that have to be maintained stable throughout the treatment (typically, for 1-1.5 h). This type of hyperthermia aims at improving the outcomes of radiation therapy and chemotherapy, by making cancer cells more sensitive to these therapies. Mild temperature hyperthermia may be applied to a part of the body (regional perfusion, deep tissue hyperthermia) or to the whole body [17]. In this case, clinicians are looking for the temperature accuracy in the range of several tenths of a degree, while spatial and temporal resolution becomes less critical. On the contrary, thermal ablation procedures are of shorter duration (an average treatment lasts 10-20 min), and the operating temperatures reach up to 100˚C, with the most critical range of 50–60˚C necessary to achieve tumor damage. To be able to detect fast changing temperature gradients within a small target region, a temperature measuring device has to perform with high spatial and temporal resolution. For this type of thermal therapy, a spatial resolution of the perfect thermometry should be ≤1 mm, while the desirable temperature accuracy should stay in the range of

1–2˚C [97]. Regarding the temporal resolution, measurement device should provide at least 1 reading per second to ensure accurate control of the ablation procedure, furthermore, temperature data should be presented in real-time to allow the necessary adjustments of needle position, as well as settings of the ablation tool [17].

2.2.3 Contact-type temperature sensors

Several temperature measurement methodologies are applied and studied recently to guide energy-based treatments in research, and more recently in clinical practice. These approaches are divided into thermocouples and imaging-based modalities (magnetic resonance imaging (MRI)-based techniques, ultrasound (US) imaging and X-ray computer tomography (CT) imaging modalities).

Contact-type temperature sensors have to be placed into the target tissue, usually in the way when sensors are attached to or embedded in the percutaneous ablation RF or MWA applicators, and are inexpensive modality providing relatively good accuracy, about 1 °C. Thermocouples consist of two metallic wires, and commercially available systems are presented in the form of single sensor or multisensory thermistor-based or thermocouple-based systems. Despite their low cost, thermocouples cannot be suitable for all TA applications for several reasons:

- The number of measuring points are strongly limited
- Temperature measurements are performed in the closest proximity to the electrode,
- No data are collected within the rest of ablation lesion, away from the applicator
- Temperature errors due to high thermal conductivity of metallic wires which causes undesirable heating of the sensor itself.

2.2.4 Imaging based modalities

MRI is the most common imaging technique utilized temperature monitoring of TA treatments and is the only FDA approved modality for non-invasive

monitoring of thermal therapies [36], [37]. MRI is based on the relaxation of excited protons in water. MRI scanner consists of a large coil, generating magnetic field. An object is placed in a static external magnetic field inside the scanner, the spins of the protons align in one of two opposite directions: parallel or antiparallel [98]. The protons precess with a certain frequency. For a 1T scanner, a pulse frequency of 42.58 MHz is used.

There are several methods for temperature monitoring with MR, using spin-lattice relaxation time (T1), diffusion coefficients, proton resonance frequency (PRF) of tissue water, and spectroscopic imaging. The most suitable method for MR temperature monitoring during hyperthermia treatment is the PRF method because it is quantitative, sensitive, and accurate. Thermal accuracy and temporal resolution of PRF thermal imaging is excellent with an ability to detect temperature differences of 1˚C, with a temporal resolution of 1 second and a spatial resolution of 2 mm in immobile tissues [37].

Despite high resolution of MRI thermometry and the possibility of obtaining a 3D temperature map, significant drawbacks related to MRI-based techniques are:

i) the required high magnetic field strength (>1.5 T)
ii) sensitivity to any kind of motion, which limits the use of PRF in moving organs, for ex. respiratory motion
iii) the need of MR-compatible ablation devices to be operated inside the MR scanner
iv) Image distortion and artefacts resulting from metallic objects and susceptibility effects may be significant when using thermal ablation applicators.
v) MRI is a very expensive imaging modality and not widely available for interventional clinical use.

Another imaging modality utilized in clinical ablation practice is ultrasound imaging (US). US systems provide high temporal resolution, and are widely available tools. Image quality, however, cannot compete with that provided by MRI or CT, and it is not possible to image structures containing gas, which obstruct the ultrasonic waves [38], [39]. Additionally, during HIFU, microbubbles are formed around the ablated lesion, which are not part of coagulative lesion, and they cannot be distinguished by US. These

microbubbles may also preclude the accurate use of ultrasound in many scenarios.

X-ray CT, on the other hand, is a widely available imaging modality that offers high temporal resolution combined with high spatial resolution. It is substantially less expensive than MRI and provides images which are superior to ultrasound. Moreover, it can also image the brain and lungs, which ultrasound cannot, and does not impose any restrictions on the ablation equipment located within its vicinity as MRI does. Hence, it can potentially be utilized as a quantitative method for non-invasive monitoring of thermal ablation.

In relation to thermal ablation procedures, CT technique has been applied as a temperature monitoring tool during *ex vivo* RFA [40], [41], [40] and laser ablation [42], [43]. Variations of CT Hounsfield Unit with temperature as well as the effect of the tissue shrinking during *ex vivo* MWA was analyzed via CT imaging on the porcine phantoms [8], [44], [45]. All the experiments required a phantom to be placed in PMMA box [45] to reduce CT imaging artefacts, which is significant limitation for the real practical applications. Several investigations were focused on ex vivo HIFU ablation [46]. Brace et al. performed a comparative study of RFA and MWA on *in vivo* swine lungs, but the problem of high radiation from X-ray presents another limitation of CT thermometry [47]. Since CT-based thermometry is an indirect temperature measurement method, several practical limitations arise. First, thermal expansion coefficients vary widely from one patient to another, due to inhomogeneity and complexity of human tissue composition. Thus, it may be problematic to determine CT number and thermal expansion coefficients, which will affect the accuracy of temperature measurements. Another issue, associated with CT thermometry, includes a risk of prolonged exposure to radiation. To eliminate the radiation dose, low-energy X-rays and low-dose CT is applied, which, however, result in high level of Poisson noise [41].

CHAPTER 3

Fiber optic sensors for temperature monitoring during thermal ablation of tumors

In Chapter 3 advantages of the optical fiber sensors with respect to conventional thermometry techniques are discussed. The Chapter reports FBG sensor setup for the temperature profiling of *ex vivo* HIFU ablation, and the comparative study of 3 fiber optic sensing methods for the RFA monitoring is presented.
The work presented in this Chapter was published in [56].

3.1 Introduction

None of the temperature measurement techniques discussed in Section 2.2 of Chapter 2 meet all the criteria to be suitable for high quality and high accuracy real time thermometry any during TA procedures. An effective solution comes from the unique properties of fiber optic sensors (FOSs) that make them ideal candidates for physical measurements during medical procedures. Fiber optic sensors (FOSs) thanks to their exceptional characteristics are getting interest for the sensing applications in biomedical procedures. Made up of silica, FOSs are biocompatible and almost inert to most of the chemicals [48], [49]. Due to the small diameter, around 100-200 microns, FOSs can be encapsulated into needles, flexible or semiflexible catheters and other surgical instruments [50]. Other important property is immunity to electromagnetic fields resulting in compatibility with MRI environment [51], and possibility to fabricate high-temperature resistant sensors. Fiber Bragg gratings (FBGs) have been reported as for multi-point temperature sensors in laser ablation (LA) [52]; also quasi-distributed sensors [55] have been used for spatially resolved temperature sensing in radiofrequency ablation (RFA).
In addition, FBG arrays have been demonstrated to detect two dimensional thermal patterns of ablation procedures through wavelength-division multiplexing [54].

The main types of fiber optic sensors: extrinsic or hybrid (sensing takes place outside of fiber) and intrinsic or “all-fiber” sensors (sensing within a fiber). In other words, the second type relies on the properties of the fiber to transform an environmental action to modulation of spectrum passing through it (altering power, phase, polarization or guided modes) [99]–[101].

According to Kersey [100], Udd and Spillman [101], fiber optic sensors offer considerable advantages such as EMI immunity, electrically passive operation, multiplexing capabilities, high sensitivity and capability to measure in high temperatures, large bandwidth, small size and light weight [50], [101]–[103], environmental ruggedness. Therefore, the all-passive dielectric approach of optic sensors can be used in medical applications due to electrical isolation of patients and biocompatibility, according to the ISO 10993 [104] standard in use by Food and Drug Administration and the European Union. Another main advantage of fiber sensors is the fact that they can be embedded in different materials with minimal effect on the properties of the material.

One of the most interesting properties of FOS is the possibility to enclose a plurality of sensing elements in the same fiber, that allows measuring temperature (or strain) maps or profiles in space and time [3], [105]. There are two main approaches for spatially distributed sensing of different physical parameters: (1) set of spatially resolved sensing elements on the same fiber each having specific properties, and (2) distributed sensing, that does not have specifically fabricated sensing elements, but the whole fiber acts as a sensor.

The current generation of FOS embodies another significant advantage over traditional sensing technologies based on electronic sensors: rather than limiting the measurement to a single or few sensing point(s), FOS can employ multiplexed or distributed sensors to spatially resolve physical parameters such as temperature or strain [106]. In biomedical applications, Tosi *et al.* [99] identified 3 sensing technologies that can resolve temperature on a single fiber with a resolution inferior to the centimeter:

(1) Fiber Bragg Grating (FBG) arrays, which behave as a cascade of narrow-band notch filters, and were discussed in previous section of this Chapter;

(2) Chirped FBG (CFBG) that has index modulation of the core with non-constant period and behaves as a continuous array or cascade of FBGs.
(3) Optical frequency-domain reflectometry (OFDR) that interrogates distributed weak reflections occurring in the sensing fiber.
One of the most advanced implementation of OFDR is the optical backscatter reflectometry (OBR), in which the measured distributed reflections are the Rayleigh backscattering components observed in a standard fiber [107].
These sensing technologies differ in terms of cost, spatial resolution, but all report data in form of “thermal maps”, that display temperature as a function of space and time. Temperature sampling occurs both in time, which corresponds to the measurement speed, but also in space, identifying the spatial resolution that is defined as the distance between two adjacent sensing points. FBG arrays can detect with 1 cm spatial resolution, while the other techniques can approach the millimeter scale.
The most immediate medical application of temperature sensing at the millimeter scale is in the real-time monitoring of thermal ablation procedures.
As was discussed in Chapter 2, FOS have substantial advantages with respect to conventional temperature monitoring techniques, such as thermocouples and imaging, and their use of FOS in thermotherapies has been consolidated since 2014. The key asset is the possibility to use a single optical fiber to resolve a temperature distribution. For this application, the spatial resolution, accuracy, time response, and cost of the disposable element are key performance indicators of the effectiveness of the sensing methods. All the previous methods have been used for temperature sensing in thermo-therapies: FBG array is the most consolidated method, reported by Webb *et al.* in 2000 and subsequently extended more recently for RFA, MWA, and LA. OBR has been reported by Macchi *et al.* for RFA [108]. Chirped FBGs have been first reported by Tosi *et al.* in 2014, and subsequently enhanced in 2018 using a spectral reconstruction method [55], [109].
In the following sections we report FBG based setup for the real-time temperature profiling during *ex vivo* HIFU ablation (Section 3.2). Next, a comparative study of 3 fiber optic sensing technologies, FBGs, CFBG and distributed sensor for the real-time temperature profiling during RFA, is reported (Section 3.3).

3.2 Fiber Bragg gratings for temperature monitoring during HIFU ablation of *ex vivo* breast fibroadenoma

3.2.1 Introduction

High intensity focused ultrasound (HIFU) is one of the minimally invasive thermotherapies employed to treat benign and malignant tumors in soft tissues. HIFU is getting more interest as a non-invasive alternative to surgical resection thanks to its clinical characteristics: lower scarring, lower risk of infections, faster recovery, and lower hospitalization costs.

The possibility to selectively damage tumor without the need for skin incision, as well as no bleeding and no radiation make HIFU an attractive option for patients with breast carcinomas [90], [91]. Multiple clinical studies were successfully performed on HIFU treatment of breast cancer. Wu *et al.* showed complete necrosis of breast tumors of 2-4.8 cm in diameter by HIFU technique [93]. Authors demonstrated a 95% five-year disease-free survival, and the cosmetic results were estimated as excellent by most of the patients. Li *et al.* reviewed 11 arms of breast cancer treatment using HIFU therapy during the period 2002-2010. The complete necrosis rates achieved with MRI-guided HIFU were 59%, while US-guided HIFU showed 96% of complete necrosis.

Accurate thermometry during the ablation therapy is important not only to control heating process within the target lesion, but also to avoid undesirable thermal damage of the adjacent tissue. Development of reliable thermal mapping methodology will also serve research purposes: to investigate the biophysical processes during ultrasound ablation and to further refine HIFU therapeutic capabilities. Despite significant progress in HIFU devices, temperature monitoring techniques do not provide high-quality temperature measurements.

Imaging technologies are nowadays available both to guide clinical HIFU and as a temperature measurement methodology. Those are computed tomography (CT), ultrasound (US) imaging and magnetic resonance thermometry (MRT). Despite a good spatial resolution and non-invasiveness of MRI, there are serious limitations that doesnot allow the application of tomographic imaging during the clinical ultrasound ablation. As was discussed

in previous chapter, MRI is sensitive to any kind of motions, so respiratory movements will cause thermometry artefacts, moreover magnetic field drift of the MR magnet will also deteriorate the overall image quality [37].

In this section an FBG based sensory system is proposed to detect temperature of the ablated tissue during clinical HIFU thermal treatment performed *ex vivo* on a sample of breast fibroadenoma. The array of FBG sensors detect temperature fluctuations occurring *in situ*, and the measurement results confirm that temperature increment depends on the focusing and energy of each pulsed excitation during HIFU treatment. The FBG technology can also well translate into clinical practice, as the optical fibers are biocompatible, minimally invasive, lightweight and with a compact form factor, and are immune to electromagnetic fields.

In this Section, a setup is for HIFU ablation and temperature monitoring is presented, then the FBG interrogation and data processing is described, followed by the results of the measurements.

3.2.2 Experimental setup

Figure 3.1 shows photographic image of a medical HIFU device and a fiber optic sensor-based temperature measurement system. The corresponding schematic diagram is illustrated in **Figure 3.2**. An extracorporeal HIFU device is based on a flat transducer operating in the frequency range 800-2400 kHz and an acoustic lens to focus US (ultrasound) beam (Model-JC, Chongqing HAIFU, China). The lens has a diameter of 21.5 cm and a focal length F = 16.2 cm. As depicted in **Figure 3.2**, the transducer can be moved along *x,y,z*-axes, so that the focal point position changes at x = 120 mm, y = 120 mm and z = 180 mm around the natural focus. The treatment table is also equipped with a US monitoring device operating at 3.5 MHz that allows defining the boundary of tumor and provides visual feedback during the ablation treatment. The patient was familiarized with possible complications during treatment and signed patient consent for the procedure.

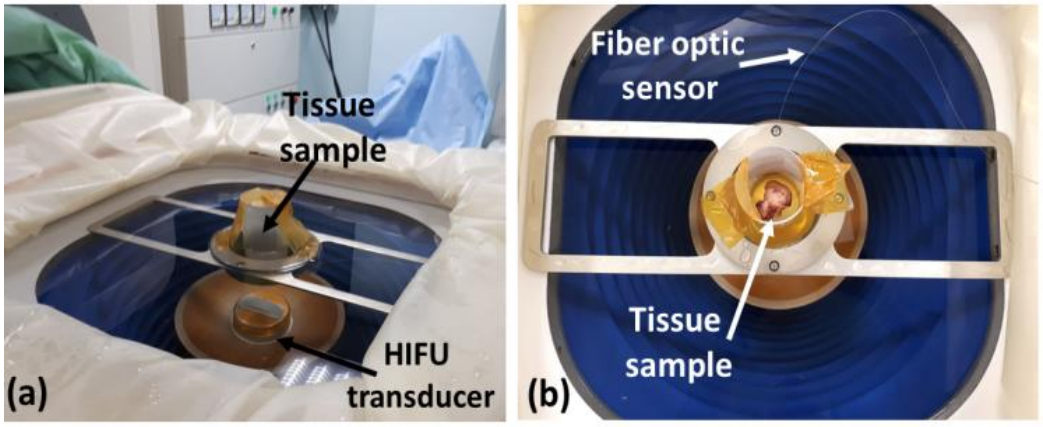

Figure 3.1 (a) Photo of the HIFU device and (b) photo of the HIFU water tank and the fiber optic sensor inserted into the tissue sample.

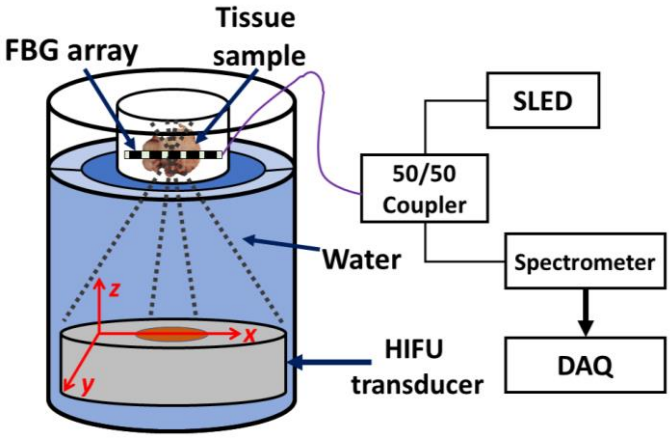

Figure 3.2 Schematic diagram of experimental setup for HIFU ablation and FBG temperature measurement system (not drawn to scale).

Experiments were performed *ex vivo* on a sample of excised tissue collected from a mammary gland by using biopsy instrument and 26-Gage needle (Bard Magnum) and degassed breast fibroadenoma taken from an adult female patient. Prior to a sample collection, fibroadenoma was localized with US guidance. Acoustic coupling is achieved using degassed deionized water. The tissue sample is placed inside a container and positioned on the membrane of the HIFU transducer's water tank, as shown in **Figure 3.1**b.

Temperature measurements were performed with a fiber optic based sensor system, consisting of array of draw tower gratings (DTG) and an interrogation setup. A DTG array has 5 gratings inscribed in ormoceramic fiber (FBGS International) with a length of 5 mm and 10 mm spacing between the center of

each grating. Prior to sonication, the fiber is inserted inside the breast fibroadenoma sample with a percutaneous 22-Gage biopsy needle (Chiba Biopsy Needle DCHN-22-10.0, Cook Medical); the needle is pulled back after the insertion.

In this study, a network of FBG sensors were interrogated with a setup, assembled in a small box. The interrogation system comprises a light source, and infrared spectrometer as a detector (I-MON-512-USB, Ibsen Photonics). Light source is a white light SLED with 60 nm bandwidth (Exalos EXS2100, ~20 mW emission power), controlled by a driver board (Exalos EBD5200, 250 mA current). The spectrometer works in the spectral range of 1520-1600 nm range and has 156 pm wavelength resolution. Light is directed to the fiber optic sensor through a 50/50 coupler (**Figure 3.2**).

Each FBG sensor in an array operates within a specific spectral range, with ~2 nm spacing between two adjacent Bragg wavelengths to exclude overlapping of FBG reflected spectra during sensing. Spectral data from all 15 FBGs were acquired by means of a LabVIEW™ code. Using the same code Bragg wavelength and wavelengths shifts were calculated for all FBGs. The analysed data were interpolated with spline interpolation [110] with an adequate accuracy (~1 pm), and allows fast operation (close to 100 Hz) [111].

3.2.3 Fiber Bragg grating sensors

The sensing element is constituted by an array of 5 FBGs. FBGs are periodic structures inscribed inside the core of a silica fiber using various techniques which are based on the photosensitivity of the silica, for example, inscription by means of a phase mask, or through a draw tower process [48], [100]. These structures are formed by a periodic modulation of the refractive index of the fiber core. An FBG acts as a notch filter, and reflects a narrowband spectral component, centered at the so called Bragg wavelength (λ_B) [100]. For an FBG with the periodicity Λ and effective refractive index of the fiber n_{eff}, the Bragg wavelength λ_B is defined by Bragg's law [112]:

$$\lambda_B = 2n_{eff}\Lambda\,, \tag{3.1}$$

The grating parameters Λ and n_{eff} change under variation of external conditions. For example, temperature sensitivity of a grating arises from two physical effects: the thermo-optic effect, i.e. the temperature dependence of the refractive index, and second is the thermal expansion of the glass. The reflected spectrum centered at Bragg wavelength is then shifted, and in absence of longitudinal deformation, the Bragg wavelength change arises from thermo-optic effect and to a lesser degree from thermal expansion of silica:

$$\frac{\Delta\lambda_B}{\Delta T} = 2\Lambda\frac{\partial n_{eff}}{\partial T} + 2n_{eff}\frac{\partial\Lambda}{\partial T}, \tag{3.2}$$

where $\partial n_{eff}/\partial T$ is the thermo-optic coefficient and $\partial\Lambda/\partial T$ is the thermal expansion coefficient of the fiber material, most commonly, silica. Substituting (3.1) into (3.2) and rearranging the equation, we get a relationship between temperature variation and the Bragg wavelength shift:

$$\Delta\lambda_B = \lambda_B\left(\frac{1}{\Lambda}\frac{\partial\Lambda}{\partial T} + \frac{1}{n_{eff}}\frac{\partial n_{eff}}{\partial T}\right)\Delta T = \lambda_B\left(\alpha+\xi\right)\Delta T, \tag{3.3}$$

where the thermal expansion coefficient and the thermo-optic coefficient are denoted as α and ξ respectively. Equation (3.3) can be rewritten as:

$$\Delta\lambda = k_T\Delta T, \tag{3.4}$$

where k_T is the temperature sensitivity of the grating. Therefore, temperature variations ΔT can be detected in an accurate way by measuring the Bragg wavelength shift, using one of the demodulation techniques [110].

Figure 3.3 schematically illustrates the sensing principle of an array of 5 FBGs. As seen from **Figure 3.3**b, each FBG reflects at specific wavelength, Bragg wavelength λ_B, separated by about 2 nm. The spectrum shifts when temperature changes (**Figure 3.3c**). The Bragg wavelength shift $\Delta\lambda_B$ is detected by interrogation system and corresponds to the temperature change ΔT, recorded at each of 5 sensor locations.

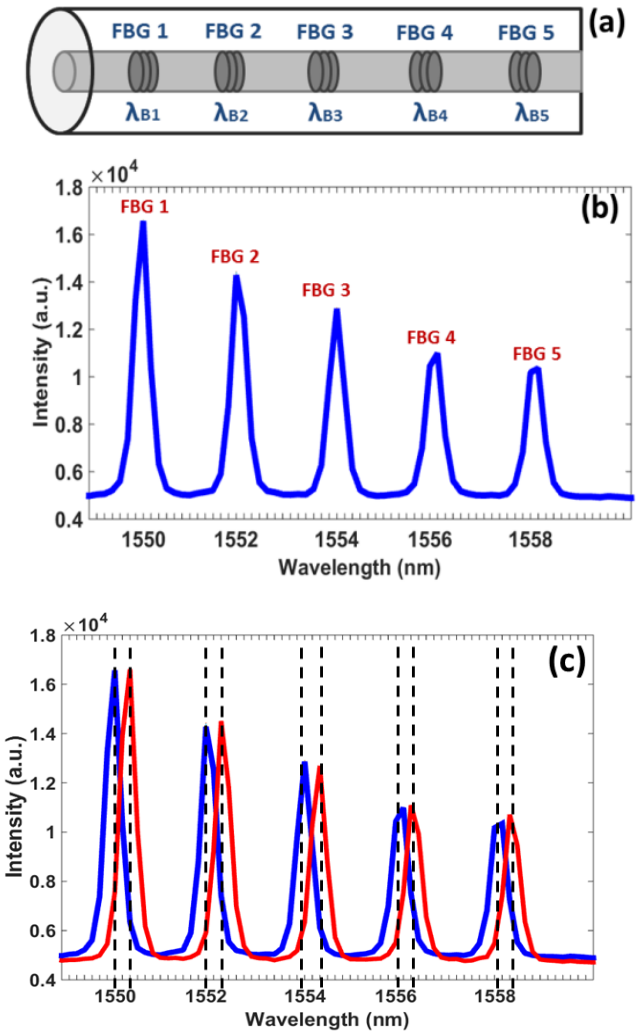

Figure 3.3 Sensing mechanism of FBGs: (a) schematic of 5 gratings inscribed in a fiber, (b) reflected spectra comprising wavelengths reflected by all FBGs, (c) the shift of each Bragg wavelength $\Delta\lambda_B$ corresponds to the temperature change ΔT, recorded at the locations of the FBG.

3.2.4 FBG sensor calibration

Thermal sensitivity coefficient of each FBG was determined through a calibration of an optical fiber in a temperature controlled water bath. An electronic contact thermometer (IKA ETS-D5) was used for reference measurements to record water temperature (T) ranging from 25 °C to 75 °C. As the water was heated with a step 5 °C, the Bragg wavelength λ_B of the FBG 1, FBG 2…FBG 5 was recorded with an interrogator described in previous section. **Figure 3.4** reports the wavelength shift $\Delta\lambda_B$ of each grating as a function of the temperature T, according to Equation 3.4. Since it is a

linear function, temperature sensitivity coefficient was estimated as the slope of the plot. The average temperature sensitivity coefficient for all FBGs in the array was estimated as k_T = 13.07 pm/°C. This value is close to manufacturer's specification. This thermal coefficient has been used in the interrogator to convert the spectral shift of each FBG into the estimated wavelength.

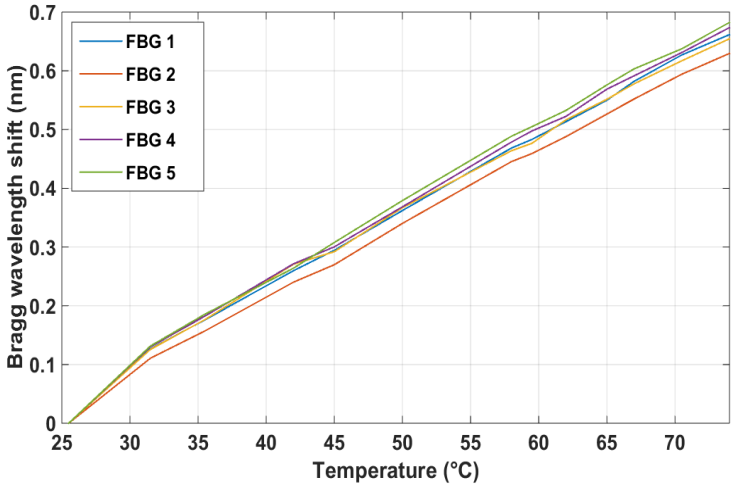

Figure 3.4 Calibration functions for the FBG sensors; the chart reports the wavelength shift as a function of the applied temperature during a temperature cycle in a water bath.

3.2.5 Measurement results

After the fiber optic sensor was inserted in the tissue sample, the sample with a fiber were fixed inside the sample holder and positioned on top of the plexiglass tank, as illustrated in **Figure 3.1**b. HIFU ablation was performed by three sets of pulses with different power: 100 W, 200 W and 400 W. The duration of each pulse is 1 s, so the total duration of the procedure is 30 s. We analyse temperature changes by reconstructing spectral data obtained from all 5 FBGs. **Figure 3.5** presents temperature records from the start to the end of HIFU treatment. Temperature of the tissue starts increasing in accordance with the acoustic pulses generated by the HIFU transducer: each peak recorded by the FBG sensor is associated with the pulse, and duration of each pulse is 1 s. The first set of pulses with power equal to 100 W heats the target volume of the tissue; the increase of power to 200 W leads to the temperature increase to 4 °C from the initial temperature. The last set of pulses performed

at 400 W power lasts from 22 to 30 seconds and leads to a steep rise in temperature up to 12 °C, as shown in **Figure 3.5.**

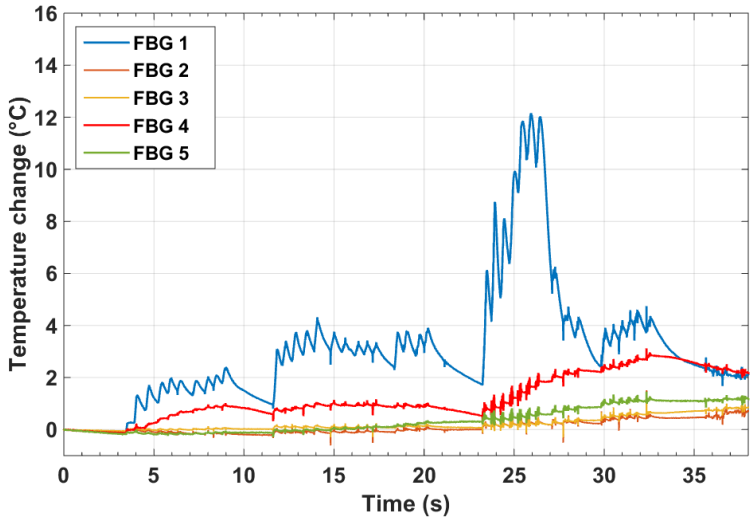

Figure 3.5 Temperature recorded by FBG sensors during HIFU ablation. The legend shows each FBG label according to its position inside the array.

3.2.6 Conclusion

In conclusion, for the first time, we report an FBG-based sensory system for the thermal profiling of HIFU treatment was presented. HIFU ablation was performed of breast fibroadenoma sample. A network of 5 FBG sensors is deployed to record temperature distribution within the ablation region. The time-domain temperature chart demonstrates the possibility of employing FBG sensors to monitor temperature during clinical HIFU procedures; the proposed sensor system is able to detect temperature rise as a response to increasing acoustic power.

3.3 Comparison of fiber optic sensors for thermal ablation monitoring

3.3.1 Introduction

Fiber optic sensors (FOS) are gaining great attention in the fields of medicine and biology due to their exceptional properties [113]: small size and lightweight, that guarantee a minimally invasive form factor; biocompatibility, in accordance to ISO 10993 standard; immunity to electromagnetic interference,

that makes FOS magnetic resonance (MR)-compatible; high sensitivity to both capability to respond at high speed to both physical and biological parameters, and the possibility to achieve sub-millimeter spatial resolution [101]. Modern applications of the biomedical FOS include measurements of blood vessel obstructions [114], intra-cranial pressure, intra-aortic balloon pumping therapy, solid state manometers, biomechanics, where commercial systems have been developed [115], [116].

The current generation of FOS embodies another significant advantage over traditional sensing technologies based on electronic sensors: rather than limiting the measurement to a single or few sensing point(s), FOS can employ multiplexed or distributed sensors to spatially resolve physical parameters such as temperature or strain [106]. In biomedical applications, Tosi *et al.* [99] identified 3 sensing technologies that can resolve temperature on a single fiber with a resolution inferior to the centimeter:

(1) Fiber Bragg Grating (FBG) arrays, which behave as a cascade of narrow-band notch filters, and were discussed in previous section of this Chapter;

(2) Chirped FBG (CFBG) that has index modulation of the core with non-constant period and behaves as a continuous array or cascade of FBGs.

(3) Optical frequency-domain reflectometry (OFDR) that interrogates distributed weak reflections occurring in the sensing fiber.

One of the most advanced implementation of OFDR is the optical backscatter reflectometry (OBR), in which the measured distributed reflections are the Rayleigh backscattering components observed in a standard fiber [107].

These sensing technologies differ in terms of cost, spatial resolution, but all report data in form of “thermal maps”, that display temperature as a function of space and time. Temperature sampling occurs both in time, which corresponds to the measurement speed, but also in space, identifying the spatial resolution that is defined as the distance between two adjacent sensing points. FBG arrays can detect with 1 cm spatial resolution, while the other techniques can approach the millimeter scale.

The most immediate medical application of temperature sensing at the millimeter scale is in the real-time monitoring of thermal ablation procedures.

As was discussed in Chapter 2, FOS have substantial advantages with respect to conventional temperature monitoring techniques, such as

thermocouples and imaging, and their use of FOS in thermotherapies has been consolidated since 2014. The key asset is the possibility to use a single optical fiber to resolve a temperature distribution. For this application, the spatial resolution, accuracy, time response, and cost of the disposable element are key performance indicators of the effectiveness of the sensing methods. All the previous methods have been used for temperature sensing in thermo-therapies: FBG array is the most consolidated method, reported by Webb *et al.* in 2000 and subsequently extended more recently for RFA, MWA, and LA. OBR has been reported by Macchi *et al.* for RFA [108]. Chirped FBGs have been first reported by Tosi *et al.* in 2014, and subsequently enhanced in 2018 using a spectral reconstruction method [55], [109].

While several works have been reported, no conclusions have been drawn regarding the effectiveness of these methods.

In this section, a comparative scenario is proposed, whereas the 3 different fiber optic sensors are used to detect the temperature pattern in RFA, and positioned in the same location with multiple interrogators. With this setup, we can evaluate the thermal maps of each individual sensing system and compare their performance, evaluating the most suitable methodologies for temperature detection in thermal ablation.

3.3.2 Experimental setup

We propose experimental setup designed to simultaneously investigate three fiber optics-based sensing methods for monitoring temperature pattern during RFA. **Figure 3.6** and **Figure 3.7** show, respectively, a photographic image and a schematic of the experimental setup, which is comprised of RF ablation tool and two independent temperature measurement systems. The tool for RF ablation is a custom-made RF generator operating at 450 kHz (Leanfa Hybrid Generator). The energy is delivered to the tissue with a solid brass percutaneous applicator of 160 mm length and 3 mm diameter, and terminated with a conical active electrode (AE) with 5 mm length; for the passive electrode (PE) a metallic plate is used positioned underneath the tissue. Ablation experiments (with RF power set at 30 W) were performed *ex vivo* on a porcine liver obtained from a local slaughter house. The phantom has been refrigerated until the measurement time, and then rested until

reaching room temperature (~ 21 °C). A contact thermometer (IKA ETS-D5) was used to register the temperature of phantom before the start of ablation.

The custom-made interrogation system for FBG and CFBG sensors is made up of a superluminescent LED source (SLED, Exalos EXS2100) having 60 nm bandwidth and with emission power of ~20 mW, and a infrared spectrometer (I-MON-512 USB, from Ibsen Photonics). Spectrometer works within the 1520-1600 nm range, with 512 sampling points on the wavelength grid. A network of two 50/50 couplers is used to direct light to CFBG and FBG array and to collect the backreflected spectra. As shown in **Figure 3.6**, all the components of the FBG and CFBG interrogation system are placed in a small case. Analysis of FBG and CFBG reflection spectra and the subsequent temperature reconstruction have been performed with spline interpolation realized through a LabVIEW code [3].

Figure 3.8 shows the liver phantom prior to the start of ablation: RF probe is placed on top of the tissue with three fiber optic sensors positioned next to it. The sensors were placed in closest proximity to each other and to RFA applicator to provide simultaneous temperature sensing during the procedure: FBG array was positioned in such a way, that the central grating was aligned with the RF applicator tip (**Figure 3.8b**).

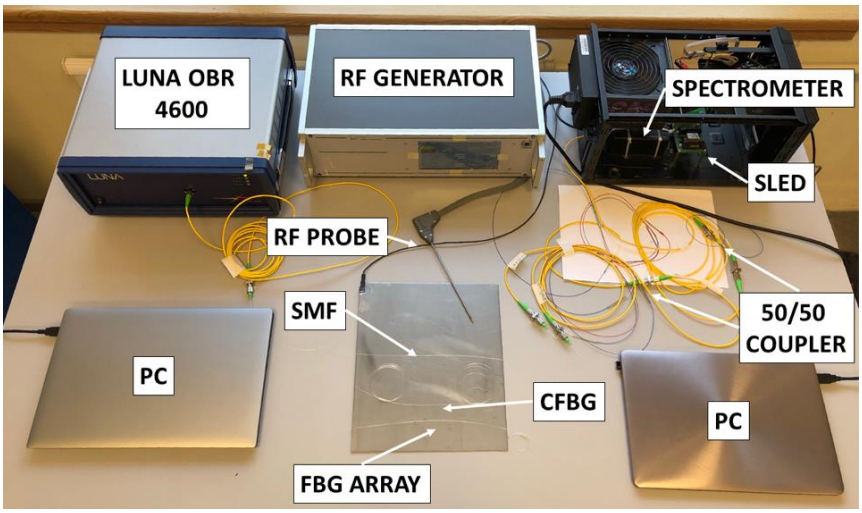

Figure 3.6 Photo of RF hyperthermia and fiber optic sensors interrogation setup, arranged on the bench. On the left side, the OBR (Luna OBR4600) with its control PC. In the center, the RF generator with the active electrode probe, and the metallic plate acting as passive electrode. On the right, a custom-made interrogator made by SLED and spectrometer with its control PC, for dual detection of FBGs and CFBG.

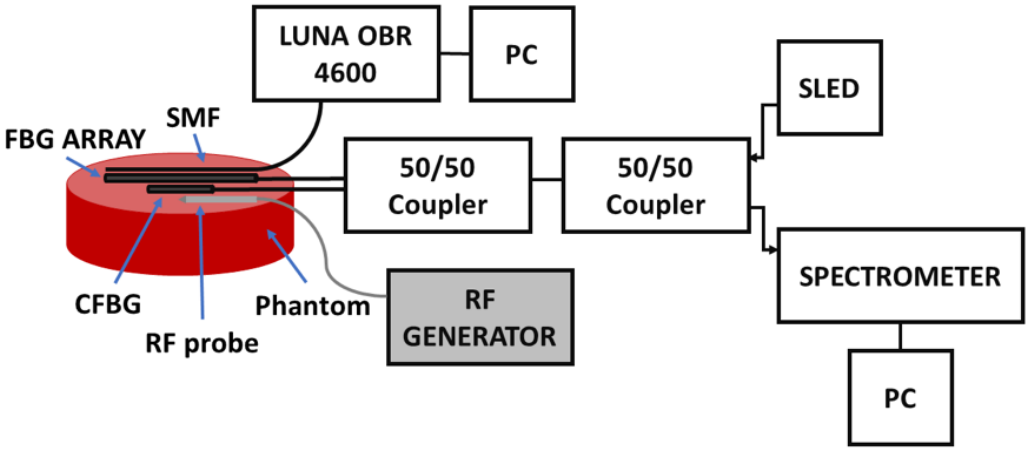

Figure 3.7 Schematic of the experimental setup based on RFA hyperthermia and fiber optics sensing systems.

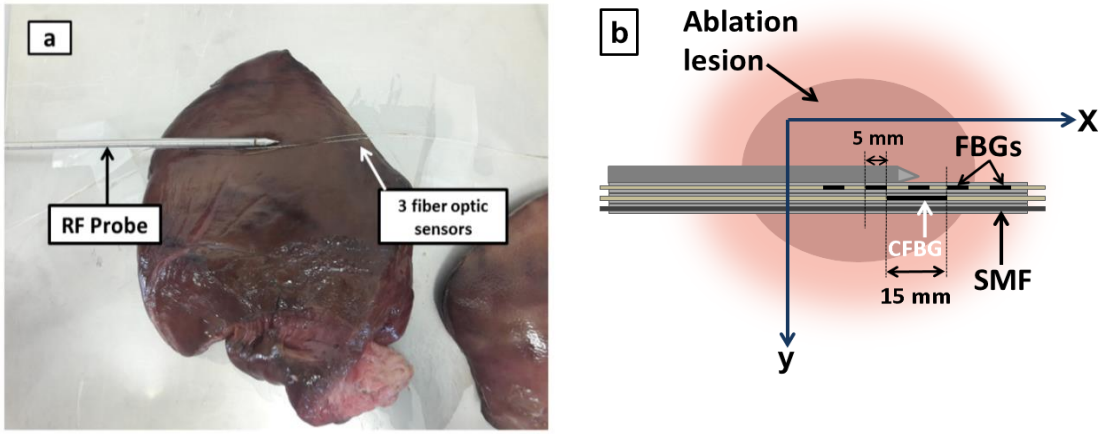

Figure 3.8 (a) Photographic image and (b) schematics of positioning of RF probe and three fiber optic sensors in the phantom tissue prior to RFA heating.

Temperature measurements were performed with an array of 5 draw tower gratings (DTG, FBGS International), inscribed in ormoceramic fiber, and a Chirped FBG (Technica S. A). Each DTG has a length of 5 mm and 10 mm spacing between each grating, whereas the length of chirped Bragg grating is

15 mm and reflectivity >90%. The reflectivity of FBGs is 5-10%, as typically observed in short-length gratings inscribed via drawing tower process. All 5 DTGs have different Bragg wavelengths, with ~2 nm spacing between two adjacent wavelengths; such a spectral spacing is sufficient to avoid overlapping of FBG spectra during sensing. We show in **Figure 3.9** the spectrum of the CFBG and FBG arrays. The wavelength range of the CFBG was chosen in the way, that the spectrum did not overlap with the FBG.

In parallel to FBG and CFBG measurements temperature variations were recorded through Rayleigh backscattering reflections observed in a standard single mode optical fiber (SMF). Interrogation unit is LUNA OBR 4600 (Luna Technologies). The instrument allows detecting, with a spatial resolution selected by a user, the amount of light backreflected in each section of the fiber by Rayleigh scattering effect. In the following section we will discuss interrogation principles for all three sensing methodologies. The fibers were positioned parallel to each other and in the closest proximity to RF applicator, so that the applicator tip was aligned with the center of CFBG and the middle point of the central grating of the FBG array.

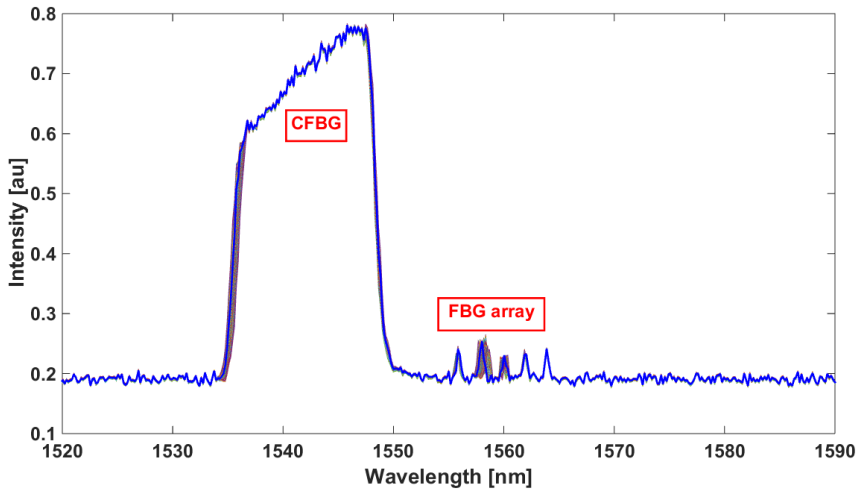

Figure 3.9 Reflected spectra of the CFBG and of the 5-element FBG array, detected on the spectrometer.

3.3.3 Interrogation

FBG and CFBG

The sensing mechanism and interrogation of the FBG array was presented in the previous section of this Chapter.

The CFBG is proposed as a semi-distributed sensor for estimation of temperature profiles over ablation area. We consider the case of a linearly chirped FBG, whereas the Bragg wavelength varies from the start to the end of the grating according to a constant spatial rate, defined as the chirp rate coefficient [3]. Due to the linear variation of the Bragg wavelength, the CFBG behaves as a continuous of Bragg wavelength, thus having a wideband reflection spectrum of tens of nanometers (**Figure 3.9**). When a spatially uniform temperature field acts on the CFBG, the whole spectrum shifts and the CFBG behaves as a wideband FBG. However, when the temperature pattern is not uniform in space, the whole spectral envelope of the CFBG is modified, and we can demodulate by reversing this process, i.e. estimating the temperature pattern from the spectral changes. As for a uniform FBG, the temperature coefficient is 10.2 pm/°C.

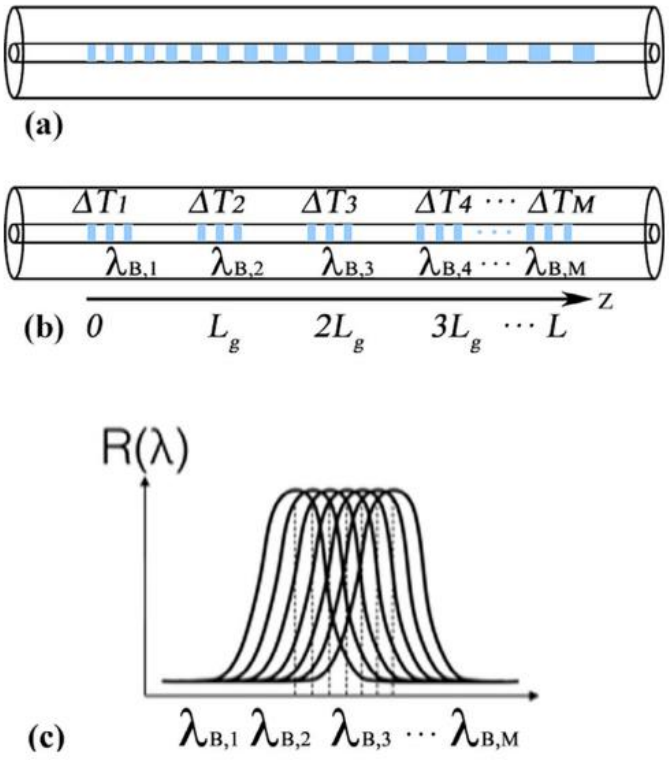

Figure 3.10 Principle of CFBG modelling. (a) CFBG: grating period is increasing with distance. (b) CFBG model using *N* number of uniform FBGs, located at distance $(i-1)\cdot L_g$ and exposed to temperature ΔT_i and related Bragg wavelengths $\lambda_{B,i}$, to form a cascade of filters. (c) Spectrum consisting from *N* number of uniform FBG spectra.

In this study, a method for demodulation of the CFBG spectrum is based on the algorithm developed by S.Korganbayev et al. [3]. The working principle of this model is presented in **Figure 3.10**, here the chirp grating with length *L* is discretized into N uniform gratings, each having length $L_g = L/M$. Each of the N discretized gratings is treated as a uniform standard grating, with its Bragg wavelength determined by the chirp coefficient, and simulated using the CMT.

Discretization factor *N* will define spatial resolution of the obtained temperature data. So, for the CFBG length 1.5 cm, the spatial resolution will be 0.15 mm. The number of N is chosen based on the bandwidth, the length of the grating, in such a way that the simulated spectrum will be more close to the real CBGF spectrum, as shown in **Figure 3.10**(c). Increasing *N* will significantly increase computational time.

The demodulation technique is based on two chirped gratings: (1) the real grating, the spectrum of which is detected with interrogator described earlier; (2) the artificial grating, generated using Erdogan's coupled-mode theory (CMT), which is designed to match the first grating spectrum. When the measured grating changes, we apply a temperature variation to the artificial grating, until the difference between the artificial and real grating is minimized. In turns, CFBG demodulation is converted into an optimization problem. Here, the assumption is that the temperature pattern has a shape known a priori, which approximates previous modelling [117] and experimental [108] results of RFA.

The simulated spectrum of CFBG is generated as in [3] with CMT model, which is obtained by discretizing the grating into a set of N = 100 discrete gratings (along the direction of propagation *z*), each uniform and contributing to the overall spectrum. We assume that the temperature distribution has a Super-Gaussian shape [108]: this pattern well approximates the rapid growth of temperature in proximity of the RFA applicator, until reaching a temperature plateau when the inner tissue vaporizes [118]. Such a temperature profile $\Delta T(z)$ is described by:

$$\Delta T(z) = A \cdot e^{-\left(\frac{|z-z_0|}{2\sigma_0}\right)^{2G}} \tag{3.5}$$

$$\sigma_0 = \frac{\sigma}{\left(\frac{\pi}{2}\right)^{\frac{1}{2G-1}}} \tag{3.6}$$

where A is the amplitude, σ is the standard deviation, z_0 is the central point (at which the temperature is maximum), and G is the Super-Gaussian order.

To decrease the complexity and increase the rate of demodulation, the algorithm was divided into two main parts. The first part of demodulation process is considered on the estimations of starting and ending wavelength values of reflection spectrum, evaluation of transfer function for aligning the top of reflection spectrum for compliance with the characteristics of real fiber reflection, and the simulation of reflection spectrum using combination of the gradient parameters – amplitude, center, variance, and super-Gaussian power. Initially, the spectra are simulated by using a combination of the parameters in equations 3.5-3.6. Then, obtained reflection models are saved with the corresponding gradient parameters in the form of matrix in separate database. In order to distinguish each matrix, they are named according to the amplitude variations. **Figure 3.11** briefly demonstrates first part algorithm.

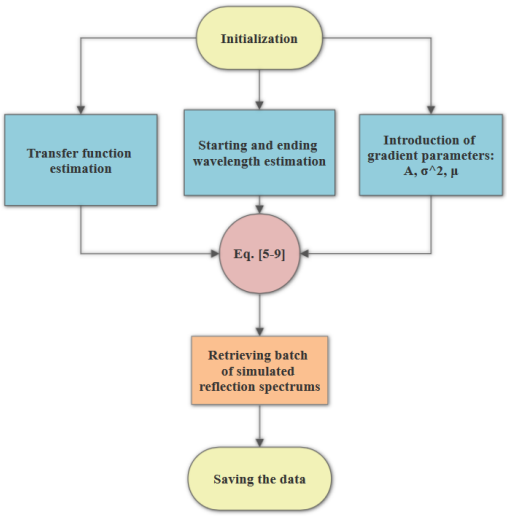

Figure 3.11 CFBG demodulation technique: first part algorithm - preliminary simulations of reflection spectra.

The second part of the demodulation is introduced during the ablation process. The algorithm works in a loop mode with feedback element –

temperature change value, which is also the amplitude value of thermal gradient. Initially, the algorithm obtains the change of the temperature and for the first cycle it is assumed to be 0. According to the temperature change, it extracts corresponding matrix from database with simulated reflection models made in the previous part. Then, all simulated models are compared with the measured model by using Mean Squared Error (MSE). The most related model ascertains the required gradient parameters for reconstruction of temperature distribution, and the amplitude value is then passed as the input for the next temperature measurement of thermal ablation process. The steps of the second part are illustrated in **Figure 3.12**

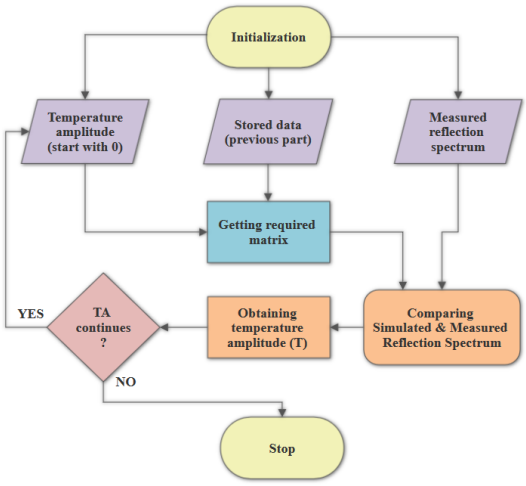

Figure 3.12 CFBG demodulation technique: second part algorithm – identification of gradient components during thermal ablation.

OBR

The OBR method is a coherent optical frequency-domain interferometers (OFDR), in which the photodetectors track the Rayleigh scattering profile of the sensing fiber over its length and over a range of wavelengths. In presence of Rayleigh scattering, the refractive index of the fiber is subjected to local variations, which appear as a random spectral signal; the randomness is due to the fact that the defects in the fiber is not a deterministic but rather a statistic factor, and therefore the scattering signal appears as a random process, but consistent over time and space. This scattering content, labelled the “signature” of the fiber, shifts in wavelength with a sensitivity identical to a FBG.

The OBR used in experiments perform the OFDR method as in [107], and converts the signature into each temperature variation according to Froggatt's method [119].

This method has been implemented into the commercial OBR system used in experiments (Luna OBR4600), which operates with the parameters listed in **Table 3.1.**

Table 3.1 Parameters of the OBR system.

Parameter	**Setting**
Temperature coefficient	10.2 pm/°C
Sensing range	1.2 m
Gage length	1 cm
Sensor spacing	2 cm
Spatial resolution	0.1 mm
Scanning rate	3 Hz
Wavelength range	43.01 nm
Scan range	1545.5 – 1588.51 nm
Sensing fiber	SMF-28

3.3.4 Results and discussion

Experimental setup shown in **Figures 3.6 and 3.7** has been used to perform RF ablations and the temperature distribution measurements. Thermal ablation tests were carried out at room temperature on a porcine liver phantom, purchased in a local market. The phantom has been refrigerated until the measurement time, and then rested until reaching room temperature. The phantom was placed on the grounding pad, which acts as a passive electrode. In order to facilitate the insertion of the fibers, and ensure that all sensors are recording the temperature at the same location, the phantom has been divided in two parts: all fibers have been positioned in the bottom part, after inserting the RFA applicator, and subsequently an upper layer of phantom has been placed on the top, sealing the fibers and the applicator electrode into the tissue. With this method, it was possible to control the fiber positioning with respect to the applicator, without introducing a positioning error due to a needle puncture insertion, while ensuring that the RFA tip is in full contact with the phantom tissue in the ablation region. The RF power has been set to 30 W, and the ablation was performed for a duration of 215

seconds minutes, with additional 35 seconds after the RF power had been disconnected (cooling stage).

Data were recorded from the start of RF ablation, and lasted 250 seconds. Spectral data were collected simultaneously in real time for all 3 types of sensors: for FBG array and CFBG reflected spectra were detected with Ibsen infrared spectrometer (**Figure 3.6**), and Luna OBR was used to perform measurements on the SMF fiber. The temperature data have been recorded in real time and were processed using the interrogation techniques described above.

Figure 3.13 reports temperature as recorded by 5 elements of an array. The positioning of FBG array during RF ablation was in the closest proximity to RF applicator, so that the 3rd FBG (central) was aligned with the applicator tip x = 0. The maximum temperature was recorded, as was predicted, in the ablation area closest to the RFA tip; then temperature is increasing with the distance from the applicator tip. The tissue was heated linearly from the start of ablation t = 0 s. until it reaches maximum temperature after 200 s.

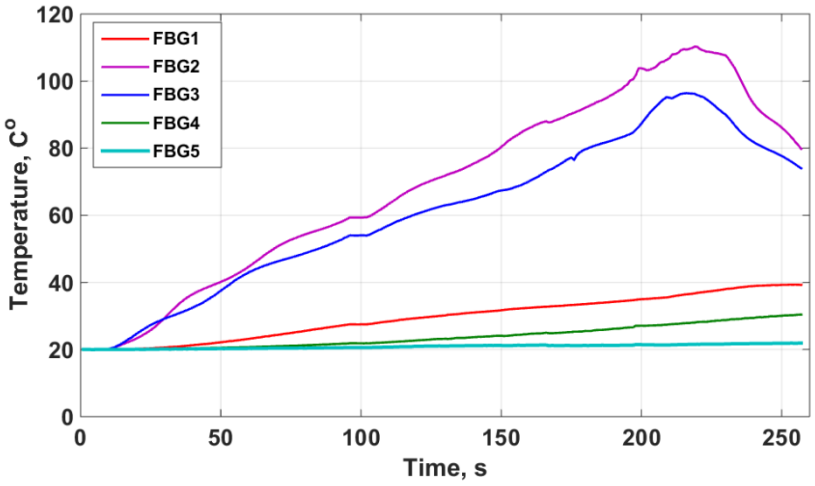

Figure 3.13 Temperature data recorded by 5 FBGs

FBG 2 records 60 °C threshold after t = 96 s., and the central FBG recorded 60 °C at t = 118 s. The tissue reaches maximum temperature of 96.4 °C after 216 s for FBG 3, and T_{max} = 110.3 °C recorded by FBG 2 after 219 seconds.

Peak temperatures recorded by 3 fiber optic sensing technologies during RF ablation is reported in **Figure 3.14**. The plots show similar peak temperature values recorded by an FBG array (110.3 °C) and with OBR distributed sensor T_{max} = 109.84 °C. FBG array exhibits a time delay in measuring data,

compared to OBR: for almost the same values of temperature, the time is different, for an array it's t_{max} = 219 s., which is later than for OBR t = 203 seconds.

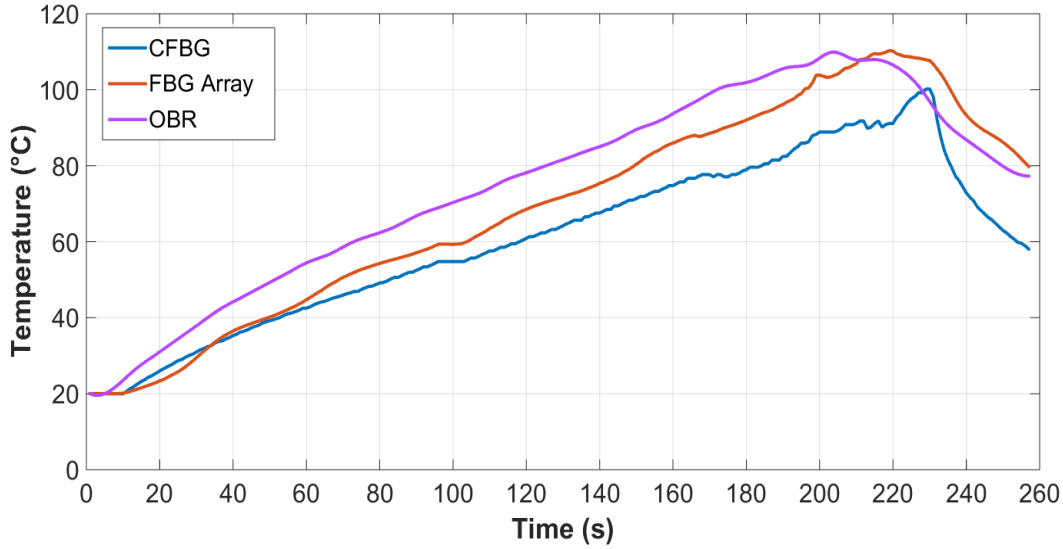

Figure 3.14 Peak temperatures recorded in real time by FBG array, CFBG and distributed sensing methodologies during RFA.

From the **Figure 3.14** we observe that CFBG tends to underestimate the temperature values, for example, 60 threshold is recorded after 116 s, and the peak temperature value is 100.2 C, which is lower compared to FBG array and distributed sensor. From **Figure 3.14** as well as **Table 3.2** we observe that both FBg array and CFBG underestimates temperature values, which can be associated with lower spatial resolution (1 cm for FBGs compared to sub-centimeter resolution achieved with OBR technology).

Table 3.2 Comparative study of temperature recorded by 3 fiber optic sensing techniques during RFA

	60 °C threshold, s	**T_{max}, °C**	**t_{max}, s**
FBG array	97	110.3 °C	219
CFBG	116	100.2 °C	230
Luna OBR	73	109.84 °C	203

Temperature data are presented in the format of thermal maps (**Figures 3.15-3.17**), i.e. the temperature is displayed a function of space and time.

Figure 3.15 presents thermal map obtained for the temperature profiling of RFA with SMF fiber and interrogated with Luna OBR. Data are reported in the form of isotherms, with 10 °C step. X axis displays duration of experiment in seconds, and Y axis shows distance along the sensor, where Y = 0 corresponds to the RFA tip. Contour charts clearly demonstrate Gaussian shape of the temperature distribution, which are the common thermal patterns for the RFA. The maximum temperature is observed near the RFA tip at Y = 0, and then temperature decreases with the distance from RFA tip.

From the thermal map confirms **Figure 3.14**, that the damage threshold is reached at t = 73 s, in the closest proximity to RFA tip, then heat is distributed through the thermal conduction to the outer regions of ablation lesion. The maximum temperature detected with distributed sensor is 109.98 °C, and it is measured at t = 206 s. From the contour charts we estimate the volume of ablated lesion to be 1.73 cm.

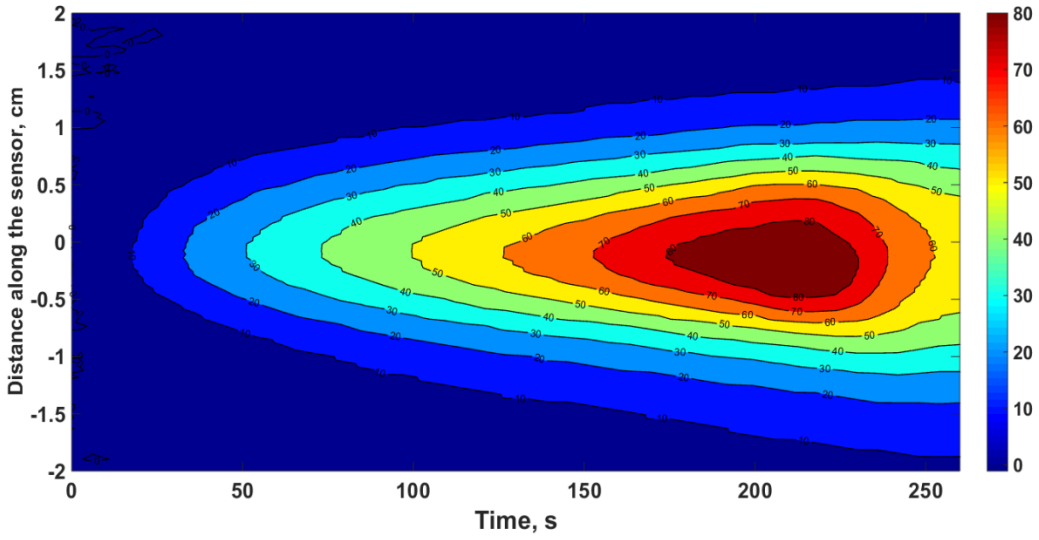

Figure 3.15 Thermal map obtained with OBR distributed sensor during RFA. *X* axis shows duration of ablation. *Y* axis shows the sensor length with *Y* = 0 coordinate corresponding to the RFA tip.

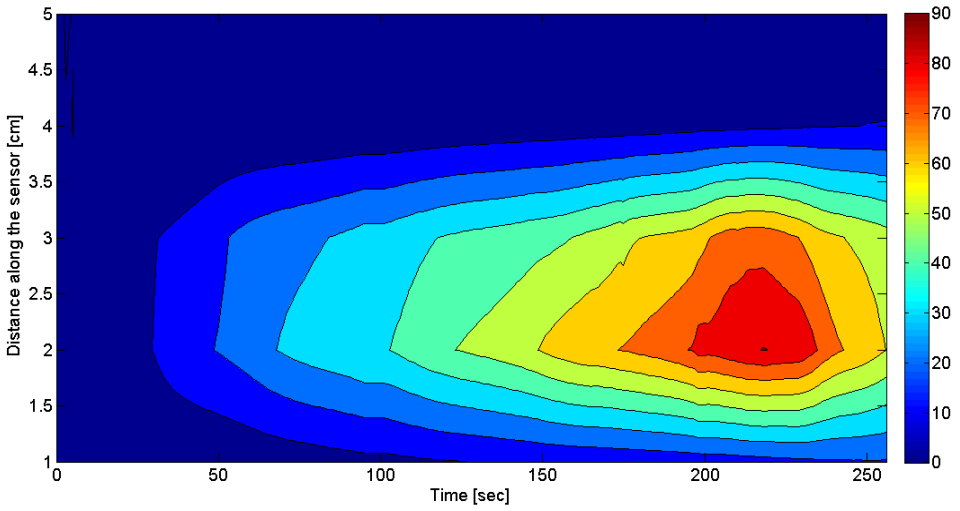

Figure 3.16 Thermal map obtained with 5 FBGs during RFA. *X* axis shows duration of ablation. *Y* axis shows the sensor length in cm, corresponding to the length of each FBG 5 mm, and 5 mm spacing between the gratings.

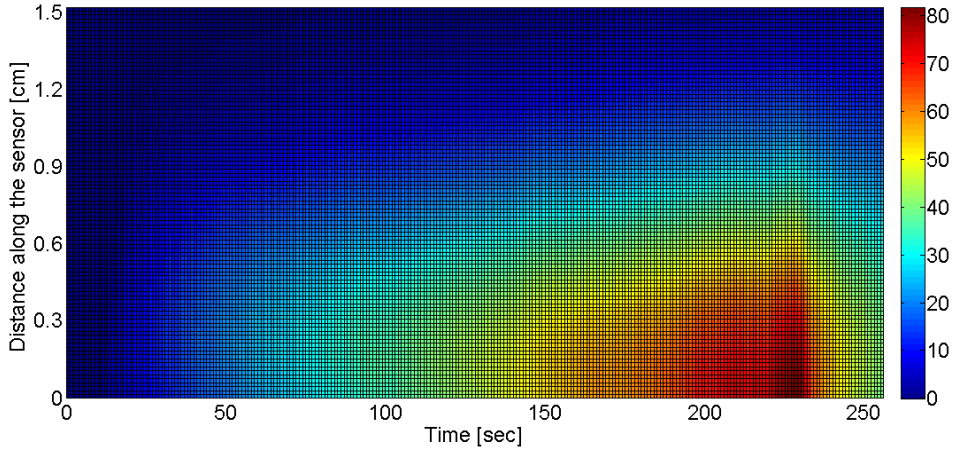

Figure 3.17 Thermal map obtained with CFBG during RFA. *X* axis shows duration of ablation. *Y* axis shows the sensor length in cm.

Figure 3.16 presents thermal map obtained for the temperature profiling of RFA with an array of 5 FBGs. Data are reported in the form of isotherms, with 10 °C step. X axis displays duration of experiment in seconds, and Y axis shows distance along the sensor.

From the thermal map shows, that the damage threshold is reached at t = 103 s, in the closest proximity to RFA tip, then heat is distributed through the thermal conduction to the outer regions of ablation lesion. From the contour charts we estimate the volume of ablated lesion to be 2.17 cm. A thermal map obtained for the CFBG measurements is presented in **Figure 3.17**

3.3.5 Conclusion

This work summarizes a comparative study of sensing performance of 3 fiber optic sensing technologies, for the application of RF ablation. Application of each type of sensor is the trade-off between spatial resolution, cost, and interrogation complexity. Using a standard SMF fiber interrogated with OBR provides the highest resolution; up to 0.2 mm of spatial resolution can be achieved with this type of sensor. Such characteristics meet the optimal requirements for the accurate monitoring of thermal ablation procedures, which are 1-2 °C temperature accuracy, 1 reading per second measurement speed, and 1 mm or below of spatial resolution. Despite excellent performance, OFDR is limited by a high cost of interrogation unit, as well as the trade-off between accuracy, spatial resolution, scanning rate, and sensing length. FBG sensors are low cost, however provides much poor spatial resolution compared to distributed sensor, since the size of FBG grating is 5 mm and the spacing is 5 mm, it is not possible to achieve the resolution better than 1 cm. CFBG has a sophisticated demodulation procedure, leading to an error in measurements and the overall underestimation of temperature.

CHAPTER 4

Fiber Bragg grating-based temperature profiling during nanoparticle-mediated thermal ablation

Chapter 4 reports the analysis of thermal distribution in *ex vivo* magnetite (Fe_3O_4) nanoparticle-mediated thermal ablation. In order to facilitate heat propagation, and maximize the volume of complete cell death, a functional solution with nanoparticles was injected into the target tissues.

The effects of nanoparticles on heat distribution during RFA and MWA was studied with fiber Bragg grating sensory system. A network of 15 FBGs were built and applied to obtain real-time temperature profiles. Experiments were conducted *ex vivo* on a liver phantom before and after injection of magnetite nanoparticle solution of 2 mg/mL and 5 mg/mL concentrations. Results are presented in the forms of thermal maps, and analyzed in terms of the 60 °C lethal isotherm. Results demonstrate the increase in ablated zone due to presence of NPs for both RFA and MWA.

The work presented in this Chapter was published in [57], [58].

4.1 Introduction

4.1.1 Limitations of thermal ablation procedure

As was described briefly in the previous chapters of the thesis, electromagnetic energy-based therapies, such as RFA, despite their minimally invasive characteristics, suffer from serious limitations. The shortcomings include the lack of *in situ* monitoring of the procedure, from one side, and the restrictions of the ablative lesion after a single treatment. The latter comes from several factors:

1. During percutaneous thermal ablation, like RFA and MWA, the highest temperature is achieved in the area closer to applicator tip, and decreases with the distance. Generally, the average dimension of the

ablation zone created by percutaneous RF device, does not exceed 35-40 mm. Thus, coagulative necrosis doesn't extend to the outer regions of the large tumor (>50 mm in diameter) [120], [121], significantly limiting the number of patients for RF therapy.

2. Complete thermal destruction of tumor is achieved only in 60% - 90% cases, and typically when treated lesions don't exceed 40 – 50 mm in diameter. For example, hepatocellular carcinoma and hepatic metastatic lesions observe more recurrence cases for large tumors measuring >5 cm. It is a result of incomplete thermal destruction [1], [122] after RFA.
3. In case of large size tumors incomplete coagulative necrosis can be reduced through multiple ablative procedures across the target area, however such an approach does not guarantee an overlap of all lesions. Thus, the risk of incomplete tumor destruction, and hence, the risk of local recurrence, is still a challenge.
4. A steep rise of the tissue impedance during RFA procedure is another limiting factor, which leads to the interruption of the process. As the temperature of the tissue approaches ~100 °C, the water starts to vaporize. Clinical RFA devices have an impedance meter and operate in safe mode, to discontinue RF power when the tissue impedance overcomes a 300-1000 Ω threshold. However, this effect limits the capacity of RFA to reach the outer borders of tumors, hence limiting the size of ablated tissue.

In the following section we will discuss solutions to overcome these limitations. Those are related to application of nanomaterials, in particular, nanoparticles to improve the outcomes of the thermal ablation.

4.1.2 Role of nanoparticles in thermal ablation therapies

Applications of nanomaterials in biology and medicine are being widely investigated. Numerous groups have studied the effects of nanomaterials, and in particular, nanoparticles (NPs), to improve the result of thermal ablation procedure. Recently, it was demonstrated that the outcomes of RF-based ablation can be improved through maximizing thermal damage in the treated area, without affecting the tissue surrounding the tumor.

In order to overcome the issues of incomplete thermal destruction of tumor, certain types of nanomaterials are targeted into a tumor site either actively or passively. In particular, during RFA electrically-conductive nanoparticles absorb electromagnetic energy and convert it into heat to induce thermal damage. Such an effect is explained by Joule heating produced by conductive nanoparticles through the RF-induced generation of local electrical currents over the nanoparticles volume [123]. Studies showed that gold NPs and carbon nanotubes provide a strong absorption of RF radiation even with small concentrations of NPs of the order of 1 mg/mL [123], [124].

Tamarov *et al.* reported the use of Si nanoparticles (NP) to increase temperature during RFA [125], while Mooney *et al.* proposed Au nanorods of different concentrations to mediate the photothermal ablation in mice [126]. Temperature rates increased with the increasing of gold nanorods concentrations. An alternative approach has been carried out by Ashokan *et al*. reported RFA mitigated by a biomineral agent [127]. Overall, the use of NP introduced *in situ* within the tissue alters the electrical impedance and the heat conductivity of the tissue, depending on their density and position [125], [128]. Previous studies show that NP-mediated ablation has a better capacity of delivering heat to the peripheral sides of the tumors.

In this Chapter, we demonstrate fiber optic based sensor system for *in-situ* thermal profiling of nanoparticles-enhanced thermal ablation. The effect of magnetite nanoparticles (MNPs) on the RFA and MWA is analysed with a 15 FBGs-based network.

Section 4.2 reports temperature profiling during MNPs mediated RF ablation by means of FBG based sensor setup. Section 4.3 covers thermal profiling with FBG sensors during NPs mediated microwave ablation. The conclusions (Sect. 4.4) show that the FBG-based measurements highlight that injections of MNPs with concentration of 2 mg/mL and 5 mg/mL is effective in spreading the heat to the peripheral areas of the tissue, resulting in a significant extension of the ablated tissue.

4.2 FBG sensors for temperature monitoring during NPs mediated *ex vivo* radiofrequency ablation

4.2.1 Introduction

In this study, we propose a solution to technological challenges of RFA through *in-situ* thermal profiling of ferromagnetic nanoparticles-enhanced RFA. Magnetic nanoparticles (MNPs) for medical application are getting great attention of researchers. Iron oxide nanoparticles are one of the few types of nanoparticles that are benign, nontoxic, and biologically tolerated [129]. These make injection into human body safe. The most common biocompatible magnetic nanomaterials are pure iron oxides, such as maghemite (γ-Fe_2O_3) and magnetite (Fe_3O_4).

The fields of biomedical applications of iron oxide nanoparticles, include magnetic resonance imaging (MRI), drug delivery, cell tracking, protein separation, and hyperthermia [130], [131].

An application of MNPs in thermal therapies, in particular, in RFA, relies on physical phenomena, such as Néel relaxation, Brownian relaxation [132], and a hysteresis loss mechanism and a method in which tumor cells are treated with the heat generated from MNPs in a high frequency field the heating mechanism is expected to depend largely on particle size. Small particles (10-40 nm) are preferred in hyperthermia application due to their ability to produce significant level of heating [133]. Due to the small size of therapeutic MNPs, of less than 100 nm, it is critical to confirm the biocompatibility of various MNPs in both *in vitro* and *in vivo* before conducting thermal ablation. Biocompatibility of MNPs was studied in several works [134], [135].

Accurate temperature monitoring during NP-enhanced ablation is of a greater importance than in a standard RFA scenario, because it addresses two tasks:

a. Estimate the thermal patterns in real time and therefore the size of the ablated tissue;
b. Investigate the effectiveness of NP based on the sizes of lethal isotherms;
c. Study different concentrations of NP solution and find the optimum value.

In this Section, we report a fiber Bragg grating (FBG) based sensing system for the real-time temperature profiling during a magnetite (Fe_3O_4)

nanoparticles (NP)-enhanced radiofrequency ablation (RFA). A minimally invasive RFA setup has been prepared and applied *ex vivo* on a liver phantom; NPs (with concentration of 5 mg/mL) were synthetized and injected within the tissue prior to perform the ablation, in order to facilitate the heat distribution to the peripheral sides of the treated tissue. A network of 15 FBG sensors, covering an area of 4.5 cm^2, was developed with the following objectives:

a. To detect the temperature distribution,
b. Estimate the thermal profiles in real time during the ablation, and the sizes of lethal isotherms;
c. To study the impact of MNPs injection on the heat propagation during RFA.

The results are presented in the form of thermal maps, i.e. temperature as a function of space and time. Results show that MNP-enhanced ablation with 5 mg/mL density achieves significant increase in heat propagation compared to the regular RFA, resulting in a double-sized lesion. Thermal data are reported highlighting both spatial and temporal gradients, evaluating the capability of NPs to deliver sufficient heating to the peripheral sides of the tumor borders.

In the following, we report nanoparticles synthesis and characterization (Subsection 4.2.2), the RFA and FBG measurement setup (Subsection 4.2.3), and the experimental results carried out with NP concentrations of 0, and 5 mg/mL (Subsection 4.2.4). The conclusions (Subsection 4.2.5) show that the FBG-based measurements highlight that RFA enhanced by NP with density of 5 mg/mL is more effective in spreading the heat to the peripheral areas of the tissue, resulting in a significant extension of the ablated tissue.

4.2.2 Nanoparticles synthesis and characterization

All chemicals used for the NPs synthesis are from Sigma-Aldrich and are of analytical grade. In the experiments we used magnetite nanoparticles (MNPs) synthesised by chemical precipitation from aqueous solutions of ferrous sulphate and iron(III) chloride. For the synthesis aqueous solutions containing Fe^{2+} ($FeSO_4 \cdot 7H_2O$, 99%) and Fe^{3+} ($FeCl_3 \cdot 6H_2O$, 97%) salts in the molar ratio Fe^{2+}/Fe^{3+} = 0.50 were mixed with sodium hydroxide (NaOH, 1.0 M). The process was conducted on the 80 °C hotplate. The solution was continuously

stirred until its pH reached 12. The precipitate was then centrifuged, washed several times with deionised water and dried in an oven at 105°C for 8 hours. XRD diffractogram (**Figure 4.1**) shows peak characteristics indexed to Iron Oxide, Fe_3O_4, Magnetite with cubic phase. The crystallite size was calculated based on XRD peak broadening using the Scherer equation. The reflection broadening at 35.4° computes the crystallite size to be 13.2 nm.

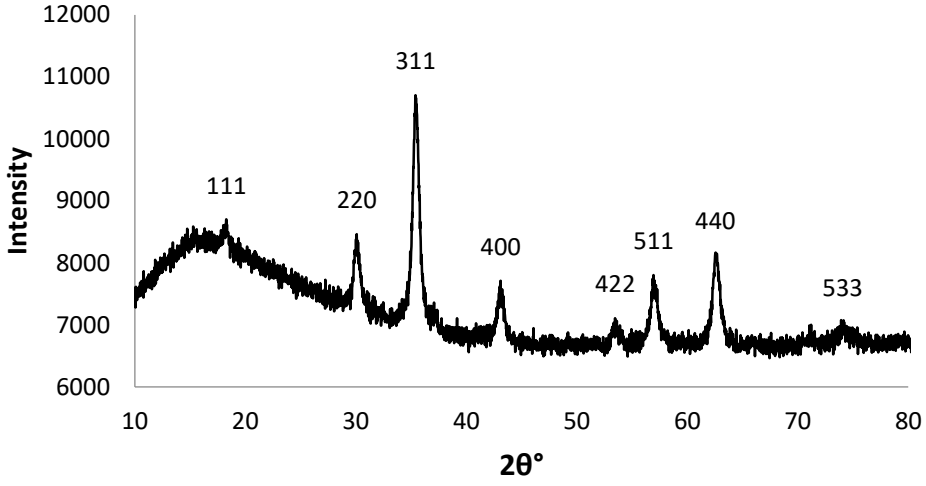

Figure 4.1 X-Ray powder diffractogram of synthesized magnetite nanoparticles.

High-resolution topographical characterization of MNPs was performed with Atomic Force Microscopy (AFM) SmartSPM 1000 (AIST-NT) in AC-Mode (non-contact mode) of AFM scanning. All the AFM measurements were carried out with a scan range 2500 nm in *X*-*Y* and up to 40 nm in *Z* direction with scanning rate 0.2 Hz. Mica ($K_2O{\cdot}Al_2O_3{\cdot}SiO_2$) multilayer substrate of 15 mm x 15 mm dimensions (NT-MDT, Russia) was used as a substrate reference sample before deposition of MNP solution. Prior to the scanning, chitosan solution of MNPs was dilute in water with concentration 1:10 and 1:100.

Figure 4.2 presents results of AFM scanning over the area of 2.5x2.5 μm. The overall distributions of MNPs are between 8 nm and 40 nm.

Nanoparticles injection

Currently two techniques are used to deliver MNPs to the tumor. The first is to deliver particles to the tumor vasculature through its supplying artery [136]. The second approach is to directly inject magnetic particles into the

extracellular space of tumor [137]. In this work we choose second approach of the nanoparticles admission to the tissue in order to improve MNPs distribution within the tumor (also in case of tumor with an irregular shape multiple-site injections can be exploited to cover the entire target region).

For all ablation experiments, magnetite particles were dispersed in chitosan solution (0.5 wt%, in 1.0% acetic acid, Sigma-Aldrich) and a dose of 0.1 mL was injected into the phantom using a syringe.

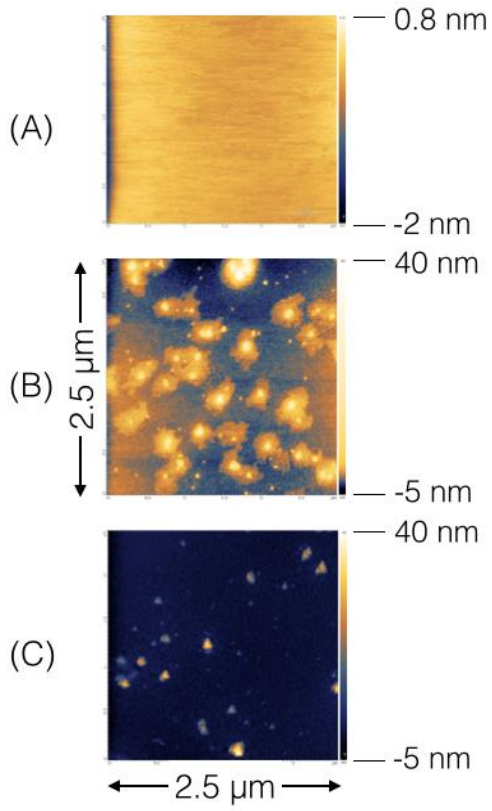

Figure 4.2 AFM topographical images in air of the synthesized magnetite nanoparticles (MNP); the data report the AFM images (2.5 μm × 2.5 μm) with 2D view. A) Mica substrate in absence of MNPs; B) images of MNPs diluted in solution 1:10 concentration water buffer; C) images of MNPs diluted in solution 1:100 concentration water buffer. The synthesized MNP are 8 nm - 40 nm size.

4.2.3 Experimental setup

Figure 4.3 presents a photo of the experimental setup, which combines thermal ablation device and a temperature measurement system. The custom-

made Hybrid RFA/MWA module (Leanfa, s.r.l.) was employed to perform thermal ablation; the module is comprised of RF 450 kHz electromagnetic power generator with maximum of power 100 W. Heat was delivered to the tissue through a solid brass laboratory-grade percutaneous applicator (160 mm length, 3 mm diameter) with a 5 mm conical active electrode (AE) on the tip. A second electrode presented by a metal plate served as a passive electrode (PE) and was placed underneath the liver phantom. **Figure 4.4**a displays a schematics of the experimental setup, and **Figure 4.4b** shows an arrangement of RF applicator and 3 FBG arrays for a total 15 FBGs providing temperature measurements within the surface area 10 mm×45 mm. This configuration allowed for the processing of two-dimensional thermal maps within the thermal ablation plane.

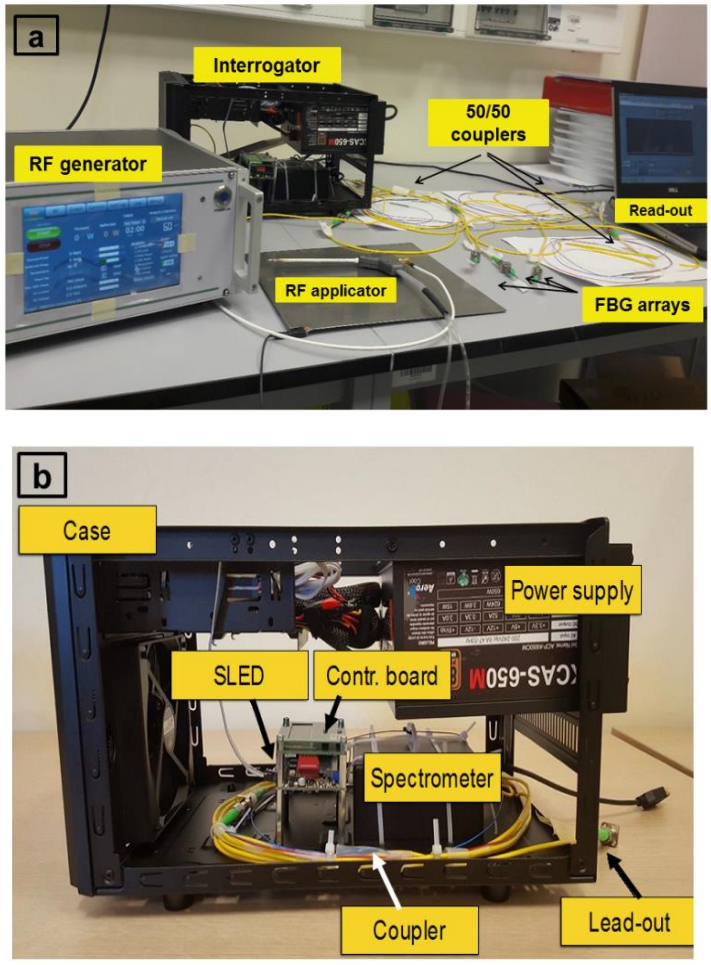

Figure 4.3 Photographic image of the (a) RF ablation and FBG measurement setup; (b) Custom-made interrogation system.

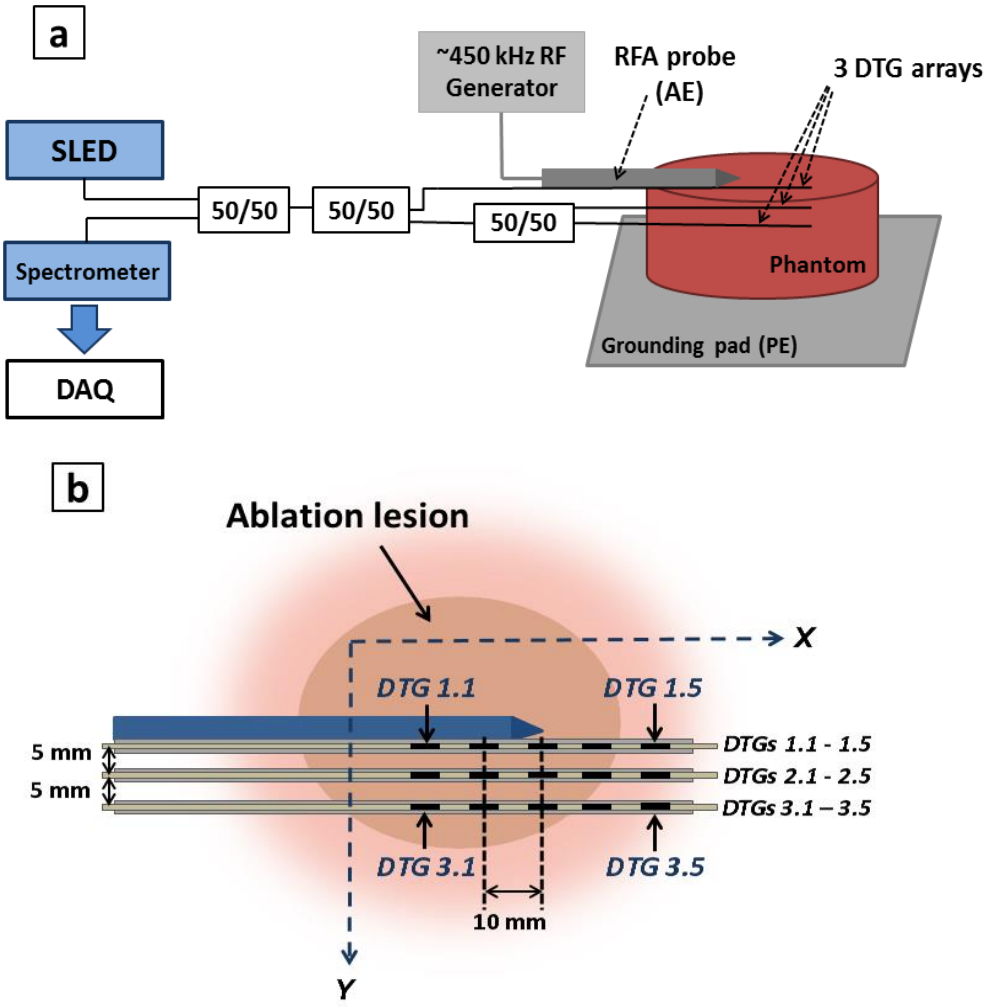

Figure 4.4 a) Schematics of the experimental setup for MNP-enhanced RFA; b) Positioning of the 15 FBGs arranged in 3 arrays on the *xy* plane.

Ablation experiments were performed *ex vivo* on a phantom of the porcine liver acquired from a local slaughter house. The meat was held at room temperature (~ 20 °C) right before the start of the experiment. The initial temperature of the tissue was measured with a contact thermometer (IKA ETS-D5).

The RF power has been set to 50 W for all experiments. Throughout the ablation process, the resistance of the tissue was monitored with an integrated impedance meter, and the values were displayed on the equipment User Interface. The initial resistance of the liver phantom was about 100-110 Ω. While the temperature of the tissue increased, its resistance was also

increasing, since the heated tissue becomes less capable of absorbing radiofrequency energy. The generator was operated in safe mode, meaning that the maximum resistance threshold was set at 300 Ω. The RF power is automatically switched off, when the measured resistance exceeds the threshold value. The initial tissue temperature has been measured with a contact thermometer (IKA ETS-D5).

Sensors positioning

The configuration of the fiber optic-based temperature measurement setup is made up of 3 FBG-based array structures that are positioned parallel to each other as shown in **Figure 4.4**b. The position of each of 15 DTGs can be described in terms of coordinates of the *XY* ablation plane, in which RFA tip corresponds to the origin of the coordinate system, X-axis is parallel to the RF applicator and Y-axis is perpendicular. The first FBG array was positioned at the closest proximity to the RF applicator, i.e at distance Y_1 = 0 mm, in order to detect the highest temperature values. The second and third optical fibers were located at distances Y_2 = 5 mm and Y_3 = 10 mm from the RFA probe respectively in such a way that the central (i.e third) DTGs of each array are aligned with the applicator tip (X = 0). Given that the size of each FBG is 5 mm, the rest gratings were located at distances X_2 = ±10 mm and X_3 = ±20 mm away from the tip. Such a configuration allows for real time temperature detection in 15 points of measurement within the surface area of 10 × 45 mm^2. The designed temperature measurement setup aims at the following:

- Studying heat propagation from the inner part of the ablation lesion to the peripheral locations.
- Building thermal maps, assuming the symmetrical heat propagation relative to the RF probe
- Analysing the effect on magnetite nanoparticles injection on the thermal profiles during RF ablation.
- Estimating 60 °C isotherms within the ablated areas and investigating their sizes at NPs concentrations 0 mg/mL and 5 mg/mL

The advantage of the proposed FBG sensors arrangement is to provide thermal patterns inside the whole ablation area surrounding the RFA tip and to measure the sizes of ablated volumes at different X coordinates: X_1 = 0, X_2 =

5 and X_3 = 10 mm. This configuration is an improvement with respect to previous designs, when the optical fiber was positioned either alongside the RF applicator [108] or in a perpendicular *Y* direction [54].

Each of 3 DTG arrays has been enclosed into a percutaneous 22-Gage catheter (Chiba Biopsy Needle DCHN-22-10.0, Cook Medical) [54]. The biopsy needle with a length of 100 mm was first inserted into a liver phantom, and was slowly pulled back after the insertion, while the optic fiber was left *in situ*. Using a biopsy needle mimics a percutaneous insertion of the RFA probe and fiber optic sensors in clinical conditions, and leads to an uncertainty of ± 0.5 mm on each coordinate.

This setup allows detecting the spectrum of the whole matrix of 15 FBGs, exploiting the wavelength division multiplexing. All FBGs of the setup have different wavelength, with ~2 nm spacing between each adjacent wavelength: this spectral spacing is sufficient to avoid overlap of FBG spectra during sensing. Data acquisition and recording has been performed with a LabVIEW™ code that acquires the FBG spectra and estimates all the Bragg wavelengths; the peak tracking method is the spline interpolation which has a good accuracy (~1 pm) despite the coarse wavelength resolution and allows fast operation (close to 100 Hz).

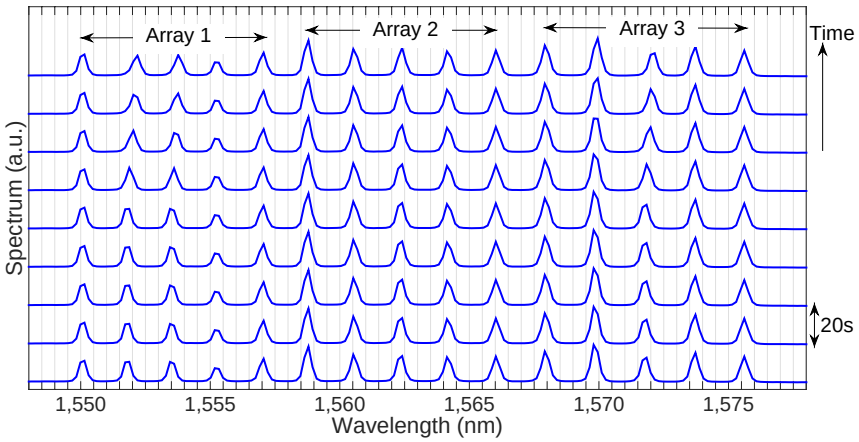

Figure 4.5 Spectra of the 15 FBGs arranged in 3 arrays, acquired every 20 s during a RFA experiment.

Figure 4.5 shows the principle of operation of the 15-FBG measurement system. The FBGs operate in WDM, visualizing with a single detection the

spectrum of the 15 gratings. The spectral shifts correspond to the temperature change measured at each of 15 locations within the ablated area.

Each DTG array used in our experiment has 5 gratings inscribed in ormoceramic optical fiber (DTG-15XX, FBGS International) with a grating length of 5 mm and 10 mm spacing between each DTG. The reflectivity of FBGs is 5-10%, as typically observed in short-length gratings inscribed via drawing tower process.

In this work we made use of the custom-made interrogation system (**Figure 4.3**) that was assembled in a case. A light source is a superluminescent LED source (SLED, Model EXS 2100, Exalos). The SLED light source has following electro-optical characteristics: maximum operating current 500 mA, center wavelength at 1550 nm, 20 mW emission power, and 60 nm bandwidth. SLED drive current is controlled by an EBD 5200 driver board (Exalos, ~600 mA drive current). Parallel connection of the optical fibers was realized through a network of 3 50/50 couplers, as sketched in **Figure 4.4**. Light from SLED was routed to all 3 FBG arrays through the couplers, and the back reflected light was detected with a low-cost infrared spectrometer (I-MON-512 USB, Ibsen Photonics). The optical range of the spectrometer is 1520-1600 nm, with wavelength resolution of 156 pm and 512 sampling points on the wavelength grid. As shown in **Figure 4.3**a, all the components of the FBG interrogation system are packaged in a portable box. All 15 DTGs used in our experiments have different Bragg wavelengths, with ~2 nm spacing between two adjacent wavelengths; such a spectral spacing allows to avoid spectral overlapping during sensing. Data acquisition and processing have been performed with a LabVIEW code and a spline interpolation was used for a peak tracking as described in [110]. The acquisition speed of the setup is ~100 Hz. The exposure time of the spectrometer has been set to 9 ms.

FBGs calibration

Prior to temperature measurements, each FBG was calibrated in order to calculate temperature sensitivity k_T. From Equation (3.4) k_T can be calculated as a relationship between $\Delta\lambda_B$ and ΔT. The following experimental setup was prepared to perform a sensor calibration: a custom-made environmental chamber, a contact thermometer, FBG array, and interrogation system

described previously. FBG array was placed in the chamber within which temperature was controlled with the electronic contact thermometer (IKA ETS-D5 electronic contact thermometer). The calibration testing was executed in a temperature range between 25 °C and 75 °C, with temperature interval 10 °C. During the calibration, the Bragg wavelength λ_B of each FBG was detected with the spectrometer. The results are presented in Figure 4.6, that shows the wavelength shift of the FBGs $\Delta\lambda_B$ as a function of the temperature T. Temperature sensitivity was defined as the ratio $k_T = \Delta\lambda_B / \Delta T$ (Equation 3.4) and was estimated as k_T = 13.07 pm/°C, which is close to manufacturer's specification. The same k_T coefficient was observed also for the other two FBG arrays. The uncertainty in the measurement is mainly due to possible hysteresis of the reference sensor and uncertainty in heat transfer from the water to the sensors.

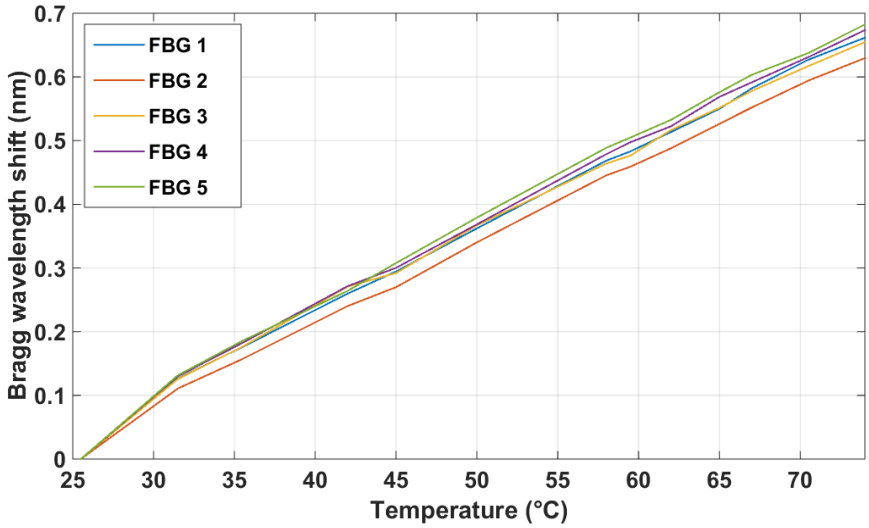

Figure 4.6 Calibration functions for the FBG sensors; the chart reports the wavelength shift as a function of the applied temperature for the first array of the FBGs during a temperature cycle in a water bath.

4.2.4 Results and discussion

Experiments have been carried out in absence of MNPs, and enhancing the RFA with 0.1 mL of 5 mg/mL MNP solution. The photographic results of the ablations are shown in **Figure 4.7**; the ablated tissue has been separated and the photographs show qualitatively the extension of the parenchymal lesion.

The results of thermal profiling before and after injection of nanoparticles, are presented as the charts reporting the temperature reading of each individual FBG, with respect to the applicator tip position and the 60 °C damage threshold. Further, thermal maps are presented obtained by reporting the temperature as a function of space and time in a contour chart with the methodology outlined in previous study.

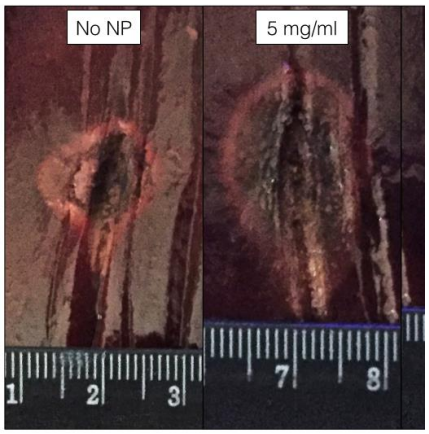

Figure 4.7 Photographs of the RF-ablated lesions in the liver phantom, in absence of NP and after injection of 5 mg/mL concentration. The ruler shows cm units.

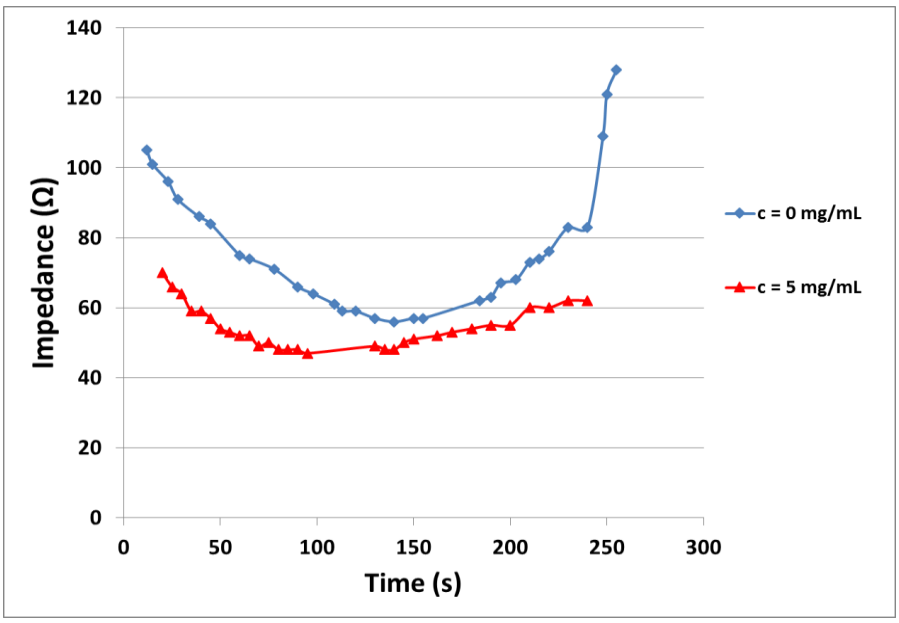

Figure 4.8 Tissue impedance recorded with the impedance meter throughout the RFA.

Impedance of the tissue was measured during the ablation processes. **Figure 4.8** shows the results, the charts show confirm that loading MNPs allow to increase the conductivity of the tissue, thus facilitating the heat propagation and to increase the ablated area.

Experiments started with the regular RF ablation, with no nanoparticles injected in the tissue; the temperature traces recorded by 15 FBGs are displayed in **Figure 4.9** in the time domain. The line indicating 60 °C is plotted for the reference. The experiment duration is 154 s. As was observed in the research by Tosi et al. [111], temperature rises rapidly in the area closest to the applicator tip (recorded by FBG 1.3), and reaches 60 °C threshold after 13 seconds. The peak temperature has a value of 157.8 °C; this value is high than due to the larger RF power delivered to the tissue. Moving along *y*, the central FBG of the second array records a peak temperature of 113.0 °C, while the third FBG exhibits a peak temperature of 108.8 °C.

After the inner part of the tissue reaches the peak value, the tissue impedance rises over 300 Ω reducing the RFA efficiency. Overall, after 100 s, temperature values appear to stabilize. Moving along *x*, only the FBG positioned in (-10, 0) mm reaches the damage threshold value, while at the peripheral side of the tissue we observe a heating pattern that does not reach the threshold.

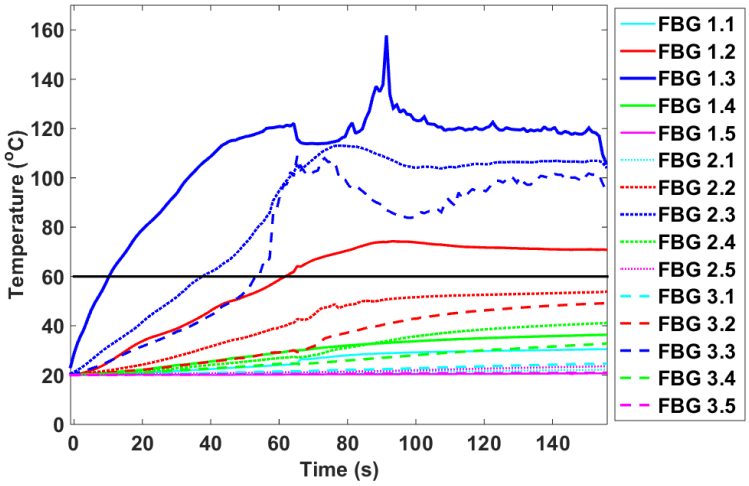

Figure 4.9 Temperatures recorded by FBG sensors during RFA (no nanoparticles). The legend shows each of 15 FBGs label according to its position inside the 3 arrays.

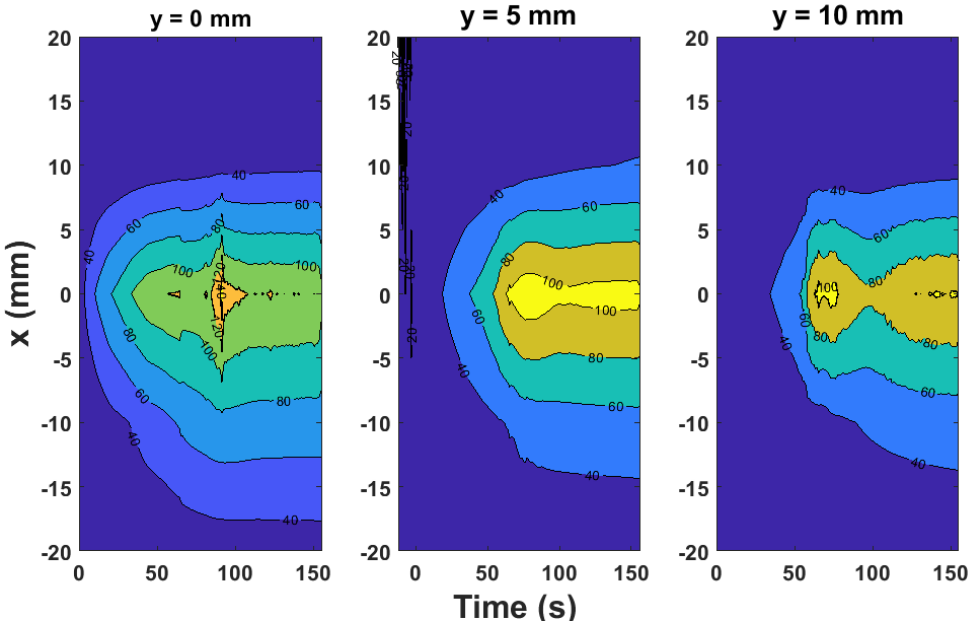

Figure 4.10 Thermal maps for RFA experiments (no nanoparticles injected). Temperature levels are presented in °C as a function of *x* and time for the first (left, *y* = 0 mm), second (center, *y* = 5 mm) and third (right, *y* = 10 mm) FBG arrays.

Temperature data are summarized in **Table 4.1**, providing values for all FBGs for the two ablation procedures.

Figure 4.10 reports the thermal maps obtained for the NP-free experiment. Thermal map provides isotherms as a function of time and *X*-*Y* plane, where *X* is the distance along the optical fiber, and *Y* is the direction perpendicular to the RF probe. Thermal maps are effective in showing the propagation of heat on the ablation plane.

After the initial rise, the temperature exhibits a fast growth near the ablation peak and then stabilizes, as for the smaller *y* values the contours are almost parallel to the horizontal axis after 100 s. Heat is however still propagating on the border of the tissue, as the temperature field is still expanding for *y* = 10 mm when the procedure is discontinued. Overall, with this interpolation method we estimate that the diameter of fully ablated area is 20 mm for *y* = 0 mm, 16 mm for *y* = 5 mm, and 12 mm for *y* = 10 mm.

Table 4.1 Peak temperatures and damage threshold for the FBG sensors.

		FBG 1.3	FBG 2.3	FBG 3.3	FBG 1.2	FBG 1.4	FBG 2.2	FBG 2.4	FBG 3.2	FBG 3.4
No NPs	Time to reach 60 °C, s	11	38	54	62	-	-	-	-	-
	Peak temperature, °C	157.8	113	108	74.3	-	53.5	-	49	-
5 mg/mL	Time to reach 60 °C, s	13	9	51	-	7	36		101	
	Peak temperature, °C	114.8	122	112.5	100	129	110	100	101.6	53

The results of MNP-mediated ablation with 5 mg/mL density are shown in **Figure 4.11**, and differ qualitatively and quantitatively from the regular ablation. At first, we observe that the maximum heating is obtained on the FBG elements positioned in front of the RFA tip (x = 10 mm) rather than in the central position. This is due to the NP effect that contributes to reduce the average electrical impedance of the tissue and support a heat propagation to the peripheral areas. The relatively fast heating occurs for multiple FBGs, and the consequence is that 8 FBG sensors out of 15 record temperature peaks higher than 60 °C. All FBGs located at x = 0 and -10 mm and two FBGs located at x = 10 mm reach the damage threshold, and overall we can observe that the cytotoxicity region has significantly expanded with respect to **Figure 4.9**. The duration of the experiment is 172 s and is longer than previous ablation; this is in part due to the effect of the ferromagnetic material, that by reducing the average impedance during the most intense RFA heating prevents early disconnections of the RFA power, with the consequence that the heat is delivered to the peripheral regions in a much deeper way. This is confirmed by the reduced peak temperature value (143.2 °C) which prevents a fast vaporization of the inner tissue [117].

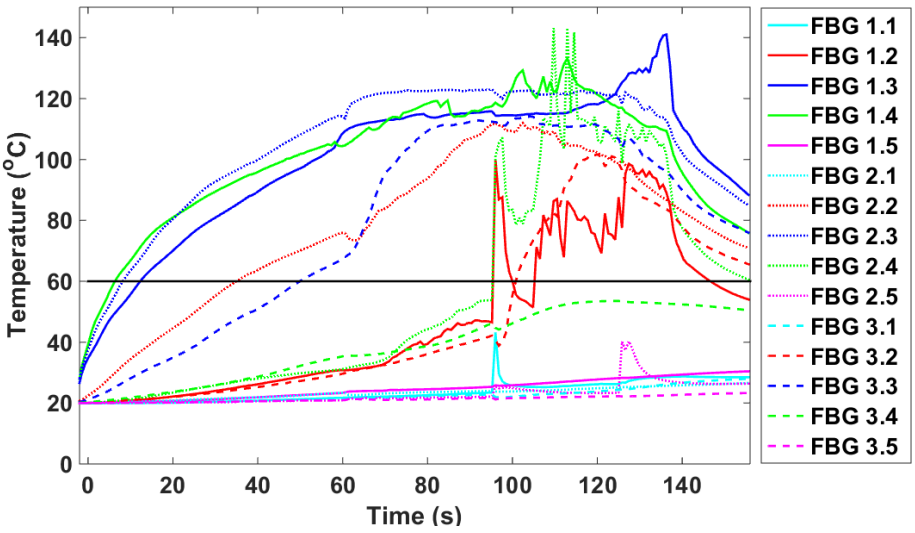

Figure 4.11 Temperature recorded by FBG sensors during MNP-enhanced RF ablation (5 mg/mL density of MNPs). The legend shows each of 15 FBGs label according to its position inside the 3 arrays.

This analysis is complemented by the thermal maps, shown in **Figure 4.12**. We immediately observe that the thermal fields are substantially enlarged with respect to **Figure 4.10**, due to the beneficial effect of the NP. At y = 0 mm, the extent of the >60 °C is approximately 28 mm, and almost same value (25 mm) is observed at y = 5 mm. At y = 10 mm the tissue extent exceeding the damage threshold is 24 mm, and overall the size of the ablated volume during MNP enhanced ablation is 60% larger than without applying NP solution.

We observe also a different pattern in heating: the first two FBG arrays detect a rapid heating throughout the tissue, a thermal plateau where the temperature is almost steady, and a region of rapid heating and cooling that was not observed in the previous experiment. This can be partially due to oscillations of the tissue impedance that are induced in the RF circuit.

We also observe that when the RF power is discontinued (174 s), the deeper part of the tissue recorded by the third FBG array has already started cooling, which appears to suggest that the system has a limitation of its effectiveness in spreading the heat. Overall, it is clear by the comparison of thermal maps that NP with a density of 5 mg/mL act as an enhancement of the ablation effect: heat is successfully spread to the peripheral sides of the tissue, a

condition necessary to ablate larger tumors, and it has been possible to obtain a lesion >3 cm in diameter even with a single RFA applicator with one electrode.

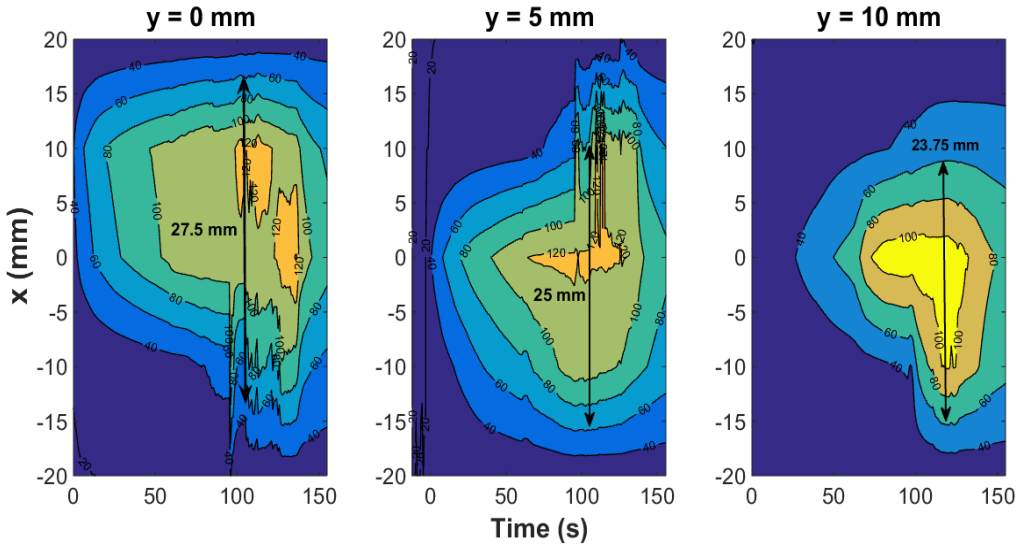

Figure 4.12 Thermal maps for MNP-mediated RFA experiments (5 mg/mL concentration). Temperature levels are presented in °C as a function of *x* and time for the first (left, *y* = 0 mm), second (center, *y* = 5 mm) and third (right, *y* = 10 mm) FBG arrays. Double arrows indicate the diameter of 60 °C isotherm.

4.2.5 Conclusions

We presented a FBG-based sensing system for the real time thermal profiling of *ex vivo* RFA enhanced by ferromagnetic nanoparticles (Fe_3O_4, Magnetite), for interventional cancer care. A network of 15 FBG sensors has been deployed in order to measure the thermal patterns within the tissue in an *ex vivo* RFA setup. The effect of injecting MNP solution was observed on both mitigating the tissue impedance and altering the heat propagation properties. The time-domain temperature charts, and the thermal maps, show a significant impact of NP in moderate density (5 mg/mL) with respect to a standard RFA:

- the portion of tissue exceeding the damage threshold increases significantly, approaching the 28 mm diameter in the near-applicator area;

- the ablated volume reaches 25 mm and 24 mm at the distances y = 5 mm and y = 10 mm from the RF probe, respectively, even with a single-tip RFA applicator;
- NPs improve delivering the heat to the peripheral sides of a tumor.

This is a significant achievement for RFA as it enables the treatment of larger tumors with a minimally invasive applicator: thermal maps show that NP-enhanced RFA can achieve a lesion having extension approximately twice larger than in absence of NP.

4.3 Fiber Bragg grating sensors for temperature profiling during NPs mediated *ex vivo* microwave ablation

4.3.1 Introduction

Chapter 2 presented the overview of the microwave ablation procedure, its working principles. The inherent tissue inhomogeneity and the heat sink effect due to blood flow limit the ability of MWA to create large necrotic lesions [138]. In order to facilitate heat propagation towards the outer borders of the tumor, thus maximizing the volume of complete cell death, a functional solution with nanoparticles is injected into the target tissues. Such methodology makes use of the fact that liquids containing metallic or nonmetallic nanoparticles have higher thermal conductivity compared to that of the base liquid [139], [140]. Following this approach, gold nanoparticles have been applied to enhance thermal ablation in the kidney [141], while an efficient treatment of lung carcinoma was demonstrated by utilizing Si nanoparticles during radiation-induced hyperthermia [125].

Overall, loading nanoparticles into the tumor affects both electrical and thermal conductivities of the tissue [142], [143], improving the efficiency of conventional thermal ablation techniques without burning the healthy tissue adjacent to the tumor. In this work we demonstrate, through *in situ* temperature profiling, the feasibility of applying ferromagnetic nanoparticles to enhance the efficiency of MWA. Iron oxide magnetite nanoparticles have shown biocompatibility both *in vitro* and *in vivo* [135], [144], and have been used in various clinical applications, like drug delivery, thermal marking of tumor and cryosurgery.

In this Section, we report a fiber Bragg grating (FBG) based sensing system for the real-time temperature profiling during a ferromagnetic nanoparticles (NP)-enhanced microwave ablation (MWA). A minimally invasive MWA setup has been prepared and applied *ex vivo* on a porcine liver phantom; MNPs (with concentrations of 2 mg/mL and 5 mg/mL) were synthetized and injected within the tissue prior to perform the ablation, in order to facilitate the heat distribution to the peripheral sides of the treated tissue. A network of 15 FBG sensors, covering an area of 4.5 cm^2, was developed with the following objectives:

a. To detect the temperature distribution,
b. Estimate the thermal profiles in real time during the ablation,
c. To study the impact of MNPs injection on the heat propagation during MWA.

The results are presented in the form of thermal maps, i.e. temperature as a function of space and time. Results show that NP-enhanced ablation achieves significant increase in heat propagation compared to the regular MWA, resulting in extended ablation lesion. Thermal data are reported highlighting both spatial and temporal gradients, evaluating the capability of NPs to deliver sufficient heating to the peripheral sides of the tumor borders.

In this study design of the experiment was similar to the setup reported in section 4.2 of this Chapter. Here, we will omit the description of the FBG measurement setup, sensors calibration, nanoparticle synthesis and characterization, as those have been mentioned in the section related to NP-enhanced RFA. The difference is in the generator; in this work a MW generator was a custom-made MW module operating at 2.45 GHz (Leanfa Hybrid Generator). A solid brass percutaneous applicator of 16 cm length and 3 mm diameter is connected to the generator; the MW power was set to 60 W for all experiments. Ablation experiments were performed *ex vivo* on a porcine liver obtained from a local slaughter house. The meat was held at room temperature (~ 20 °C) right before the start of the experiment. The initial temperature of the tissue was measured with a contact thermometer (IKA ETS-D5).

Thermal ablations were performed in the absence of MNPs, and with concentrations 2 and 5 mg/mL.

4.3.2 Results and discussion

In this study, three microwave ablations were carried out, each experiment on a virgin part of the phantom: the first one in absence of nanoparticles, and then after injecting NP solutions of 2 mg/mL and 5 mg/mL concentrations. The photographic images of the liver tissue, as shown in **Figure 4.13**, demonstrate that adding NPs solution helps extend ablation lesions in the direction perpendicular to the applicator. The observed increase in the lesion diameter as compared to pristine ablation is 2 mm in case of 2 mg/mL NPs concentration, and 6 mm for the solution of 5 mg/mL concentration.

Temperature evolution throughout the ablation process is reconstructed based on the spectral data obtained from all 15 FBGs. We also illustrate contour charts of temperature as a function of time and space using the methodology proposed in previous works [54], [55].

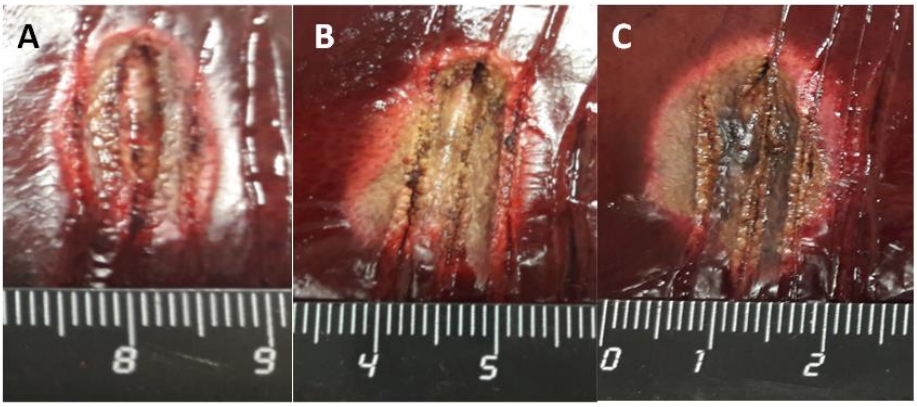

Figure 4.13 Photographic images of the tissue undergoing MWA: a) no NPs injected, b) with 2 mg/mL NPs concentration, and c) with 5 mg/mL NPs concentration. The ruler shows cm units.

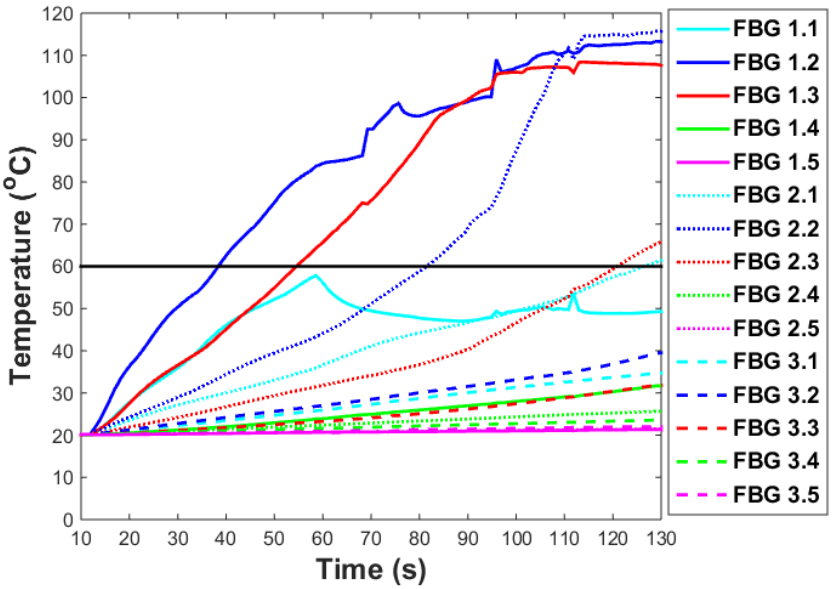

Figure 4.14 Temperature recorded by FBG sensors during MW ablation (no nanoparticles injected). The legend shows each FBG label according to its position inside the 3 arrays.

The first ablation was performed for 120 seconds without loading NP solution; temperature records are presented in **Figure 4.14**. For convenience, all FBG sensors are labelled according to their positions on a particular sensor array: FBGs 1.1 to 1.5 are located on the first array at the zero distance from the microwave probe. In the same way, sensors labelled 3.1 to 3.5 are positioned on the third array at the maximum y = 10 mm distance from the applicator.

Tissue close to the applicator tip is heating evenly and at 38 s the temperature reaches 60 °C threshold. After 110 s temperature reaches maximum value of 112 °C and then stabilizes. Moving away from the MWA probe at distance y = 5 mm, only one sensor records the excess of the damage threshold, and the peak temperature is 115 °C. Heat propagation to the peripheral side of the ablation area is very poor and none of the sensors exhibit the values higher than 35 °C. The analysis of heat propagation on the ablation plane is presented in **Figure 4.15** in the form of thermal maps for three distances y = 0 mm, y = 5 mm, and y = 10 mm from the MWA applicator. The fastest temperature growth is observed close to the applicator tip, where the tissue is heated to 60 °C within 38 s. The heat is propagating in the lateral direction 5 mm away from the probe and the temperature here rises up to 60 °C after 80

s. The amount of heat spreading to the distance *y* = 10 mm, however, is not sufficient to warm up the tissue more than 38 °C. Overall, with this interpolation technique the volume of successfully ablated tissue can be estimated and it is 24 mm at *y* = 0 mm, and 21 mm at *y* = 5 mm.

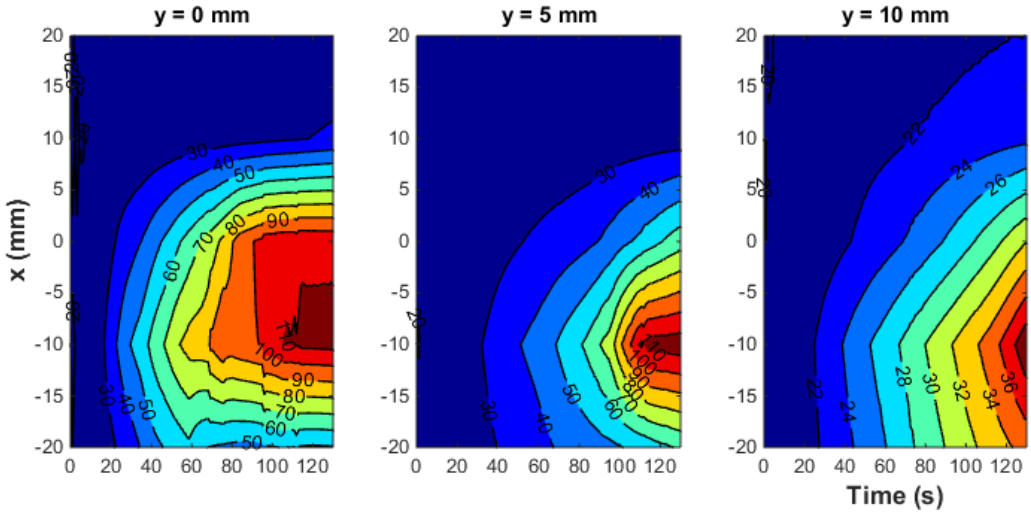

Figure 4.15 Thermal maps for MWA experiments (no nanoparticles injected). Temperature levels are presented in °C as a function of *x* and time for the first (left, *y* = 0 mm), second (center, *y* = 5 mm) and third (right, *y* = 10 mm) FBG arrays.

Subsequently, thermal profiling is presented for the ablation enhanced with 2 mg/mL density nanoparticle solution. **Figure 4.16** demonstrates significant changes in the way temperature is distributed within the ablation zone. First, temperature rises faster within the whole lesion, and 60 °C threshold is reached in 19 s from the start of ablation. FBG 2.2 of the second array, located at *y* = 5 mm from the ablation probe, records the threshold temperature at 51 s and the temperature keeps increasing until it reaches the peak of 113 °C. Moreover, a sensor positioned in (10, 5) exhibits a steep temperature rise with a peak value of 100 °C, meaning that the cytotoxicity region is expanded after nanoparticles are injected. The temperature plateau observed after 40 s, whereas the central temperature stabilizes while in the surrounding regions the heating progresses, is a good validation of the NP-mediated MWA, and is in agreement with [53]: in this case, the ablated region expands while the peak temperature is mitigated, avoiding excessive heating.

Thermal maps obtained for the NP-mediated MWA are shown in **Figure 4.17** and they confirm that NPs contribute to the extension of ablation lesion. At distance y = 0 mm the successfully ablated region extents to 26 mm, while at y = 5 mm this size is 25 mm. These values demonstrate 20% increase in the ablation area with respect to pristine MWA.

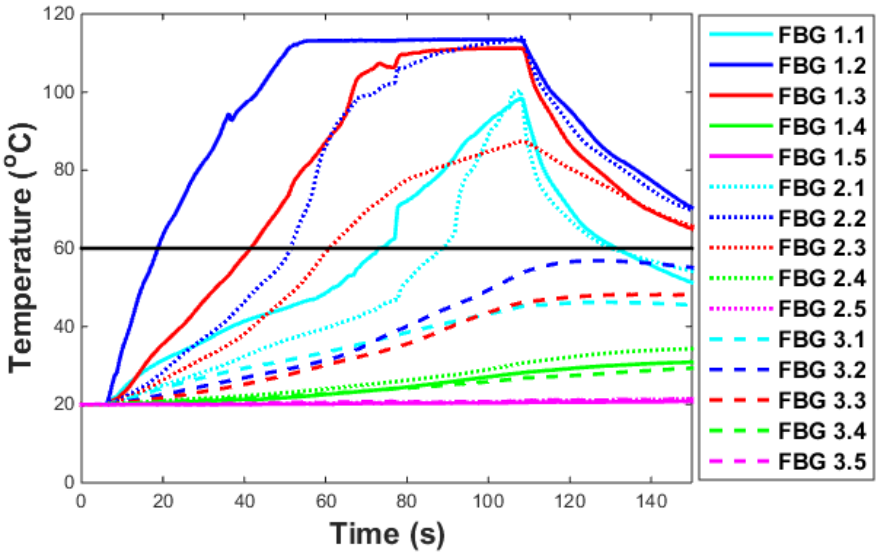

Figure 4.16 Temperature recorded by FBG sensors during NP-enhanced MW ablation (2 mg/mL MNPs concentration). The legend shows each FBG label according to its position inside the array.

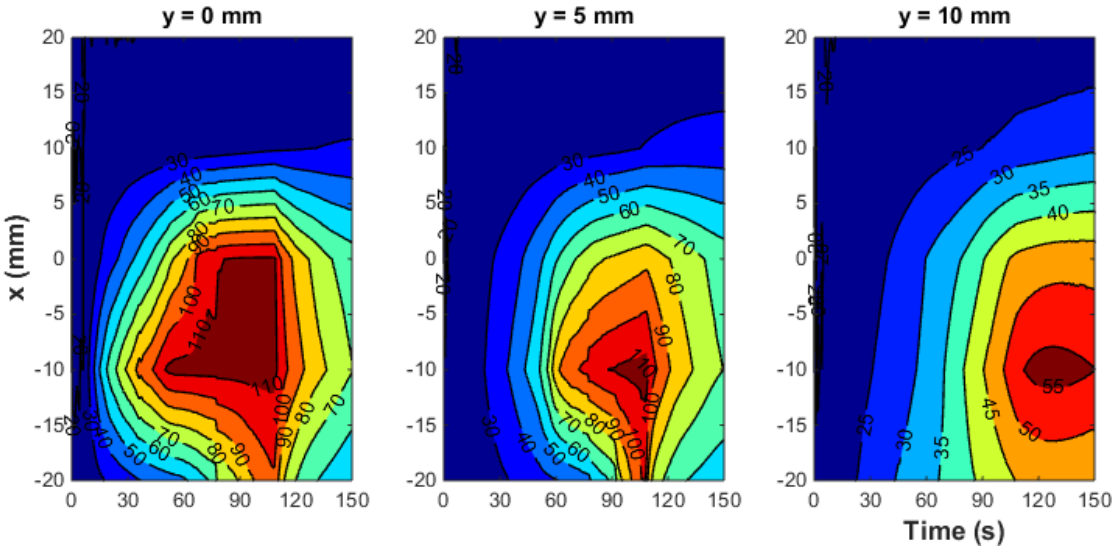

Figure 4.17 Thermal maps for NP-enhanced MWA experiments (2 mg/mL MNPs concentration). Temperature levels are presented in °C as a function of x and time for the first (left, y = 0 mm), second (center, y = 5 mm) and third (right, y = 10 mm) FBG arrays.

The results of thermal profiling during MWA enhanced with 5 mg/mL nanoparticle solution are shown in **Figure 4.18**. Temperature behaviour demonstrates that such nanoparticle density is more efficient than 2 mg/mL density in terms of heat propagation towards the peripheral sides of the lesion. The first two FBG arrays, positioned at y = 0 mm and y = 5 mm, detect a rapid temperature growth, a plateau with almost constant temperature and then cooling after 100 s. The heating occurs faster compared to the 2 mg/mL NPs concentration: the first FBG array indicates that area closest to the applicator heats up to 60 °C in just 15 s, and FBGs located at the furthermost array (dashed lines) exhibit temperature as high as 86.4 °C. Another important fact is that eight sensors out of 15 detect a temperature higher than the damage threshold, and the damage threshold is reached at y = 10 mm in 67 s.

Thermal maps obtained for the MNP-mediated MWA (5 mg/mL concentration) confirms the results of temperature profiling. Thermal contour charts shown in **Figure 4.19** demonstrate that the heat propagates outwards the center of ablation and the temperature raises up to 80 °C at the distance y = 10 mm from the MWA applicator tip. The lethal isotherms extend to 16 mm in diameter at distance y = 10 mm.

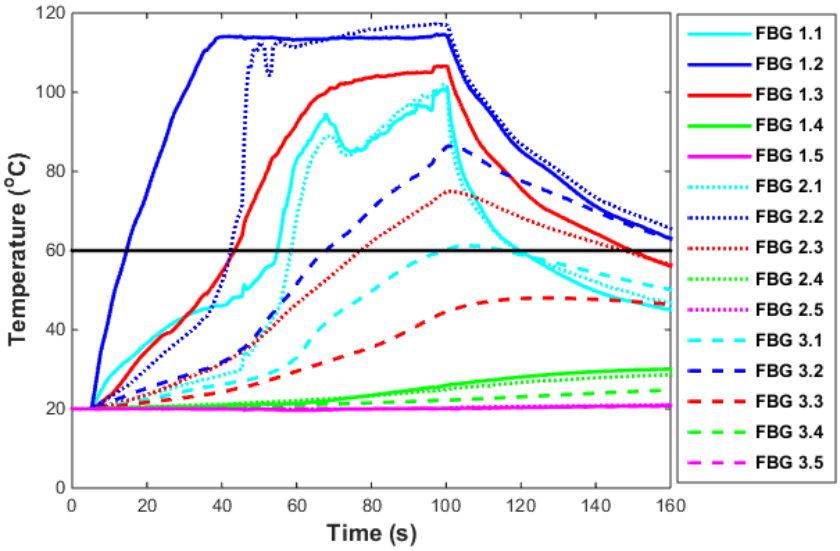

Figure 4.18 Temperatures recorded by 15 FBG sensors during MNP-mediated MW ablation (5 mg/mL MNPs concentration). The legend shows each FBG label according to its position inside the array.

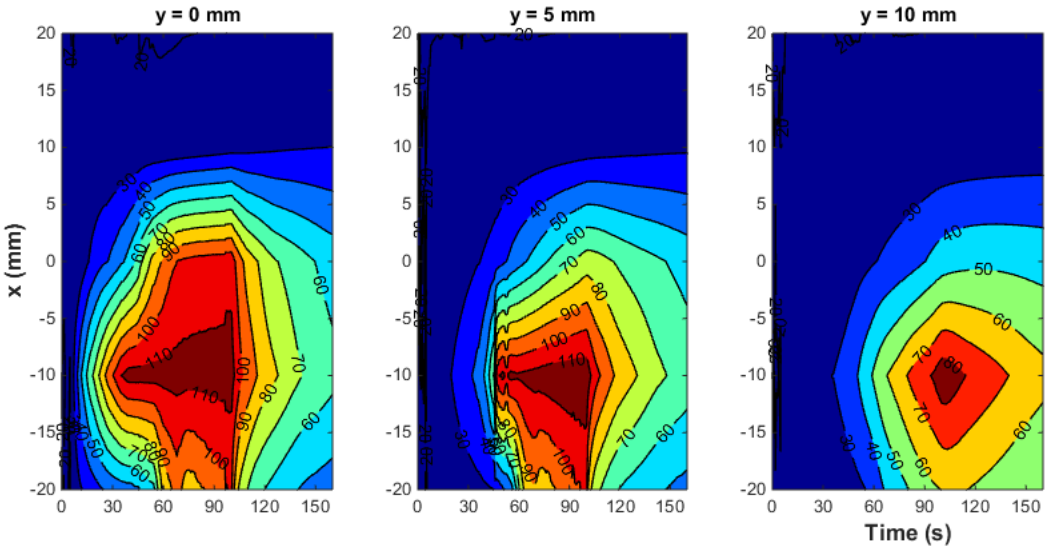

Figure 4.19 Thermal maps for NP-enhanced MWA experiments (5 mg/mL MNPs concentration). Temperature levels are presented in °C as a function of *x* and time for the first (left, *y* = 0 mm), second (center, *y* = 5 mm) and third (right, *y* = 10 mm) FBG arrays.

4.3.3 Conclusions

This section reported a setup comprised of 3 arrays of total 15 FBG sensors for the real-time detection of tissue heating during nanoparticle-enhanced microwave ablation. The setup has been arranged in order to measure the temperature profiles over the length of 450 mm, and at three different distances from the MWA applicator. The proposed FBG system configuration provides information about how the temperature is distributed from the center to the periphery of the ablated area. MWA procedure has been enhanced through *in situ* injection of a solution of magnetite nanoparticles that allow a better heat propagation into the external sides of the tissue.

The results show both the effectiveness of FBG sensors to measure the temperature profiles, and an increased depth of heat penetration achieved with MNP with respect to the absence of nanoparticles. The sensor network can detect an increased amount of ablated tissue that has been observed for a density of 5 mg/mL. In this case, the largest ablated volume has been achieved for a short term ablation. The inherent lack of repeatability of thermal ablation is due to the variability of electrical and thermal properties of the tissue, as well as the imprecisions of nanoparticle spatial distribution. These limitations require an *in situ* network of sensors that can render thermal maps

in real time in order to estimate, for each MWA, the correctness of the procedure.

To the best of our knowledge, this is the first study that aims at thermal profiling *in situ* for a microwave ablation treatment enhanced by nanoparticles. Fiber optic sensors, which is the only technology capable of sensing in this measurement environment, provide a real-time detection of thermal maps that render the heating spreading into the tissue.

Future work will address an optimization of MNP density and injection methodology, as well as the catheterization of a device that embodies the MWA applicator, FBG sensors, and the nanoparticle injection.

4.4 Conclusions

In this Chapter FBG-based sensing setup was proposed for the real-time thermal profiling of RFA and MWA enhanced by 0.1 mL aqueous solution of nanoparticles (Fe_3O_4, Magnetite). Results demonstrated the impact of MNPs injection on both mitigating the tissue impedance and altering the heat propagation properties.

This is a significant achievement for percutaneous TA as it enables the treatment of bigger tumor regions with a minimally invasive applicator: thermal maps show that MNP-enhanced RF ablation achieves a lesion having extension approximately twice larger than in absence of NP; and in case of MWA lethal isotherm is enlarged by 20%. The results are significant because, to the best of our knowledge, they report the real-time effect of NPs in the most appropriate format, i.e. analysing the spatial distribution of temperature, rather than simply analysing the damaged tissue via imaging (prior and after the treatment) or using a colorimetric phantom; the role of FBG sensors is therefore essential for evaluating the procedure from the heat propagation perspective, but also as a key indicator for the clinician of successful treatment or as a tool for terminating the RFA procedure when the target ablation size has been achieved.

The results suggest that there is an optimum density of NP that maximizes the heat distribution to the peripheral sides of the tumor. Future work will address the engineering of NP-enhanced RFA; in particular, it is important to

investigate the optimum NP density as a function of the RF power at the generator, for different typologies of tissues. Further effort will be also given to the reduction of the spatial resolution of fiber optic sensors. The present setup operates at the limit of FBG length and FBG spacing (5 mm and 10 mm respectively) for a draw-tower grating array, which is a good trade-off between FBG spacing, accuracy of the FBG location, reflectivity, and need to maintain the fiber protective coating to sustain the penetration and extraction from the tissue. Future work will explore optical frequency domain reflectometry to RFA setup enhanced by RF to evaluate *ex vivo* the thermal field with a narrower resolution.

CHAPTER 5

Thermal profile detection with chirped fiber Bragg grating on microstructured PMMA fiber

This Chapter reports a linearly chirped fiber Bragg grating (CFBG) inscribed in a microstructured polymer optical fiber (mPOF) for measuring temperature profiles during *ex vivo* thermal ablation. A 10 mm CFBG was fabricated on an mPOF fiber by means of a KrF laser and uniform phase mask. The Chapter presents results of two experiments validating the CFBG temperature reconstruction: first experiment involved a linear temperature gradient, and a second - research-grade RFA setup to apply Gaussian-shaped temperature spatial profiles. Results show that the higher sensitivity of the mPOF CFBG allows detection of spatially non-uniform temperature fields.
The work presented in this Chapter was published in [145].

5.1 Introduction

The principle of percutaneous minimally invasive thermal treatment, whether it is RFA, MWA or laser ablation, is to induce a highly spatially confined heat field into the target tissue to cause coagulative necrosis of the tumor. Due to the small dimensions of the percutaneous applicator, thermal gradients produced by the electromagnetic energy have slopes reaching 3-5 °C/mm in space and 1 °C/s in time [85], [99]. Steep temperature gradients are also recorded during blood temperature measurements performed in laser treatment and intravascular interventional surgery [146]. In order to conduct thermotherapies in a more efficient way, there is a high demand for the compact biocompatible temperature sensor that provides sub-centimeter spatial resolution within the ablation lesion (10-50 mm).
Linearly chirped FBGs (CFBGs), as was concluded in Chapter 3 of the Thesis book, provide the possibility of a dense thermal profiling and, thus, are

suitable to measure temperature distribution with a sub-millimeter resolution [99], [147]. The whole length of the CFBG presents a continuous sensing region, and the reflection spectrum of CFBG is dependent on the temperature (or strain) pattern experienced in each point of the active area [148].

While early works have reported the use of CFBGs as mechanical strain sensors, and for the crack detection [149], [150], recent studies discussed the feasibility of using chirped FBG sensors in biomedical fields. In particular, CFBGs have potential in thermal ablation therapies, which require dense thermal profiling [52], [85]. Spatial resolution of 0.25 mm was achieved with a chirped FBG during temperature measurements in *ex vivo* laser induced interstitial thermotherapy (LITT) [151]; high bandwidth (> 40 nm) CFBG sensor system was proposed to detect temperature distribution in RFA [55].

In previous chapters of the Thesis book, we discussed fiber optic sensor systems, such as FBG and CFBG sensors, based on the silica optical fibers. However, drawbacks of silica optical fibers, such as low flexibility, and risks of accidental breakage, make scientists and engineers to search for the alternative materials for the fibers. In terms of temperature sensitivity, FBGs and CFBGs fabricated on glass fibers, typically provide sensitivity about 10 pm/°C, hence, a small temperature variation result in a barely detectable spectral shift. Polymer optical fibers (POFs) demonstrate excellent properties which we don't observe in glass fibers, such as low Young's modulus (about 3.3 GPa for PMMA fibers), high failure strain, greater flexibility, and resiliency to bending and vibration [152]. Another significant advantage makes POFs applicable for *in vivo* medical applications, for example, sensing: polymer fibers do not produce dangerous sharps in case of breakage. All these characteristics make polymer fibers a lower cost alternative to glass fibers at medium distances and bit rates of 10 Gb/s. POFs are mostly fabricated from polymethyl methacrylate (PMMA) [153], however a variety of other optical polymeric materials have been investigated, each offering specific advantages.

Another important area of research, and also the focus of this Chapter, is POF-based sensors. Peters et al. [154] presented a review work focused on strain and temperature sensing applications, based on POFs using different solutions. Recent works reported CFBGs inscribed in PMMA optical fiber with

sensitivity ten times higher compared to the SMF silica fibers: Marques *et al.* [155] fabricated a CFBG on a step-index POF achieving thermal sensitivity of -131 pm/°C; Min *et al.* [156] demonstrated a BDK-doped (benzyl dimethyl ketal) CFBG inscribed on a microstructed POF (mPOF) with a high sensitivity (-57 pm/°C).

This Chapter provides a novel approach for measuring thermal profiles during RF ablation. A linearly chirped fiber Bragg grating (CFBG) inscribed in a microstructured polymer optical fiber (mPOF) by means of a KrF laser, has been used to detect temperatures during thermal treatments. CFBG temperature reconstruction was validated during two experiments, one involving a linear temperature gradient, and another one – using a RF ablation device, to detect Gaussian profiles. The Chapter is arranged as follows: Section 5.2 covers inscription method and characterization of the mPOF CFBG fabricated using a KrF laser and a phase mask. A demodulation technique for the fabricated CFBG sensor is introduced, which allows converting the CFBG spectrum into the temperature measured in each section of the grating, with 1 mm spatial resolution. Next section describes experimental setups to validate the CFBG temperature sensor: first, a linear thermal gradient is induced, and a RF ablation setup to apply Gaussian-shaped temperature profile. In section 5.3 we present results in the form of thermal maps. Section 5.4 summarizes the work and present conclusions.

5.2 Fabrication of mPOF CFBG

Bragg grating structures were formed in the three ring microstructured poly (methyl methacrylate) (PMMA) optical fiber with a uniform distribution of benzyl dimethyl ketal (BDK) in its core [157]. Before the experiments, post heating at 70 °C was performed on a piece of POF (200 mm length) in order to redistribute residual stress during the drawing process. After the post heating, the fiber sample was connected to the ferrule on one end, so it could be connected to a single mode fiber (SMF) through a mating sleeve. Since the diameter of the mPOF is larger than the SMF, the polymer fiber was partially etched at one end-side. Etching was performed in acetone solution (2:1 mixed acetone and liquid alcohol) following the method described in [158]. Then, the mPOF-SMF connector was fixed and stabilized by applying glue, and leaving

the fibers at room temperature to let it dry [158]. Additionally, the end face of the PMMA fiber was polished with sand paper to improve the end face quality. Inscription of the chirped FBG was performed with a coherent KrF excimer laser (pulsed operating mode, 248 nm wavelength, pulse energy 2.5 mJ) (**Figure 5.1**). **Figure 5.2** presents the system for the CFBG inscription: laser beam has a top-hat profile with the size 6.0 × 1.5 mm^2 and divergence equal to 2 × 1 $mrad^2$. A plano-convex cylindrical lens (effective focal length 200.0 mm) was positioned in front of the fiber to focus the UV beam. Inscription of the grating was realized with the help of a 10 mm long uniform phase mask, with 1067.03 period, and 1% strain was applied in order to obtain a chirp profile [159]. The fabricated Bragg grating has a length of 10 mm, in addition the chirped profile is obtained through the strain pattern.

Figure 5.2 shows the reflected amplitude spectra for a 10 mm long CFBG and non-uniform tapering on mPOF. A maximum reflectivity is −34.27 dB, and the full-width half maximum (FWHM) bandwidth is 0.94 nm, which corresponds to a chirp rate approximately 0.09 nm/mm.

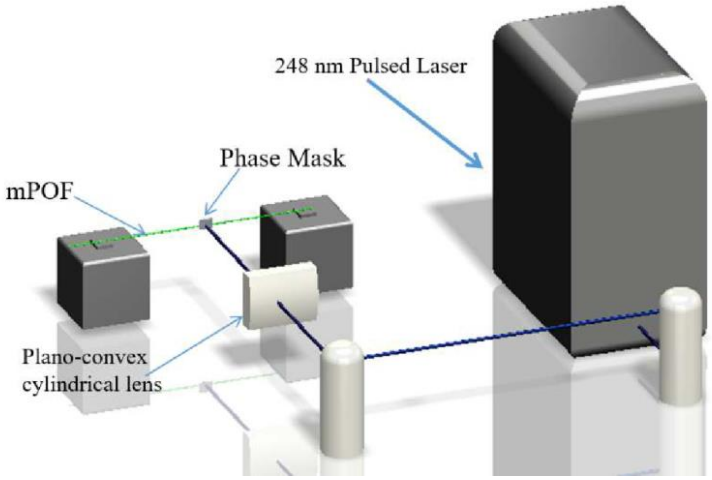

Figure 5.1 Experimental setup for the chirped Bragg grating inscription by means of KrF excimer laser and a uniform phase mask [3].

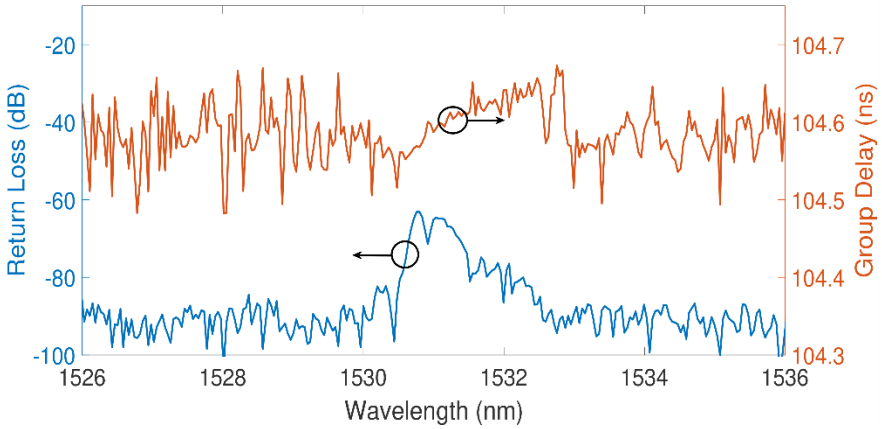

Figure 5.2 Reflection spectrum (left) and group delay (right) of mPOF CFBG in reference condition, before exposure to thermal gradients [3].

5.3 Temperature reconstruction

In order to obtain temperature data, a method of spectral reconstruction was adopted from [3] and adjusted to the CFBG used in this work. In this method, temperature profile is assumed to have a known shape over the length of the CFBG, and it is a function of certain parameters. Grating parameters are defined with the coupled mode theory (CMT) [112]. Then, during each measurement, a detected temperature profile is applied to the CMT model until the root mean square error between the simulated grating and the measured spectrum is minimized. This method was discussed in details in [3] and allows the detection of either a linear temperature profile, or a Gaussian-shaped pattern which is produced by RFA or LA devices. In case of a linear profile ΔT(z), it is a function of 2 parameters:

$$\Delta T(z) = A_0 + A_1 \cdot z \tag{5.1}$$

where z is the axis along the fiber, A_1 is the thermal gradient, and A_0 is the temperature offset. For a thermal ablation pattern, we assume a Gaussian distribution:

$$\Delta T(z) = A \cdot exp\left[-\frac{(z-z_0)^2}{2\sigma^2}\right] \tag{5.2}$$

where A, z_0, and σ are the amplitude, center value, and standard deviation respectively.

The proposed algorithm utilizes the same approach as for the silica CFBG in [3]. Since in this study a CFBG is inscribed into a polymer fiber and has different geometrical and optical parameters, the model was adjusted to meet those characteristics. The major differences of mPOF CFBG are in the value of chirp rate coefficient: ~10 times narrower than for a glass fiber; and thermal sensitivity: ~1 order of magnitude greater and with opposite sign. The solution that we propose is to maintain a relatively high number of simulated gratings (M = 100), which provides an adequate discretization of each element constituting the chirped grating. The parameters of the CFBG grating were estimated from the measured optical spectra and summarized in **Table 5.1**.

Table 5.1 Parameters of the mPOF CFBG

	Wavelength bandwidth	Grating strength, kL_g	Effective refractive index, n_{eff}	Refractive index change, δn_{eff}	Chirp rate	Thermal sensitivity, pm/°C
mPOF CFBG	1529.5 – 1530.7 nm	0.34	1.4895	10^{-5}	0.09 nm/mm	-191.4

Important modification that had to be applied into the proposed algorithm, is to artificially increase the overall length of CFBG to 10 cm, rather than 1 cm as its geometrical size. The reason for this change is that the temperature reconstruction techniques works well for gratings with chirp rate of 1 nm/mm to 2 nm/mm, such as the silica CFBG studied in [3]. Polymer CFBG has a much narrower chirp rate, about 0.09 nm/mm, so, in order to maintain the structure of the algorithm without changing the optimization routine, we artificially expand the grating length by a factor 10 in order to have an artificial chirp rate of 0.94 nm/mm, similar to the previous values reported in [3]. After inputting all the parameters of the CFBG, the algorithm computes the optimization routine and extract the temperature profile over the grating artificial length (100 mm), that is then rescaled down by a factor 10 to the 0–10 mm dimension.

5.4 Thermal profile detection with mPOF CFBG

5.4.1 mPOF CFBG sensor calibration

In this work the calibration of mPOF CFBG sensor was performed in the water bath during water heating. Since the polymer FOS are sensitive to humidity changes, due to water absorption and the resulting swelling of the fiber [160], prior to calibration the CFBG sensor has been placed into the water bath for 12 hours. This step was performed once in order to absorb water and, hence, to exclude humidity measurement during the calibration process. There was no particular investigation of the duration of such an effect and whether the fiber has been dried after a certain period of time. However the calibration in water bath was done 1 h after the fiber had absorbed water, so in this case the shift of the Bragg wavelengths was induced by the temperature increment only.

The sensor was calibrated in the water bath within the temperature range 24.0°C to 37.0 °C, a contact electronic thermometer was used to monitor reference temperature. Reflected spectrum of CFBG was measured with a calibration step of 1 °C; for each measurement the Bragg wavelength has been estimated by calculating the center of the FWHM of the grating.

The reflection spectra of the chirped FBG, measured at different temperatures during calibration test are displayed at **Figure 5.3**; as expected by [155], one observes the blue shift of the spectrum during the heating. Thermal sensitivity of the mPOF CFBG sensor can be estimated as the relationship between the Bragg wavelength shift and a temperature increment (**Figure 5.4**). By applying a linear fit, we calculated the temperature sensitivity of the CFBG sensor as −191.4 pm/°C, which is close to the sensitivity coefficient (−180.0 pm/°C) reported in [161]. This value for the sensitivity coefficient has been applied during spectral reconstruction with the CMT model. Errors during calibration can be attributed to non-uniform heat distribution in the water bath, heat absorption effect, accuracy of the thermometer, and to a non-linear thermal coefficient of the PMMA fiber [162].

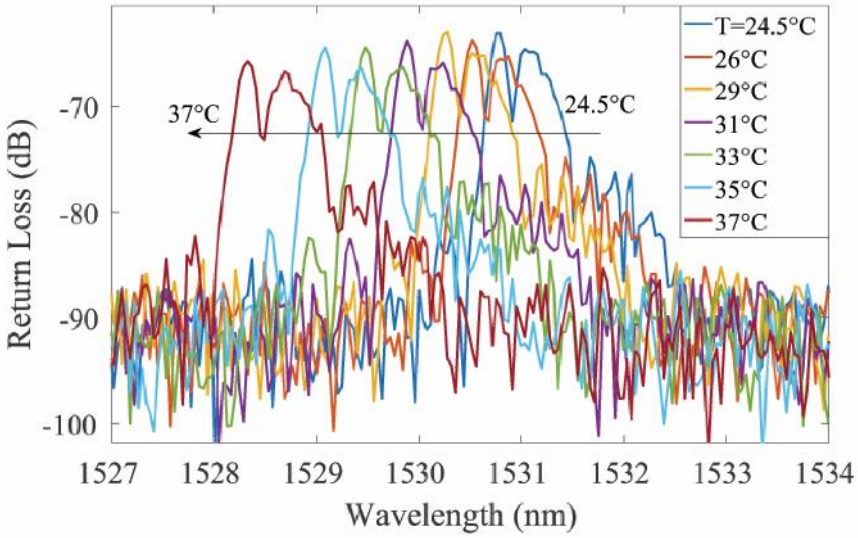

Figure 5.3 Reflection spectrum (left) and group delay (right) of mPOF CFBG during heating cycles in water bath.

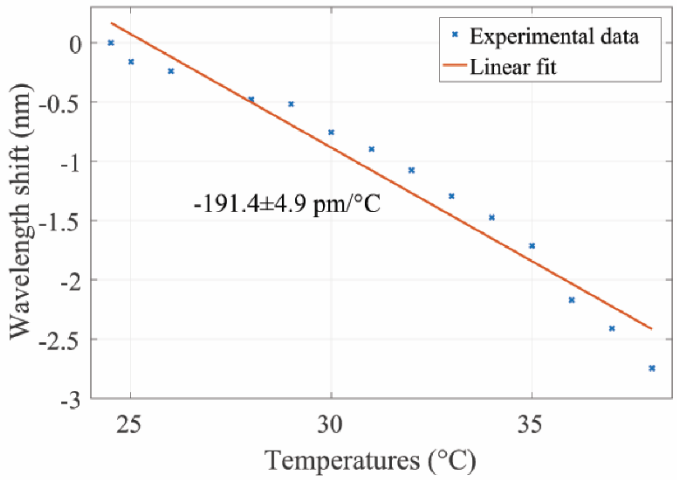

Figure 5.4 mPOF CFBG central wavelength shift as a function of temperature; the chart shows the experimental data and a linear fit.

5.4.2 Detection of the linear temperature gradient

The experimental setup is shown in **Figure 5.5** and it is designed to assess the feasibility of mPOF CFBG to detect a non-uniform, in particular, a linear temperature profile [109].

In order to create a linear temperature gradient, the tip of the CFBG sensor corresponding to the right portion (longest wavelengths) of the spectrum was

positioned in the center of the hot plate, while the tail (shortest wavelengths) was placed at distance 20 mm from the plate. Since the temperature in the center of the hot plate is higher than at another end of the sensor, one can observe an approximately linear thermal gradient along the CFBG length.

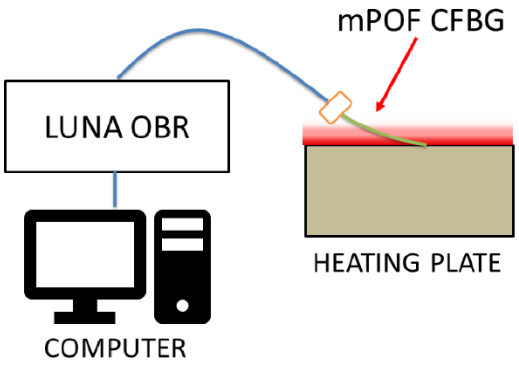

Figure 5.5 Setup for the temperature detection experiment: a case of the linear gradient.

By applying a linear form of the temperature profile to the thermal reconstruction, we obtained a linear pattern along the grating length (**Figure 5.6**). The thermal map reports that as the plate heats, and temperature increases from the tip to the tail of the grating, the gradient progressively enlarges until the hot plate reaches 60 °C; at this time, the tail of the grating is exposed to 49 °C, accounting for a gradient of 11 °C/cm. This experiments shows that the CFBG responds in a different way to a non-uniform pattern, and the spectral reconstruction method can estimate the thermal map.

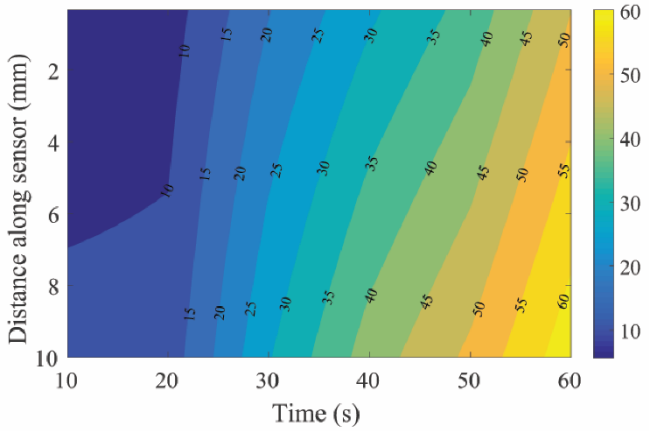

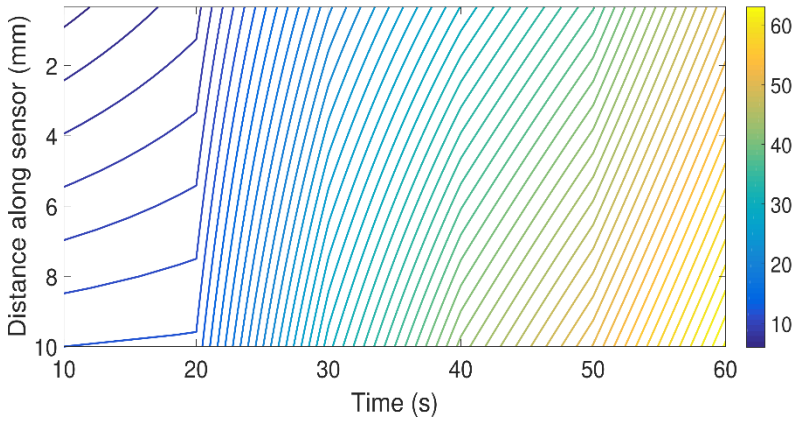

Figure 5.6 Results of the temperature profiling with the mPOF CFBG: upper chart: thermal map, lower chart: isotherms. The colorbar shows temperature in °C degrees.

5.4.3 Temperature measurements during thermal ablation

The sensing performance of the mPOF CFBG was validated during radiofrequency ablation (RFA) on *ex vivo* porcine liver. The use of CFBG inscribed in a polymer fiber provides a much larger sensitivity to temperature variation compared to the silica CFBG (about 19 times higher than was reported in [55]).

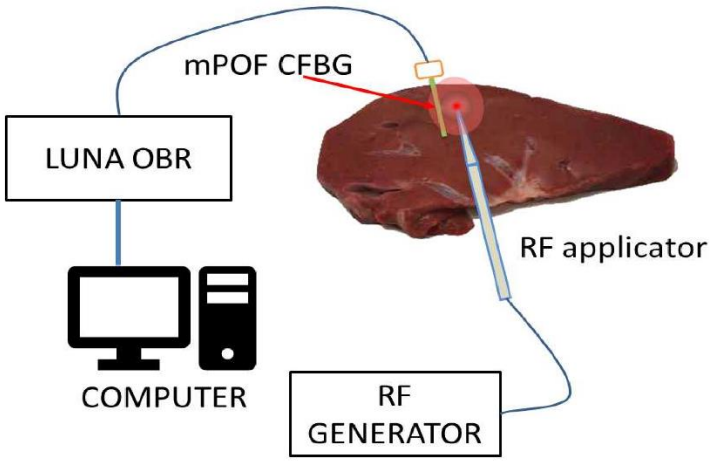

Figure 5.7 Schematic of thermal ablation experiment: the LUNA OBR measures spectra from mPOF CFBG, which is placed in proximity of RF applicator during the ablation.

RF ablation setup is shown in **Figure 5.7.** The mPOF CFBG has been placed in proximity of a RF applicator, which was inserted in the phantom. RF power

was set at 50 W. The reflection spectrum of the mPOF CFBG has been detected by LUNA OBR4600 and further analyzed using the spectral reconstruction technique. The results of thermal reconstruction are shown in **Figures 5.8** and **5.9**. **Figure 5.8** presents thermal map; it can be observed that after 9 s temperature reaches maximum 28 °C, and starts decreasing after 18 s, that correlates with the ablation cycle during experiment. Results agree with the thermal map obtained with the silica CFBG, taking into account the distance 10 mm between the RFA probe and the sensor. The RF power has been automatically disconnected by the RF generator after 18 s, in correspondence to the impedance of the tissue rising over threshold value [55]: this causes the tissue to cool down until reaching room temperature.

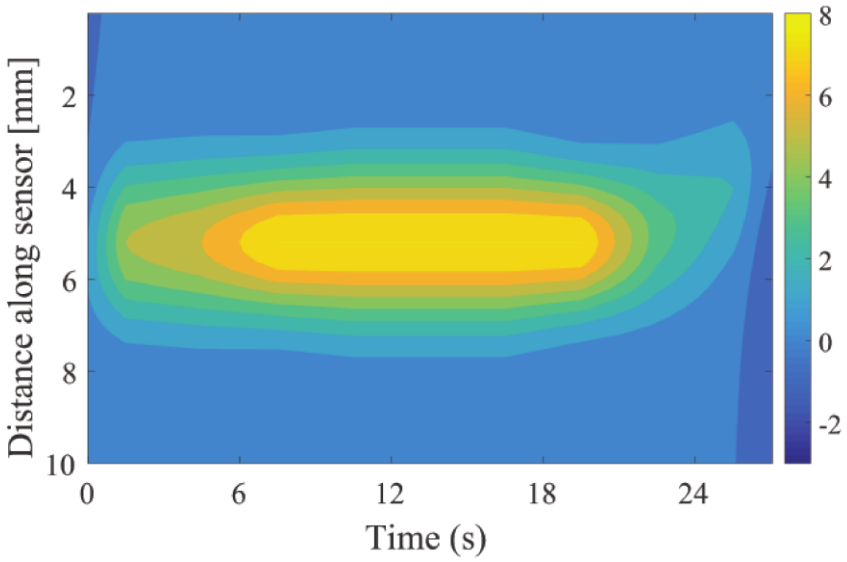

Figure 5.8 Measurement of Gaussian temperature gradient with a mPOF CFBG: thermal profile reconstructed with the CFBG as a function of distance along grating and time during ablation. The colorbar shows temperature in ◦C degrees.

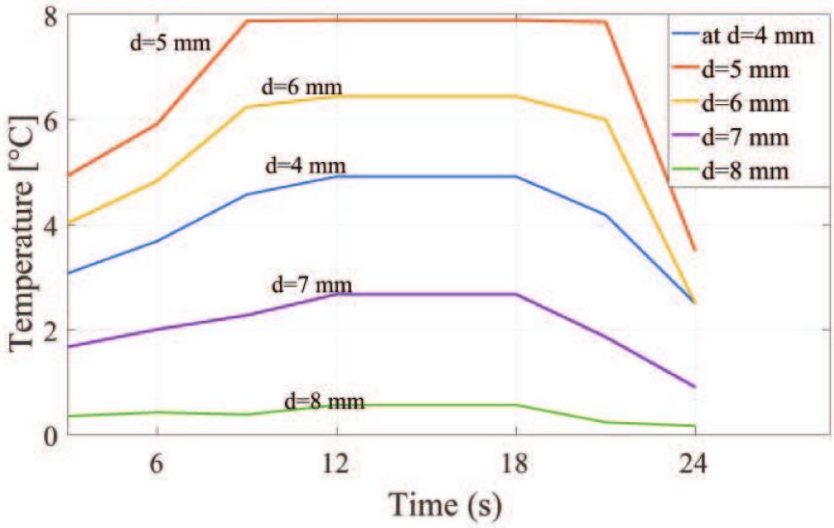

Figure 5.9 Temperature graphs for Gaussian-shaped RFA temperature profile; the chart reports the temperature as a function of time, for different values of position along the grating length *d*.

5.5 Conclusion

In this Chapter, a novel approach for the temperature measurements during thermal ablation by means of a PMMA CFBG was reported. A spectral reconstruction method was developed allowing detection of non-uniform thermal profiles with the mPOF CFBG. Due to the higher thermal sensitivity (−191.4 pm/°C) with respect to glass fiber, and the low chirp rate of the mPOF grating the temperature reconstruction algorithm was modified and validated experimentally. Two sets of experiments were performed: linear temperature profile along 10 mm mPOF CFBG, and a radiofrequency ablation that induces Gaussian shaped temperature gradient. Experiments validate that proposed mPOF CFBG can provide significant advantages for thermal sensing in biomedical applications, however the large sensitivity coefficient impose challenges in positioning the fiber sensor close to the RF applicator tip, where thermal gradient exhibits the steep rate.

Future work will be addressed to evaluate the response of the mPOF CFBG in closer proximity to the applicator, using a longer grating length and possibly a larger chirp rate, and to improve the spectral reconstruction method to work with specific mPOF CFBG coefficients.

CHAPTER 6

Enhanced backscattering optical fiber distributed sensors for temperature monitoring during thermal ablation

Chapter 6 presents results of the two-dimensional thermal mapping of *ex vivo* laser ablation (LA) by means of optical fibers with enhanced backscattering profile. Enhanced scattering properties are achieved through the MgO-based nanoparticles doping of the fiber core. The proposed temperature measurement setup allows detecting multiple sensing regions on a plurality of fibers, which is not possible with a conventional OBR operating on a single optical fiber. Results obtained in the form of thermal maps demonstrate excellent spatial resolution of 2.5 mm.

The Chapter covers fabrication, optical characterization of custom-made MgO nanoparticles-doped optical fibers. Next a methodology of experiment is presented. Results of the temperature measurements during LA are presented in the form of 2D thermal maps, which show improved spatial resolution compared to standard glass fibers. The work presented in this Chapter, was partially published in [59], [60].

6.1 Introduction

6.1.1 Overview of fiber optic distributed sensors

Distributed optical fiber sensors have been developed during the last fourty years [105], [163], and it is a technique for resolved measurements of various physical parameters, such as temperature and strain. The term “distributed sensing” indicates that the measurements are spatially continuous, for ex., along the optical fiber. The first fiber optic distributed sensor was reported in early 80’s and was realized in a liquid-core fiber. That sensor used to measure temperature and interrogation technique was capable to resolve only a few hundred points along 1 m fiber. Since then research efforts have been mostly

concentrated on developing interrogation techniques, utilizing optical time domain reflectometer (OTDR) principles, and capable to provide high resolution measurements.

A significant advantage over other fiber optic sensing techniques is that it requires only a single fiber for both sending and receiving the signal. The unique properties of distributed optical fibers make them the most cost effective and light weight monitoring technique, with a wide range of applications, such as temperature measurements, shape sensing, and stress measurements [164], [165]. Distributed fiber optic sensors have found applications in civil and aerospace industry, demonstrating spatial resolution from one meter to one millimeter, along the distance of up to 100 km [105].

Scattering processes occurring inside the fiber core is the fundamental of any distributed optical fiber sensor. Those scattering phenomena can be described as *elastic* scattering, if no energy is transferred to the medium and, thus, the scattered light has the same frequency as the incident light beam, and *inelastic* scattering, when the emitted light beam is shifted in frequency. In the homogeneous medium, scattering will occur only in the forward direction. In the case of inhomogeneous material, such as silica glass, the variations in density and composition of the medium will result in local fluctuations of charge density and temperature on a microscopic scale [166]. The fiber core dopants, such as GeO_2, as well as anisotropy of molecular orientation, will give rise to local variations in density and refractive index. Such fluctuations of the refractive index cause an elastic scattering process, Rayleigh scattering. **Figure 6.1** illustrates spontaneous Rayleigh scattering phenomenon inside the fiber core: local variations of the refractive index (shown as a freeform shape) act as scattering centers, reflecting some portion of the incident light in all directions. The portion of this scattered Rayleigh light which falls within the angle of acceptance of the fiber will be captured by the waveguide and will be propagating in the backward direction (**Figure 6.1**).

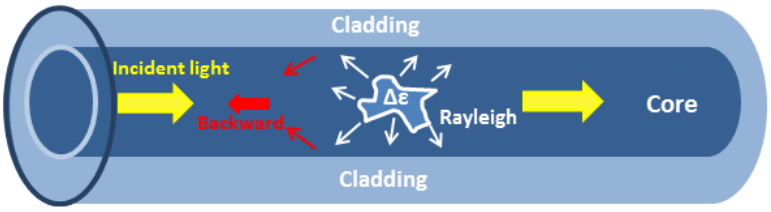

Figure 6.1 Rayleigh scattering mechanism in the core of an optical fiber.

The intensity of that backscattered signal in single-mode fibers is about 10^6 times lower than that of the input light and has a random spectral behavior [167]. Interrogation of such weak signals is a complex task.

Optical frequency-domain reflectometry (OFDR), based on the ideas developed by Froggatt et al. [22], is nowadays one of the most advanced technique of distributing sensing, providing resolution of 1 mm or less.

The fundamental features of any distributed sensor is that all the fiber in its length represents the sensing elements. Another important property, is that because of the material dependent nature of the scattering, every fiber is characterized by its own “signature”, i.e the backscattering profile, which is stable if no conditions change.

The exceptional low spatial resolution has a significant impact in the field of biomedical engineering, and distributed sensors applications for monitoring temperature and shape have been demonstrated [99].

Modern thermal therapy systems lack measurement device capable of providing temperature data in both vertical and horizontal directions, from one side, and having good spatial resolution from another side. In Chapter 3 of the Thesis book we demonstrated apparent advantages of the fiber optic distributed sensors, in particular, application of OBR approach for the monitoring of thermotherapies [99], [108]. The advantages include high spatial resolution, achieving 100 μm, as well as low cost of the sensors, since the single mode (SM) optical fibers serve as sensing element in this case. In order to extend the OBR-based fiber optic sensor system to the planar temperature measurements, which will significantly enhance the real-time control of the thermal ablation procedure, it is necessary to achieve a multifiber, multiplexed operation of the OBR system. However, one should consider the inherent

limitation of the OBR, which allows only a single fiber to be interrogated at a time.

Possible solutions of this issue require either bending a single fiber into a snake shape or a spiral shape, in order to cover a certain 2D area; or introducing a 1 × N optical switch to work with multiple output fibers. Bending a fiber is limited with a bending radius that cannot be smaller than a certain value, otherwise the bend losses will exceed critical values. Using a switch is associated with longer interrogation durations, which leads to slowing down the system since each channel has to be triggered and referenced separately [107].

6.1.2 The concept of enhanced backscattering fibers (EBF)

In this Chapter a new concept is proposed to extend OBR from 1-dimensional to 2-dimensional sensing through simultaneous interrogation of multiple fibers with a single scan. The proposed methodology makes possible to operate an OBR system with more than one optical fibers, thus achieving 2- or 3-dimensional measurements. The main idea is to utilize specialty fibers with enhanced properties instead of a standard single mode glass fiber. Introducing nanoparticles into a fiber core lead to significantly increased scattering level compared to the SMF fiber. Thanks to this property, the Rayleigh scattering component from the nanoparticles-doped fiber is much higher than the total scattering profile of the connecting SMF fibers, so the reflected spectra detected by the OBR will be unambiguously associated to a particular sensing region.

Chapter 6 presents the setup utilizing OBR as interrogation unit, and NP-doped fibers and the set of optical fiber extenders that provides two-dimensional (planar) temperature measurements in thermal ablation.

First, a methodology of MgO-doped fibers fabrication and characterization is overviewed (Section 6.2); then an arrangement of experiment is presented, including the discussion of setup for laser ablation and temperature measurements (Section 6.3). Results are presented in Section 6.4, followed by the conclusions and discussion (Section 6.5).

6.2 NP-doped fibers fabrication and characterization

6.2.1 Fabrication of MgO-doped optical fibers

Specialty optical fibers, used in this work, have been fabricated via fiber-drawing process of the preform. The preform was prepared by a Modifed Chemical Vapor Deposition (MCVD) process, which is a proven and low cost fabrication technique [168].

The doping was performed by immersing the Ge-doped core porous layer into a doping solution injected in the horizontally rotating tube. The doping solution was the ethanol-based solution of $MgCl_2$ and $ErCl_3$ with concentrations of 0.1 mol/L of $MgCl_2$ and 10^{-4} mol/L of $ErCl_3$. After the soaking, solvents were removed from the porous layer by heating at 1000 °C under an oxygen flow. The core layer was subsequently sintered down (at 1800 °C) to a dense glass layer. Finally, the preform was obtained at high temperatures (greater than 2000 °C) by collapsing the tube into a rod. The diameter of the preform was ~10 mm and the core size was 800 µm.

The optical fiber was fabricated through a draw tower process; temperature of 2000 °C was maintained during the process. The resulting diameter of the fiber was 125 µm with the core 10 µm.

An important and remarkable feature of the fabrication process is that a growth of oxide nanoparticles happens *in-situ* in the silica substrate during draw towering. Nanoparticles formation is a result of spontaneous phase separation, meaning that two phases are formed in the preform – one silica rich, another is MgO rich, obtaining forms of nanoparticles. Alkaline-earth elements (Mg, Ca or Sr) act as 'phase-separation' elements and the silicate systems containing such metal oxides exhibit large immiscibility domains. During draw towering, nanoparticles start to elongate taking a shape of cylinders; with a length up to 300 nm [168], [169]. These nanocylinders breaks up into smaller size nanoparticles due to Rayleigh instabilities or until viscous stresses are decreased.

The parameters of nanoparticles, such as diameter, concentration, distribution, as well as particles location – vary and can be controlled throughout the fabrication process. The change in the geometry of the particles strongly influences the performance of the fiber in terms of scattering

and return losses. Table 1 shows some characteristic parameters of two examples of fibers drown with the described technique.

The cross-section of the fibers M01 and G22 fabricated in [168] is presented in **Figure 6.2**. The fibers have a common diameter of a core - 10 μm and a cladding diameter of 125 μm. In the fiber M01 contains nanoparticles with average diameter of 100 um smaller than the particle in the G22 fiber, while the concentration in the M01 is significantly larger that in the G22. Moreover, the distribution of the particle in M01 fiber is uniform while in G22 fiber the particles pattern takes the shape of a ring.

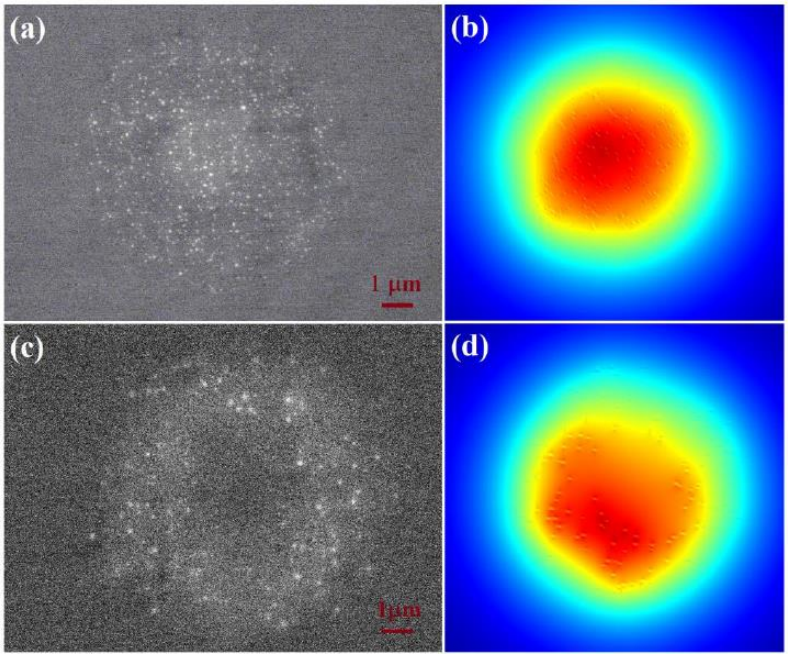

Figure 6.2 SEM cross section of the MgO-doped fibers: (a) M01 fiber, (c) G22 fiber. Simulation of LP01 mode shape of the (b) M01 and (d) G22 fibers. [4]

6.2.2 Characterization of the EBFs.

Due to the phase separation mechanism, nanoparticles exhibit refractive index ranging from 1.53 to 1.65, which is larger than an effective group index of refraction of the SMF-28 fiber (n_{eff} = 1.46) [168]. The presence of the nanoparticles significantly affects the level of scattering; the fibers utilized in this work demonstrate about 36 dB increased scattering level with respect to SMF-28 glass fiber. The return losses are also enhanced and depend strongly on particle sizes and distribution inside the core.

Backscattering profile of the NP-doped fibers spliced with a standard SMF-28 fiber is shown in **Figure 6.3**. Enhanced scattering level of the EBF is obvious with respect to a non-doped glass fiber. EBF shows an amplitude of -73.6 dB, while the scattering level of SMF is about -109 dB, resulting in the scattering "gain" of G = 35.4 dB. Since Rayleigh scattering is a loss factor in the fiber, attenuation of the EBF is also high compared to the SMF, in Figure 6.3 the losses are depicted as the slope of the scattering trace. Scattering gain of the EBFs is the key concept of the fiber multiplexing setup that is described in the following section.

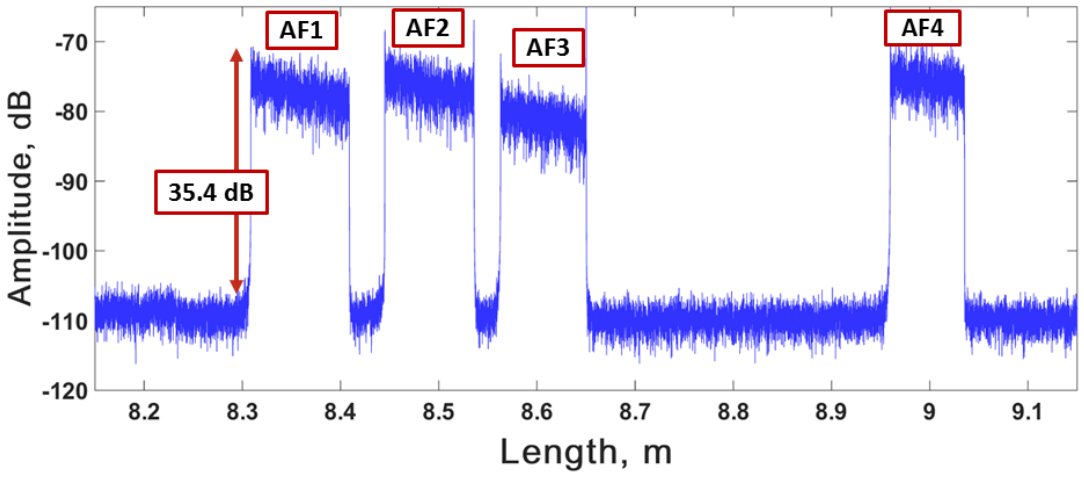

Figure 6.3 Backreflected power of the EBFs, as detected by OBR.

Temperature sensitivity of the as-fabricated MgO-doped fiber was calculated from the relationship between the wavelength shift and temperature change. The fiber was placed on the hot plate that was heated from 40 °C to 130 °C. Such a range is typical for the heating of the tissue during RF ablation. A temperature was recorded with an electronic contact thermometer, and during each measurement a backscattering profile was detected with OBR (OBR4600, Luna Technologies). **Figure 6.4** shows the linear function, from which a sensitivity coefficient was estimated, and is equal to 11.9 pm/°C. The result is close to sensitivity of single mode glass fiber, meaning that the doping process does not significantly affect the thermos-optic coefficient of the fiber.

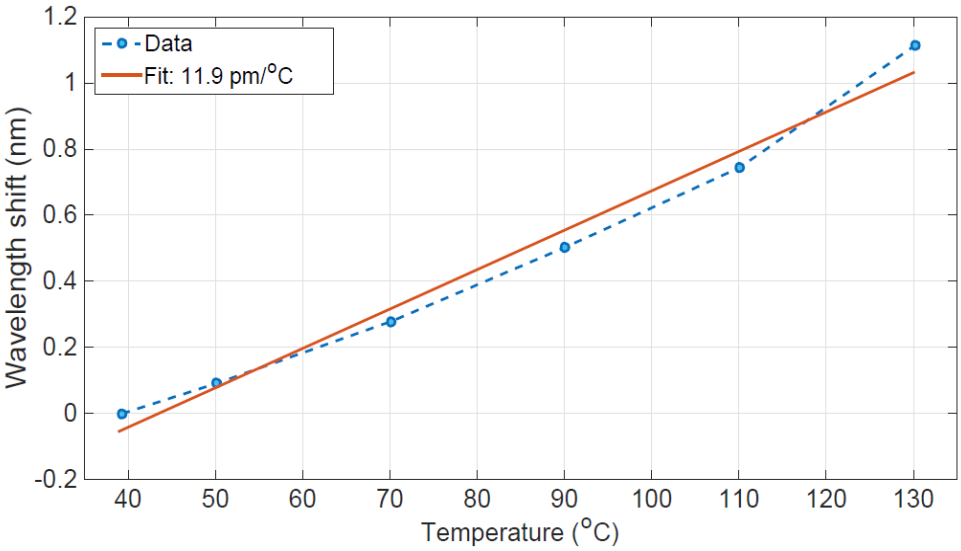

Figure 6.4 Temperature sensitivity of the MgO-doped fiber

6.3 Experimental instrumentation

6.3.1 Design of experiment

A schematic diagram and photographic image of the experimental setup are presented in **Figure 6.5** and **Figure 6.6**, respectively. Experimental setup was designed to perform real time temperature measurement during laser ablation process. Two instrument sets were arranged for this task: a laser ablation device to perform contactless ablation of the porcine liver phantom, and the optical fiber based temperature measurement setup.

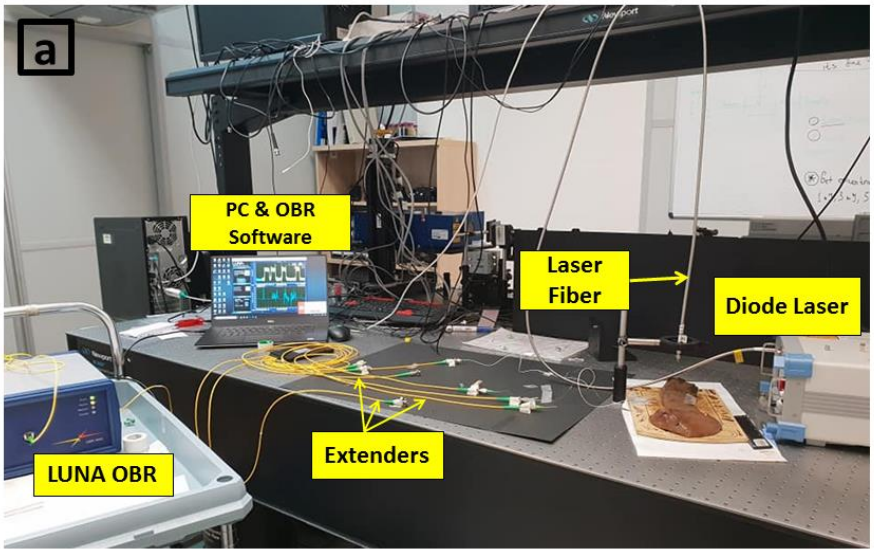

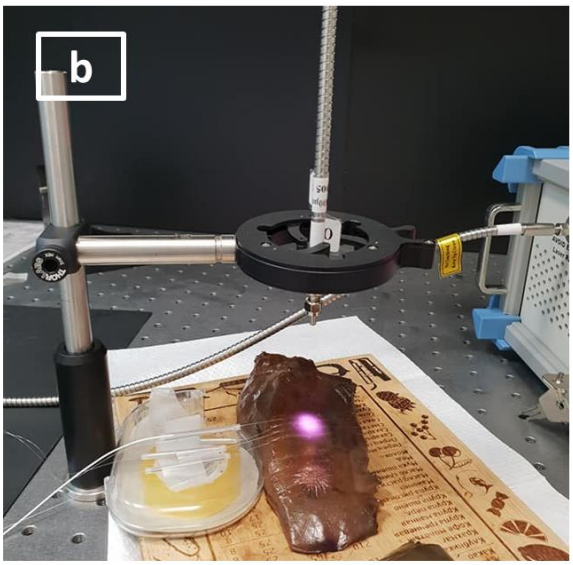

Figure 6.5 Photograph of the laser ablation and EBF based distributed sensing setup. (a) View of the whole setup, including laser diode, and OBR-based fiber multiplexing setup. (b) Positioning of the 4 MgO-doped fibers on the liver phantom; and the laser output fiber fixed perpendicular to the liver surface.

The setup for laser ablation was based on a 980 nm fiber coupled diode laser (RLTMFC, Roithner LaserTechnik, Austria). The diode laser was operating in continuous mode, and the emission power was set at 2-3 W. The output of the laser diode is coupled into a 400 µm optical fiber to deliver light onto the tissue surface in a contactless manner. The laser fiber (NA = 0.22) was fixed perpendicularly to the surface of the phantom, so that the distance from the fiber tip to the phantom was 6 cm from it (**Figure 6.5**b). The laser beam spot diameter was 10 mm, and the ablation duration was 90 s.

LA was performed ex vivo on a cut of porcine liver, purchased in a local slaughter house. Prior to conducting the experiment, it was important to maintain room temperature at 21 °C, to ensure stable operation of the diode laser. After that, P-I characteristics of the laser was measured and is presented in **Figure 6.7**. Before heating the tissue, its initial temperature was measured with contact thermometer (IKA ETS-D5).

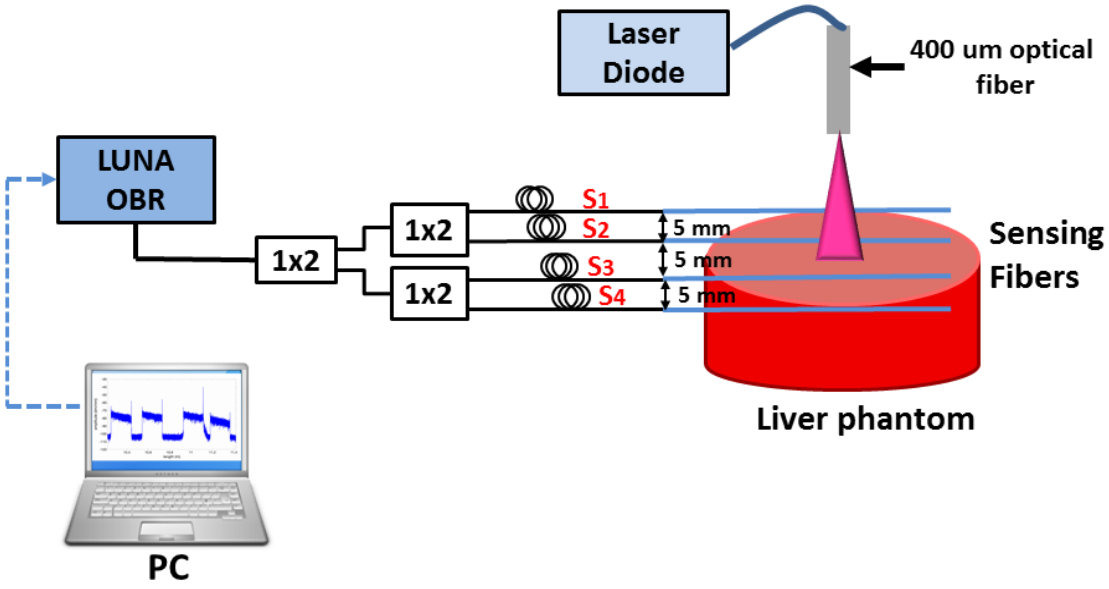

Figure 6.6 Schematics of the laser ablation and EBF based distributed sensing setup. The fiber multiplexing setup consists of 3 splitters, 4 extenders and 4 MgO-doped fibers, positioned in parallel to each other at distance d = 5 mm.

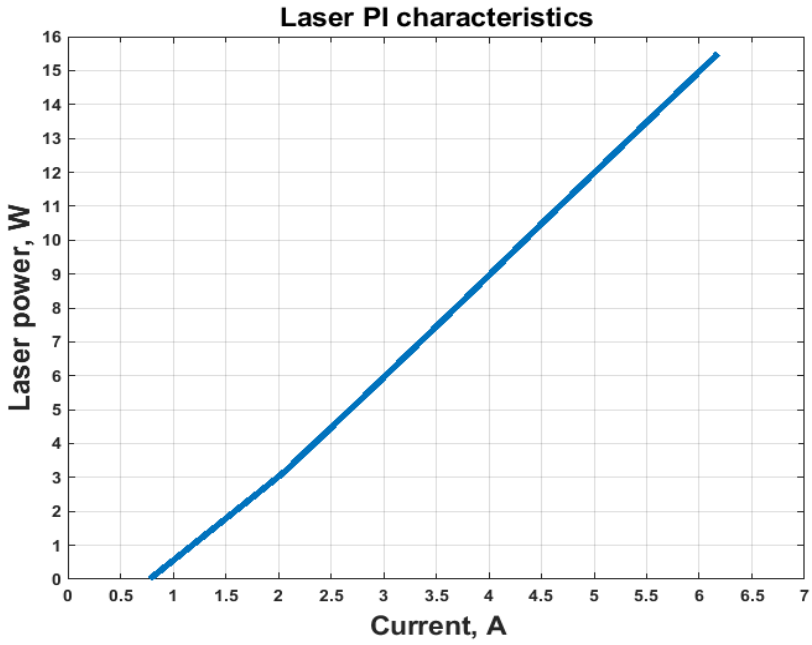

Figure 6.7 P-I characteristics of the 980 nm diode laser.

6.3.2 Temperature sensing and fiber multiplexing

Fiber optic based temperature measurement setup is shown in **Figure 6.6**; the setup consists of the matrix of parallel fibers and commercial OBR (OBR4600, Luna Technologies) to interrogate reflected spectra of the fiber parallel. The fiber parallel, as shown schematically in **Figure 6.6**, is based on 4 extenders S_1, S_2, S_3 and S_4, each having a different length and acting as delay lines of the MgO-doped sensing fibers. Fujikura 12-S fusion splicer was used to splice an extender with a piece of MgO-doped fiber. Four lines of the fibers was arranged in parallel and was connected to the output of Luna OBR by means of three 50/50 wideband splitters.

Interrogation unit is Luna OBR, employing OFDR principle. In this setup, temperature changes are measured by analyzing the backscattering profiles of NP-doped fibers, while SMF serve as connecting elements.

The backscattering spectra is shifted in response to a temperature change, so that it can be determined by comparing the measured spectra with the initial, or reference, trace. In order to observe the backscattering profiles from every MgO-doped fiber, it is necessary to prevent overlapping of the profiles. To solve this issue, the length of each SMF-28 separator S_n must be longer than the previous S_{n-1} by a length ΔS, so that $\Delta S \geq l_{active}$.

Figure 6.9 presents the relative lengths of 4 extenders labeled as S_1, S_2, S_3 and S_4, spliced to sensing fibers, labeled as AF_1, AF_2, AF_3 and AF_4. Corresponding backreflected profile is depicted as well. In this study, the length of active elements was chosen to be about 10 cm, and the lengths of each SMF-28 extender was chosen in such a way, that the scattering components of the sensing fibers do not overlap each other. In this setup the length of each extender fiber were chosen as: S_1 = 831 cm, S_2 = 844 cm, S_3 = 855 cm and S_4 = 895 cm (see **Figure 6.9**). Such sensor positioning gives information about heat propagation not only in the center of ablation zone, but also on the peripheral sides.

In the experiments, the parameters of OBR was set as follows: distributed sensing mode, with spot scan feature, the scanning rate was 0.3 Hz, spatial resolution was set at 2.5 mm, and the total sensing length, including all sensing elements and extenders, was set at 1100 mm. Distributed sensing mode performs continuous measurements of the backscattering traces. OBR

working principle is to detect fiber signature corresponding to the Rayleigh backscattering spectrum in each location of the fiber [107]. For each sensing location, a reference signature is detected at the start of measurements, and then the wavelength shifts are calculated using a mutual correlation algorithm. Temperature variation in each measurement point was estimated using thermo-optic coefficient obtained during calibration process (**Figure 6.4**). [119].

Figure 6.8 shows positioning of fibers during laser ablation: all 4 sensing elements are placed on the surface of the liver phantom, parallel to each other with the distance 5 mm between each fiber. During LA laser beam was focused in the area between two inner fibers. The length of each sensing region, i.e the length of NP-doped fiber, labeled in **Figure 6.8** as AF_1, AF_2, AF_3 and AF_4 is 10 cm.

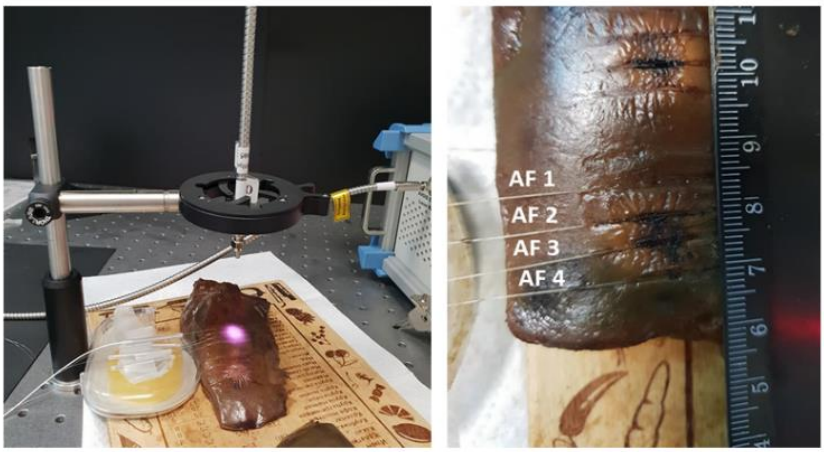

Figure 6.8 View of the laser beam focused on the liver phantom and the positioning of 4 MgO-doped fibers during LA (left); photo of the ablated tissue with 4 fibers in parallel, the distance between fibers is 5 mm.

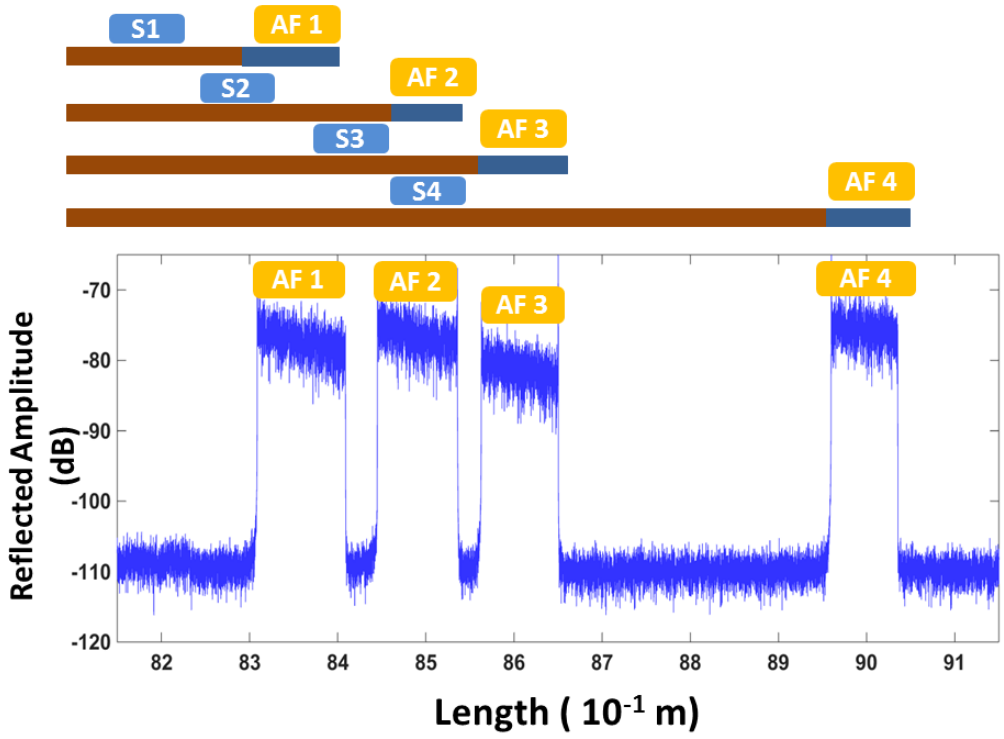

Figure 6.9 Relative lengths of SMF extenders spliced to MgO-doped fibers: S_1 = 831 cm, S_2 = 844 cm, S_3 = 855 cm and S_4 = 895 cm, and the length of each of 4 sensing fibers is 10 cm.

6.4 Results and discussion

Temperature profiles were presented in the form of thermal maps, plotted on the XY plane by processing the data from each sensing fiber. Temperature was sampled with 2.5 mm resolution along the X axis, i.e along the active fiber, and corresponding to the OBR spatial resolution. Spatial resolution in Y direction, perpendicular to the sensing fibers, was 5 mm (corresponding to the distance between adjacent sensing fibers); and time resolution was 0.33 s, corresponding to the OBR speed 3 Hz in single-scan.

Figure 6.10 presents the thermal maps, obtained on the XY plane, and capturing heat distribution patterns at different moments throughout the laser ablation: 20 s, 30 s, 50 s, 70 s, 100 s, and at the end of ablation, i.e. 120 s. For each graph, X-axis corresponds to the direction along the active fiber, and Y-axis corresponds to the direction perpendicular to the sensors. Temperature levels are given by the color bars on the right side; here, not the absolute values, but the temperature increment is displayed. The initial temperature

was measured to be about 21 °C. The considered area is 4 cm x 1.5 cm, corresponding to a grid of 4 x 17 measurement points. Inter-pixel data was interpolated as in [54].

Thermal maps show that the peak temperature is reached in the center of ablation zone, i.e. in the focus area of laser beam then through thermal conduction the heat propagates to the peripheral sides of the ablation area, Such distribution is in accordance with Gaussian shape thermal pattern of LA. Peak temperature value is displayed for the each elapsed time moment. We observe fast heating in the central region of ablation, and the 60 °C threshold is achieved after 30 s of LA.

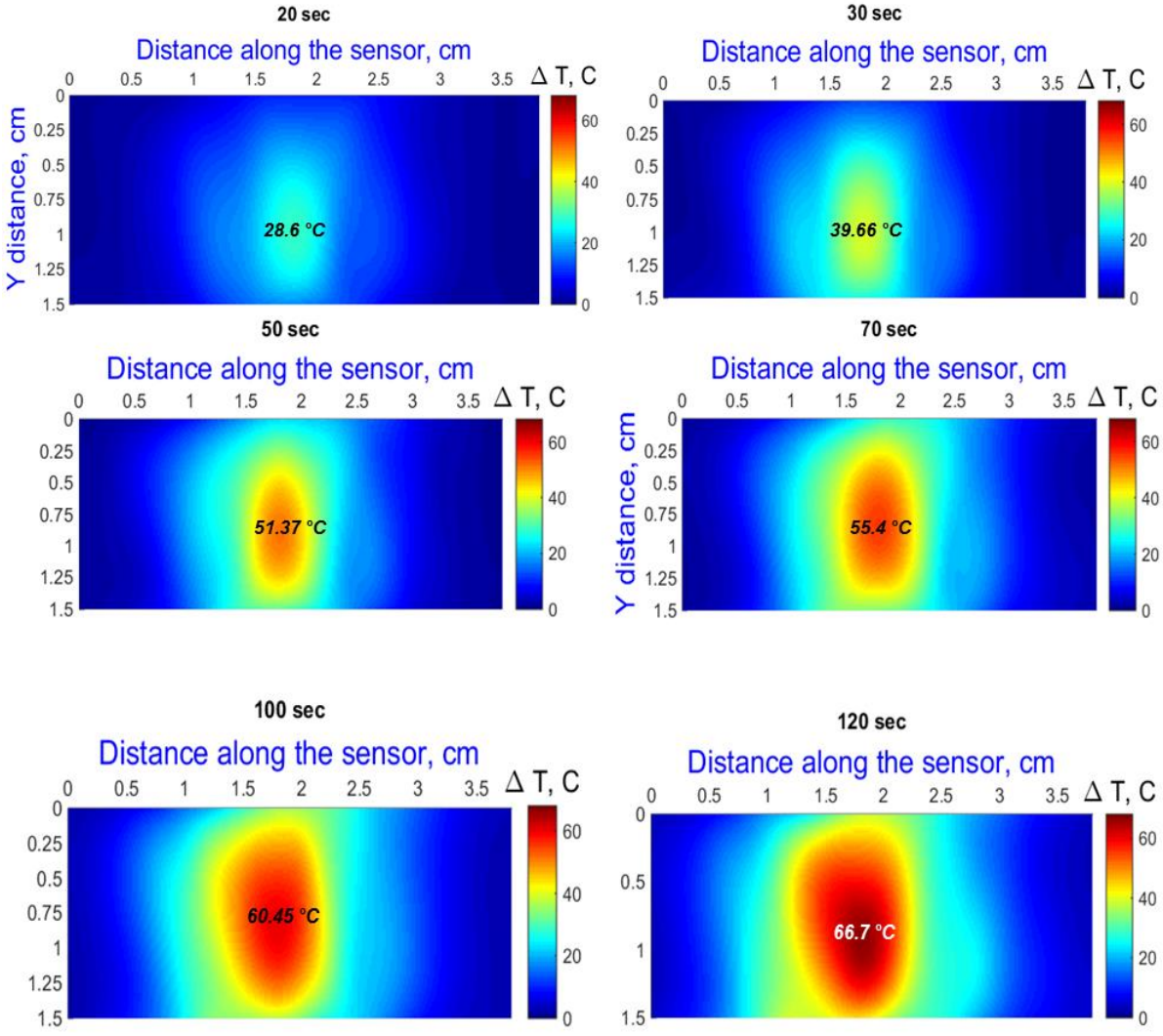

Figure 6.10 Two-dimensional thermal maps reporting temperature on the XY plane for different elapsed time (20 s, 30 s, 50 s, 70 s, 100 s, and 120 s).

6.5 Thermal mapping during Nanoparticle-mediated Laser ablation

The work reported in previous sections of this Chapter was further extended with nanoparticle-mediated laser ablation. The effect of NPs on the temperature distribution during LA was investigated using the above described fiber optic setup, based on the specialty optic fibers with enhanced backscattering profile.

Magnetite nanoparticles were prepared using the methodology described in section 4.2 of Chapter 4. We performed two laser ablations, doing each experiment on a virgin part of the phantom: the first one in absence of nanoparticles, and then after injecting 0.1 mL of NP solutions of 2 mg/mL concentration. The photographic images of the liver tissue after performing two types of ablation, as shown in **Figure 6.11**, demonstrate that adding MNPs solution helps increase the temperature of the tissue. The laser power was set to 3 W, the optical fiber coupled to a laser was positioned vertically, so that the fiber tip is at distance 6 cm from the surface of the phantom. The duration of each experiment was 2 mins.

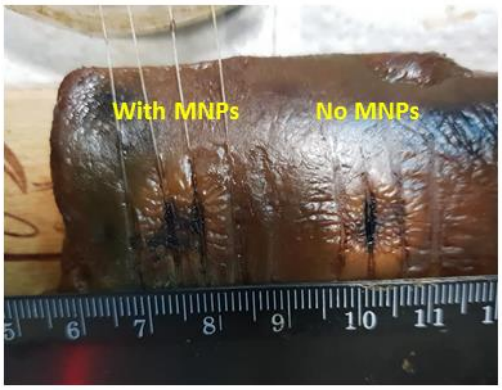

Figure 6.11 Photographic image of the phantom after performing two laser ablations: with and with no MNPs.

Figure 6.12 presents the thermal maps, obtained on the *XY* plane, and capturing temperature profiles at different moments throughout the laser ablation: 30 s, 50 s, 70 s and 100 s. Temperature distributions are presented for two cases: in absence of nanoparticle solution (top row) and for MNP-mediated laser ablation (bottom row). For each graph, X-axis corresponds to the direction along the active fiber, and Y-axis corresponds to the direction

perpendicular to the sensors. Temperature levels are given by the color bars on the right side.

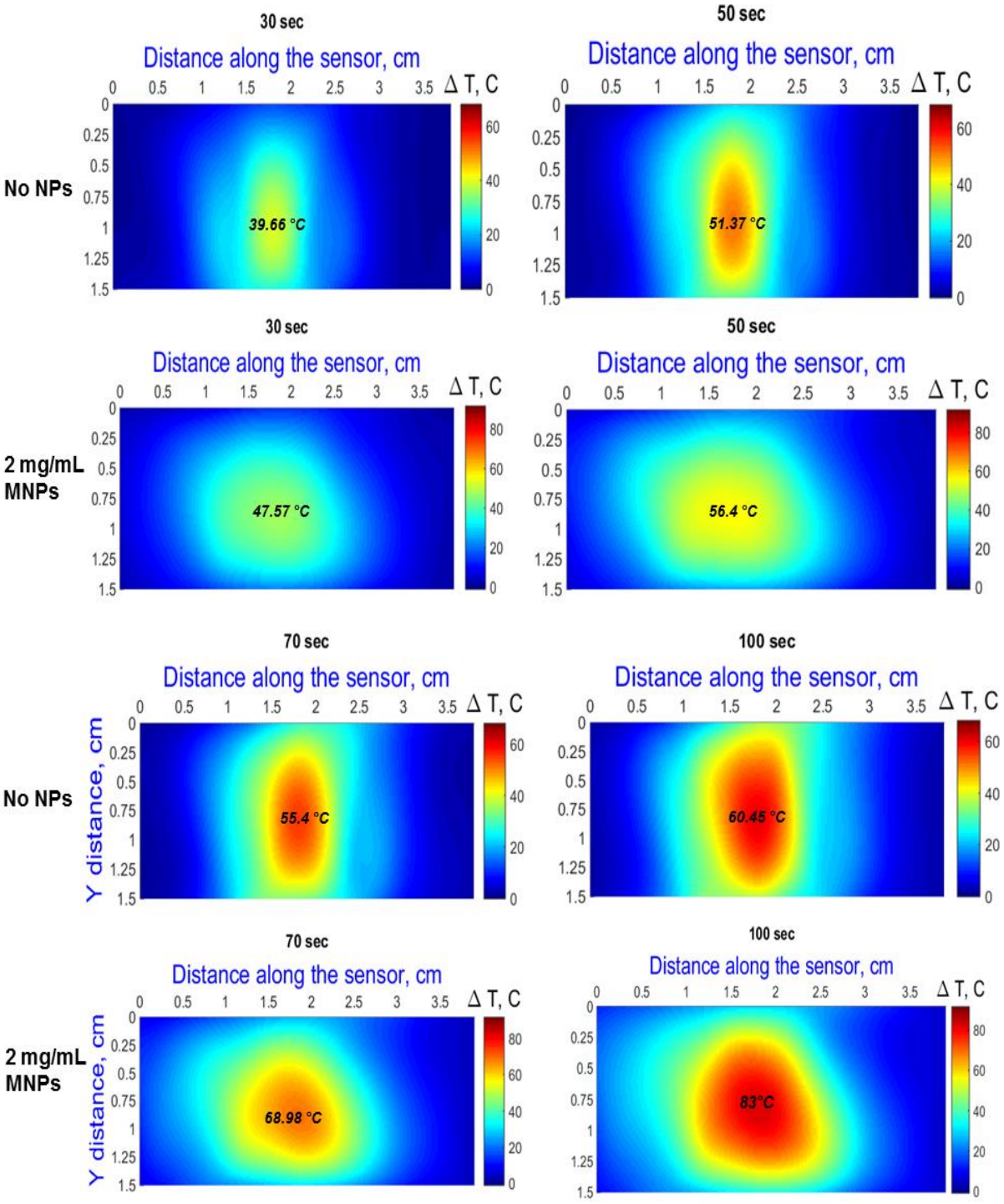

Figure 6.12 Two-dimensional thermal maps, reporting temperature distribution on the XY plane for different elapsed time (30 s, 50 s, 70 s, and 100 s). **Top row** – pristine ablation (no NPs), **bottom row** - with injected MNPs solution. The plain considered is 15×40 mm, with 4 sensing elements spaced 5 mm on Y axis.

The temperature evolution, demonstrated in **Figure 6.12**, gives an idea about the effect of MNPs injection on the thermal propagation during the LA procedure. Analyzing thermal maps obtained for two cases, it can be observed that the peak temperature is reached in the center of ablation zone, then through thermal conduction the heat propagates to the peripheral sides of the ablation area. Moreover, adding the MNPs solution onto the tissue surface helps accelerate tissue heating within the first 30 s of ablation: temperature increment in the central region almost achieves 50 °C and such an isotherm covers significantly larger area compared to the pristine LA. Taking into account the initial tissue temperature, equal to 20 °C, we conclude that the lethal isotherm affects larger volume as well (appearing as yellow-green color on the map).

There is also an extension of the temperature increment on one side of the ablated area, which can be explained by the small amount of nanoparticle solution, that flew out to the side. A similar trend is observed during the whole LA, until the laser is turned off, the injection of MNP solution helps enhance temperature increase and heat propagation towards the edges of ablation zone.

6.6 Conclusion

This chapter reports a novel setup based on MgO doped optical fibers that provides two dimensional temperature monitoring of thermal ablation. The setup utilizes specialty optical fibers with enhanced scattering profile and allows for the OBR/OFDR interrogation of multiple fibers with a single scan. The proposed multiplexing configuration is comprised of 4 fibers having superior amount of backscattering (around 40 dB with respect to SMF), and 4 extenders that implements a network of delayers that provides controlling the positioning of sensing fibers.

The setup has been validated in LA of *ex vivo* liver phantom, and results of temperature measurements are two-dimensional thermal maps with spatial resolution of 2.5 mm. The proposed configuration meet all requirements for the accurate thermometry during thermal ablation.

CHAPTER 7

Conclusion and future perspectives

CONCLUSION AND FUTURE PERSPECTIVES

Interstitial thermal ablative techniques are currently performed in medical practice as a minimally-invasive alternative to traditional surgery in the treatment of benign and malignant tumors.

Thermal ablation demonstrated more favorable outcomes compared to surgical treatment, such as lower mortality rates and shorter recovery period.

Despite growing interest in energy-based modalities their wide use in clinical practice is limited by several factors.

Those limiting factors are related to the lack of accurate real time monitoring of the temperature dose within the target area, from one side, and the inability to treat big size tumors. Since percutaneous thermal ablation is characterized by a steep temperature gradient, the reliable thermometry technique should provide spatial resolution of 1 mm, and temperature accuracy of 1-2 °C.

To date, thermocouples and thermistors attached to RF or MWA antenna are the technologies most used for thermal monitoring. However, in this configuration, such sensors do not provide data on the temperature of the tissue within the whole ablation lesion. The main drawbacks of using thermocouples and thermistors: single point measurements; and measurement errors due to heating of the metallic wires of the thermocouples and thermistors.

Technological development of the image-based thermometry, such as MRI, computer tomography, and US-imaging makes such techniques attractive for the application in thermal ablation. Despite the advantages of the imaging-based modalities, such as 2D thermal mapping of the ablated region, non-invasiveness and sufficient spatial resolution, they are associated with limitations. Those are, for the MRI technology, for example, motion artifacts

caused by natural cardiac activity, and the sensitivity to electromagnetic radiation from the ablation tools.

Fiber optic sensors (FOS) are gaining great attention in the fields of medicine and biology due to their exceptional properties: small size and lightweight, biocompatibility, immunity to electromagnetic interference, high sensitivity to both capability to respond at high speed to both physical and biological parameters, and the possibility to achieve sub-millimeter spatial resolution.

The current generation of FOS embodies another significant advantage over traditional sensing technologies based on electronic sensors: rather than limiting the measurement to a single or few sensing point(s), FOS can employ multiplexed or distributed sensors to spatially resolve physical parameters such as temperature or strain.

In this research study it was proposed to implement fiber optic sensors to improve the outcomes of thermal ablation. The main goal of the thesis was to develop fiber optic based sensing for the multi-point real time temperature monitoring during thermal ablation. To achieve this goal, different fiber optic sensor setups are considered and analyzed, and their performance is studied and compared in terms of spatial resolution and temperature accuracy. Fiber optic sensing modalities that are investigated in this thesis are FBGs, CFBG, CFBG inscribed in polymer fiber, fiber optic distributed sensor interrogated with OBR, and the novel fiber optic multiplexing setup utilizing optical fibers with enhanced backscattering profile.

This work summarizes a comparative study of sensing performance of 3 fiber optic sensing technologies, for the application of RF ablation. Application of each type of sensor is the trade-off between spatial resolution, cost, and interrogation complexity. Using a standard SMF fiber interrogated with OBR provides the highest resolution; up to 0.2 mm of spatial resolution can be achieved with this type of sensor. Such characteristics meet the optimal requirements for the accurate monitoring of thermal ablation procedures, which are 1-2 °C temperature accuracy, 1 reading per second measurement speed, and 1 mm or below of spatial resolution. Despite excellent performance, OFDR is limited by a high cost of interrogation unit, as well as the trade-off between accuracy, spatial resolution, scanning rate, and sensing length. FBG sensors are low cost, however provides much poor spatial

resolution compared to distributed sensor, since it is limited by the size of FBG grating, with a 5 mm FBG it is not possible to achieve the resolution better than 1 cm. CFBG has a sophisticated demodulation procedure, leading to an error in measurements and the overall underestimation of temperature.

In this work an FBG-based sensing setup was implemented for the real-time thermal profiling of RFA and MWA enhanced by 0.1 mL aqueous solution of nanoparticles (Fe_3O_4, Magnetite). Results demonstrated for the first time, that percutaneous TA can be enhanced with nanoparticle solution to treat tumors of larger size with a single applicator. FBG sensors network arranged in a 2D plane, confirmed the favourable impact of MNPs injection mitigating the tissue impedance; obtained thermal maps showed that for MNP-enhanced RF ablation a lethal lesion extended by 60% and in case of MWA lethal isotherm is enlarged by 20%. The results are significant because, to the best of our knowledge, they report the real-time effect of NPs in the most appropriate format. The results suggest that there is an optimum density of NPs that helps maximize the heat distribution to the outer regions of the tumor.

Another type of fiber optic sensor investigated within this work is chirped FBG inscribed into polymer optical fiber. In particular, this thesis reports for the first time temperature monitoring of RF ablation by means of a PMMA CFBG. Detection of non-uniform thermal profiles with the mPOF CFBG was performed with the spectral reconstruction method that was previously developed for the CFBG on SiO_2 fiber. Due to the higher thermal sensitivity (−191.4 pm/°C) with respect to glass fiber, and the low chirp rate of the mPOF grating the temperature reconstruction algorithm was modified and validated experimentally. Two sets of experiments were performed: linear temperature profile along 10 mm mPOF CFBG, and a RF ablation that induces Gaussian shaped temperature gradient. RF ablation was performed on *ex vivo* liver phantom. Experiments validate that proposed mPOF CFBG can provide significant advantages for thermal sensing in biomedical applications, however the large sensitivity coefficient impose challenges in positioning the fiber sensor close to the RF applicator tip, where thermal gradient exhibits the steep rate.

Future work will be addressed to evaluate the response of the mPOF CFBG in closer proximity to the applicator, using a longer grating length and possibly a

larger chirp rate, and to improve the spectral reconstruction method to work with specific mPOF CFBG coefficients.

Finally, the thesis reports a novel setup based on MgO doped optical fibers that provides high resolution two dimensional temperature monitoring of thermal ablation. The setup utilizes specialty optical fibers with enhanced scattering profile and allows for the OBR/OFDR interrogation of multiple fibers with a single scan. The proposed multiplexing configuration is comprised of 4 fibers having superior amount of backscattering (around 40 dB with respect to SMF), and 4 extenders that implements a network of delayers that provides controlling the positioning of sensing fibers.

The setup has been validated in LA of *ex vivo* liver phantom, and results of temperature measurements are two-dimensional thermal maps with spatial resolution of 2.5 mm. The proposed configuration meet all requirements for the accurate thermometry during thermal ablation.

A summary of the main features characterizing each of the fiber optic sensor technology reported in this study is presented in **Table 7.1.**

Table 7.1 Summary of the features of the fiber optic sensors presented in this thesis

Type of Thermal ablation		**Fiber optic sensor technology**	**Main features (spatial, temporal resolution)**
RFA	Pristine	Array of 5 FBGs	Spatial resolution: 10 mm, 0.1 °C temperature accuracy, and temporal resolution 0.1 sec
		CFBG	Spatial resolution: 0.15 mm, 0.1 °C temperature accuracy, and temporal resolution 0.1 sec
		mPOF CFBG	Spatial resolution: 0.15 mm, 0.1 °C temperature accuracy, temporal resolution 1 sec.
		Distributed sensor	Spatial resolution 0.2 mm, Temporal resolution 1 sec, temperature accuracy 0.5 °C
	MNPs-mediated	3 arrays embedding 5 FBGs each	Spatial resolution: 10 mm in X-direction, and 5 mm in Y-direction; 0.1 °C temperature

			accuracy, and temporal resolution 0.1 sec
MWA	Pristine	3 arrays embedding 5 FBGs each	Spatial resolution: 10 mm in X-direction, and 5 mm in Y-direction; 0.1 °C temperature accuracy, and temporal resolution 0.1 sec
	MNPs-mediated	3 arrays embedding 5 FBGs each	Spatial resolution: 10 mm in X-direction, and 5 mm in Y-direction; 0.1 °C temperature accuracy, and temporal resolution 0.1 sec
HIFU		Array of 5 FBGs	Spatial resolution: 10 mm, temporal resolution 0.1 sec
Laser	Pristine	4 NP-doped fibers	Spatial resolution: 2.5 mm in X-direction, and 5 mm in Y-direction; 0.1 °C temperature accuracy, temporal resolution 0.3 sec
	MNPs-mediated	4 NP-doped fibers	Spatial resolution: 2.5 mm in X-direction, and 5 mm in Y-direction; 0.1 °C temperature accuracy, temporal resolution 0.3 sec

Future work will be focused on optimizing the NP-mediated thermal ablation. This study demonstrated favourable effects of the nanoparticles injection in terms of heat propagation and altering the tissue properties. Nevertheless, it is important to investigate the following questions:

- Study an optimum NP density as a function of the RF power at the generator, for different typologies of tissues.
- Investigating other types of nanoparticles and nanomaterials, that have higher thermal and electrical conductivity than the biological tissue;
- Studying the physics of NP-mediated ablation, such as tissue properties, conductivity of nanoparticles, and correlation with the heat distribution.

In terms of specialty fibers with enhanced scattering profiles future research will be focusing on extending 2-dimensional thermal profiling to 3-dimensional by means of non-standard fibers with high-scattering properties.

REFERENCES

[1] K. F. Chu and D. E. Dupuy, “Thermal ablation of tumours: biological mechanisms and advances in therapy,” *Nat. Rev. Cancer*, vol. 14, no. 3, p. 199, 2014.

[2] T. J. Dubinsky, C. Cuevas, M. K. Dighe, O. Kolokythas, and J. H. Hwang, “High-intensity focused ultrasound: current potential and oncologic applications,” *Am. J. Roentgenol.*, vol. 190, no. 1, pp. 191–199, 2008.

[3] S. Korganbayev *et al.*, “Detection of thermal gradients through fiber-optic Chirped Fiber Bragg Grating (CFBG): Medical thermal ablation scenario,” *Opt. Fiber Technol.*, vol. 41, no. December 2017, pp. 48–55, 2018, doi: 10.1016/j.yofte.2017.12.017.

[4] C. Molardi, W. Blanc, and D. Tosi, “Simultaneous OFDR spatial multiplexing by means of nanoparticle doped optical fibers, theory and sensing applications,” in *Fiber Lasers and Glass Photonics: Materials through Applications II*, 2020, vol. 11357, p. 1135718.

[5] B. Greenway, “Hepatic metastases from colorectal cancer: resection or not,” *Br. J. Surg.*, vol. 75, no. 6, pp. 513–519, 1988.

[6] S. A. Curley Jr, J. C. Cusack Jr, K. K. Tanabe, and L. M. Ellis, “Advances in the treatment of liver tumors,” *Curr. Probl. Surg.*, vol. 39, no. 5, pp. 461–571, 2002.

[7] C. J. Simon and D. E. Dupuy, “Percutaneous minimally invasive therapies in the treatment of bone tumors: thermal ablation,” in *Seminars in musculoskeletal radiology*, 2006, vol. 10, no. 02, pp. 137–144.

[8] D. Liu and C. L. Brace, “CT imaging during microwave ablation: analysis of spatial and temporal tissue contraction,” *Med. Phys.*, vol. 41, no. 11, p. 113303, 2014.

[9] P. L. Pereira *et al.*, “Radiofrequency ablation: in vivo comparison of four commercially available devices in pig livers,” *Radiology*, vol. 232, no. 2, pp. 482–490, 2004.

[10] C. L. Brace, “Radiofrequency and microwave ablation of the liver, lung, kidney, and bone: what are the differences?,” *Curr. Probl. Diagn. Radiol.*, vol. 38, no. 3, pp. 135–143, 2009.

[11] F. J. Wolf, D. J. Grand, J. T. Machan, T. A. DiPetrillo, W. W. Mayo-Smith, and D. E. Dupuy, “Microwave ablation of lung malignancies: effectiveness, CT findings, and safety in 50 patients,” *Radiology*, vol. 247, no. 3, pp. 871–879, 2008.

[12] A. C. Schmitz, D. Gianfelice, B. L. Daniel, W. P. T. M. Mali, and M. Van den

Bosch, “Image-guided focused ultrasound ablation of breast cancer: current status, challenges, and future directions,” *Eur. Radiol.*, vol. 18, no. 7, pp. 1431–1441, 2008.

[13] L. G. Merckel *et al.*, “First clinical experience with a dedicated MRI-guided high-intensity focused ultrasound system for breast cancer ablation,” *Eur. Radiol.*, vol. 26, no. 11, pp. 4037–4046, 2016.

[14] T. Livraghi *et al.*, “Sustained complete response and complications rates after radiofrequency ablation of very early hepatocellular carcinoma in cirrhosis: is resection still the treatment of choice?,” *Hepatology*, vol. 47, no. 1, pp. 82–89, 2008.

[15] P. L. Pereira, “Actual role of radiofrequency ablation of liver metastases,” *Eur. Radiol.*, vol. 17, no. 8, pp. 2062–2070, 2007.

[16] M. Nikfarjam, V. Muralidharan, and C. Christophi, “Mechanisms of focal heat destruction of liver tumors,” *J. Surg. Res.*, vol. 127, no. 2, pp. 208–223, 2005.

[17] L. Frich, “Non-invasive thermometry for monitoring hepatic radiofrequency ablation,” *Minim. Invasive Ther. Allied Technol.*, vol. 15, no. 1, pp. 18–25, 2006.

[18] M. Ahmed, C. L. Brace, F. T. Lee, and S. N. Goldberg, “Principles of and Advances in Percutaneous Ablation,” *Radiology*, vol. 258, no. 2, pp. 351–369, Feb. 2011, doi: 10.1148/radiol.10081634.

[19] T. Seki and K. Inoue, “Microwave coagulation therapy of hepatocellular carcinoma,” *Nihon Naika Gakkai Zasshi.*, vol. 84, no. 12, pp. 2024–2027, 1995, doi: 10.2169/naika.84.2024.

[20] Y. Liu, Y. Zheng, S. Li, B. Li, Y. Zhang, and Y. Yuan, “Percutaneous microwave ablation of larger hepatocellular carcinoma,” *Clin. Radiol.*, vol. 68, no. 1, pp. 21–26, 2013.

[21] E. Maloney and J. H. Hwang, “Emerging HIFU applications in cancer therapy,” *Int. J. Hyperth.*, vol. 31, no. 3, pp. 302–309, 2015.

[22] E. R. Cordeiro, X. Cathelineau, S. Thüroff, M. Marberger, S. Crouzet, and J. J. de la Rosette, “High-intensity focused ultrasound (HIFU) for definitive treatment of prostate cancer,” *BJU Int.*, vol. 110, no. 9, pp. 1228–1242, 2012.

[23] R. J. Stafford, D. Fuentes, A. A. Elliott, J. S. Weinberg, and K. Ahrar, “Laser-induced thermal therapy for tumor ablation,” *Crit. Rev. Biomed. Eng.*, vol. 38, no. 1, 2010.

[24] E. Schena *et al.*, “Experimental assessment of CT-based thermometry during laser ablation of porcine pancreas,” *Phys. Med. Biol.*, vol. 58, no. 16, p. 5705, 2013.

[25] M. Lara-Velazquez *et al.*, “Advances in brain tumor surgery for glioblastoma in adults,” *Brain Sci.*, vol. 7, no. 12, p. 166, 2017.

[26] J. A. Schwartz *et al.*, “Feasibility study of particle-assisted laser ablation of brain tumors in orthotopic canine model,” *Cancer Res.*, vol. 69, no. 4, pp. 1659–1667, 2009.

[27] S. A. Sapareto and W. C. Dewey, “Thermal dose determination in cancer therapy,” *Int. J. Radiat. Oncol. Biol. Phys.*, vol. 10, no. 6, pp. 787–800, 1984.

[28] W. C. Dewey, “Arrhenius relationships from the molecule and cell to the clinic,” *Int. J. Hyperth.*, vol. 25, no. 1, pp. 3–20, 2009.

[29] E. J. Hall and L. Roizin-Towle, “Biological effects of heat,” *Cancer Res.*, vol. 44, no. 10 Supplement, pp. 4708s-4713s, 1984.

[30] M. W. Dewhirst, B. L. Viglianti, M. Lora-Michiels, M. Hanson, and P. J. Hoopes, “Basic principles of thermal dosimetry and thermal thresholds for tissue damage from hyperthermia,” *Int. J. Hyperth.*, vol. 19, no. 3, pp. 267–294, 2003.

[31] S. Puccini, N. Bär, M. Bublat, T. Kahn, and H. Busse, “Simulations of thermal tissue coagulation and their value for the planning and monitoring of laser-induced interstitial thermotherapy (LITT),” *Magn. Reson. Med. An Off. J. Int. Soc. Magn. Reson. Med.*, vol. 49, no. 2, pp. 351–362, 2003.

[32] H. Rhim *et al.*, “Essential techniques for successful radio-frequency thermal ablation of malignant hepatic tumors,” *Radiographics*, vol. 21, no. suppl_1, pp. S17–S35, 2001.

[33] C. Brace, “Thermal tumor ablation in clinical use,” *IEEE Pulse*, vol. 2, no. 5, pp. 28–38, 2011.

[34] B. E. Billard, K. Hynynen, and R. B. Roemer, “Effects of physical parameters on high temperature ultrasound hyperthermia,” *Ultrasound Med. Biol.*, vol. 16, no. 4, pp. 409–420, 1990.

[35] C. W. Song, “Physiological factors in hyperthermia,” *Natl Cancer Inst Monogr*, vol. 61, pp. 169–176, 1982.

[36] O. Seror *et al.*, “Real time monitoring of radiofrequency ablation based on MR thermometry and thermal dose in the pig liver in vivo,” *Eur. Radiol.*, vol. 18, no. 2, pp. 408–416, 2008.

[37] L. Winter *et al.*, “Magnetic resonance thermometry: methodology, pitfalls and practical solutions,” *Int. J. Hyperth.*, vol. 32, no. 1, pp. 63–75, 2016.

[38] M. A. Lewis, R. M. Staruch, and R. Chopra, “Thermometry and ablation monitoring with ultrasound,” *Int. J. Hyperth.*, vol. 31, no. 2, pp. 163–181, 2015.

[39] K. W. A. van Dongen and M. D. Verweij, “A feasibility study for non-invasive thermometry using non-linear ultrasound,” *Int. J. Hyperth.*, vol. 27, no. 6, pp.

612–624, 2011.

[40] G. D. Pandeya, M. J. W. Greuter, K. P. de Jong, B. Schmidt, T. Flohr, and M. Oudkerk, “Feasibility of noninvasive temperature assessment during radiofrequency liver ablation on computed tomography,” *J. Comput. Assist. Tomogr.*, vol. 35, no. 3, pp. 356–360, 2011.

[41] P. Bruners *et al.*, “CT-based temperature monitoring during hepatic RF ablation: Feasibility in an animal model,” *Int. J. Hyperth.*, vol. 28, no. 1, pp. 55–61, 2012.

[42] E. Schena *et al.*, “Monitoring of temperature increase and tissue vaporization during laser interstitial thermotherapy of ex vivo swine liver by computed tomography,” in *2013 35th Annual International Conference of the IEEE Engineering in Medicine and Biology Society (EMBC)*, 2013, pp. 378–381.

[43] G. D. Pandeya *et al.*, “Feasibility of computed tomography based thermometry during interstitial laser heating in bovine liver,” *Eur. Radiol.*, vol. 21, no. 8, pp. 1733–1738, 2011.

[44] J. Paul, T. J. Vogl, and A. Chacko, “Dual energy computed tomography thermometry during hepatic microwave ablation in an ex-vivo porcine model,” *Phys. Medica*, vol. 31, no. 7, pp. 683–691, 2015.

[45] V. Lopresto *et al.*, “CT-based investigation of the contraction of ex vivo tissue undergoing microwave thermal ablation,” *Phys. Med. Biol.*, vol. 63, no. 5, p. 55019, 2018.

[46] N. Weiss, S. N. Goldberg, J. Sosna, and H. Azhari, “Temperature–density hysteresis in X-ray CT during HIFU thermal ablation: Heating and cooling phantom study,” *Int. J. Hyperth.*, vol. 30, no. 1, pp. 27–35, 2014.

[47] C. L. Brace, J. L. Hinshaw, P. F. Laeseke, L. A. Sampson, and F. T. Lee Jr, “Pulmonary thermal ablation: comparison of radiofrequency and microwave devices by using gross pathologic and CT findings in a swine model,” *Radiology*, vol. 251, no. 3, pp. 705–711, 2009.

[48] Y.-J. Rao, D. J. Webb, D. A. Jackson, L. Zhang, and I. Bennion, “In-fiber Bragg-grating temperature sensor system for medical applications,” *J. Light. Technol.*, vol. 15, no. 5, pp. 779–785, 1997.

[49] O. S. Wolfbeis, “Fiber-optic chemical sensors and biosensors,” *Anal. Chem.*, vol. 80, no. 12, pp. 4269–4283, 2008.

[50] C. Cavaiola *et al.*, “Error of a temperature probe for cancer ablation monitoring caused by respiratory movements: Ex vivo and in vivo analysis,” *IEEE Sens. J.*, vol. 16, no. 15, pp. 5934–5941, 2016.

[51] J. Witt *et al.*, “Medical textiles with embedded fiber optic sensors for monitoring

of respiratory movement," *IEEE Sens. J.*, vol. 12, no. 1, pp. 246–254, 2012.

[52] E. Schena *et al.*, "Solutions for improving the outcomes of thermal treatments in oncology: Multi-point temperature monitoring," in *SENSORS, 2017 IEEE*, 2017, pp. 1–3.

[53] P. Saccomandi *et al.*, "Temperature monitoring during microwave ablation in ex vivo porcine livers," *Eur. J. Surg. Oncol.*, vol. 41, no. 12, pp. 1699–1705, 2015.

[54] G. Palumbo *et al.*, "Temperature profile of< italic< ex-vivo</italic< organs during radio frequency thermal ablation by fiber Bragg gratings," *J. Biomed. Opt.*, vol. 21, no. 11, p. 117003, 2016.

[55] D. Tosi *et al.*, "Fiber-optic chirped FBG for distributed thermal monitoring of ex-vivo radiofrequency ablation of liver," *Biomed. Opt. Express*, vol. 5, no. 6, pp. 1799–1811, 2014.

[56] M. Jelbuldina, S. Korganbayev, Z. Seidagaliyeva, S. Sovetov, T. Tuganbekov, and D. Tosi, "Fiber Bragg Grating Sensor for Temperature Monitoring During HIFU Ablation of Ex Vivo Breast Fibroadenoma," *IEEE Sensors Lett.*, vol. 3, no. 8, pp. 1–4, 2019.

[57] M. Jelbuldina, A. Korobeinyk, S. Korganbayev, D. Tosi, K. Dukenbayev, and V. J. Inglezakis, "Real-time temperature monitoring in liver during magnetite nanoparticle-enhanced microwave ablation with fiber bragg grating sensors: ex vivo analysis," *IEEE Sens. J.*, vol. 18, no. 19, pp. 8005–8011, 2018.

[58] M. Jelbuldina, A. V Korobeinyk, S. Korganbayev, V. J. Inglezakis, and D. Tosi, "Fiber Bragg grating based temperature profiling in ferromagnetic nanoparticles-enhanced radiofrequency ablation," *Opt. Fiber Technol.*, vol. 43, pp. 145–152, 2018.

[59] A. Beisenova *et al.*, "Multi-fiber distributed thermal profiling of minimally invasive thermal ablation with scattering-level multiplexing in MgO-doped fibers," *Biomed. Opt. Express*, vol. 10, no. 3, pp. 1282–1296, 2019.

[60] M. Jelbuldina *et al.*, "Multi-fiber distributed temperature profiling in ex vivo magnetite nanoparticle-mediated laser tissue ablation," in *Optical Interactions with Tissue and Cells XXXI*, 2020, vol. 11238, p. 112380H.

[61] R. O. Illing *et al.*, "The safety and feasibility of extracorporeal high-intensity focused ultrasound (HIFU) for the treatment of liver and kidney tumours in a Western population," *Br. J. Cancer*, vol. 93, no. 8, pp. 890–895, 2005.

[62] R. D. Issels, "Hyperthermia adds to chemotherapy," *Eur. J. Cancer*, vol. 44, no. 17, pp. 2546–2554, 2008.

[63] L. H. Lindner and R. D. Issels, "Hyperthermia in soft tissue sarcoma," *Curr.*

Treat. Options Oncol., vol. 12, no. 1, pp. 12–20, 2011.

[64] E. Paulet *et al.*, “Factors limiting complete tumor ablation by radiofrequency ablation,” *Cardiovasc. Intervent. Radiol.*, vol. 31, no. 1, pp. 107–115, 2008.

[65] J. R. Lepock, H. E. Frey, and K. P. Ritchie, “Protein denaturation in intact hepatocytes and isolated cellular organelles during heat shock,” *J. Cell Biol.*, vol. 122, no. 6, pp. 1267–1276, 1993.

[66] H. H. Kampinga, “Cell biological effects of hyperthermia alone or combined with radiation or drugs: a short introduction to newcomers in the field,” *Int. J. Hyperth.*, vol. 22, no. 3, pp. 191–196, 2006.

[67] T. Mala, “Cryoablation of liver tumours–a review of mechanisms, techniques and clinical outcome,” *Minim. Invasive Ther. Allied Technol.*, vol. 15, no. 1, pp. 9–17, 2006.

[68] R. Lencioni *et al.*, “Early-stage hepatocellular carcinoma in patients with cirrhosis: long-term results of percutaneous image-guided radiofrequency ablation,” *Radiology*, vol. 234, no. 3, pp. 961–967, 2005.

[69] J. P. Guenette and D. E. Dupuy, “Radiofrequency ablation of colorectal hepatic metastases,” *J. Surg. Oncol.*, vol. 102, no. 8, pp. 978–987, 2010.

[70] J. P. McGahan and G. D. Dodd III, “Radiofrequency ablation of the liver: current status,” *Am. J. Roentgenol.*, vol. 176, no. 1, pp. 3–16, 2001.

[71] S. N. Goldberg and G. S. Gazelle, “Radiofrequency tissue ablation: physical principles and techniques for increasing coagulation necrosis.,” *Hepatogastroenterology.*, vol. 48, no. 38, p. 359, 2001.

[72] A. S. Wright, L. A. Sampson, T. F. Warner, D. M. Mahvi, and J. Lee Fred T, “Radiofrequency versus microwave ablation in a hepatic porcine model,” *Radiology*, vol. 236, no. 1, pp. 132–139, 2005.

[73] D. F. Saldanha *et al.*, “Current tumor ablation technologies: basic science and device review,” in *Seminars in interventional radiology*, 2010, vol. 27, no. 3, p. 247.

[74] S. Seki *et al.*, “Laparoscopic microwave coagulation therapy for hepatocellular carcinoma,” *Endoscopy*, vol. 32, no. 08, pp. 591–597, 2000.

[75] K. Ohmoto *et al.*, “Percutaneous microwave coagulation therapy for unresectable hepatocellular carcinoma.,” *Hepatogastroenterology.*, vol. 46, no. 29, pp. 2894–2900, 1999.

[76] M. G. Lubner, C. L. Brace, J. L. Hinshaw, and F. T. Lee Jr, “Microwave tumor ablation: mechanism of action, clinical results, and devices,” *J. Vasc. Interv. Radiol.*, vol. 21, no. 8, pp. S192–S203, 2010.

[77] A. S. Wright, F. T. Lee, and D. M. Mahvi, “Hepatic microwave ablation with

multiple antennae results in synergistically larger zones of coagulation necrosis," *Ann. Surg. Oncol.*, vol. 10, no. 3, pp. 275–283, 2003.

[78] A. M. Ierardi *et al.*, "A new system of microwave ablation at 2450 MHz: preliminary experience," *Updates Surg.*, vol. 67, no. 1, pp. 39–45, 2015.

[79] A. M. Ierardi *et al.*, "Microwave ablation of liver metastases to overcome the limitations of radiofrequency ablation," *Radiol. Med.*, vol. 118, no. 6, pp. 949–961, 2013.

[80] L. J. Higgins and K. Hong, "Renal ablation techniques: state of the art," *Am. J. Roentgenol.*, vol. 205, no. 4, pp. 735–741, 2015.

[81] S. J. E. Rombouts *et al.*, "Systematic review of innovative ablative therapies for the treatment of locally advanced pancreatic cancer," *Br. J. Surg.*, vol. 102, no. 3, pp. 182–193, 2015.

[82] M. G. Keane, K. Bramis, S. P. Pereira, and G. K. Fusai, "Systematic review of novel ablative methods in locally advanced pancreatic cancer," *World J. Gastroenterol. WJG*, vol. 20, no. 9, p. 2267, 2014.

[83] M. Nikfarjam and C. Christophi, "Interstitial laser thermotherapy for liver tumours," *Br. J. Surg.*, vol. 90, no. 9, pp. 1033–1047, 2003.

[84] T. Schröder, M. Castren-Persons, A. Lehtinen, and M. Taavitsainen, "Percutaneous interstitial laser hyperthermia in clinical use.," in *Annales Chirurgiae et Gynaecologiae*, 1994, vol. 83, no. 4, pp. 286–290.

[85] E. Schena, D. Tosi, P. Saccomandi, E. Lewis, and T. Kim, "Fiber optic sensors for temperature monitoring during thermal treatments: an overview," *Sensors*, vol. 16, no. 7, p. 1144, 2016.

[86] S. L. Jacques, "Optical properties of biological tissues: a review," *Phys. Med. Biol.*, vol. 58, no. 11, p. R37, 2013.

[87] S. Van Esser *et al.*, "Ultrasound-guided laser-induced thermal therapy for small palpable invasive breast carcinomas: a feasibility study," *Ann. Surg. Oncol.*, vol. 16, no. 8, p. 2259, 2009.

[88] H. Mumtaz *et al.*, "Laser therapy for breast cancer: MR imaging and histopathologic correlation.," *Radiology*, vol. 200, no. 3, pp. 651–658, 1996.

[89] S. H. Kim, S. E. Jung, H. L. Kim, S. T. Hahn, G. S. Park, and W. C. Park, "The potential role of dynamic MRI in assessing the effectiveness of high-intensity focused ultrasound ablation of breast cancer," *Int. J. Hyperth.*, vol. 26, no. 6, pp. 594–603, 2010.

[90] F. Wu *et al.*, "Extracorporeal high intensity focused ultrasound treatment for patients with breast cancer," *Breast Cancer Res. Treat.*, vol. 92, no. 1, pp. 51–60, 2005.

[91] H. Furusawa *et al.*, “The evolving non-surgical ablation of breast cancer: MR guided focused ultrasound (MRgFUS),” *Breast cancer*, vol. 14, no. 1, pp. 55–58, 2007.

[92] S. Li and P.-H. Wu, “Magnetic resonance image-guided versus ultrasound-guided high-intensity focused ultrasound in the treatment of breast cancer,” *Chin. J. Cancer*, vol. 32, no. 8, p. 441, 2013.

[93] F. Wu *et al.*, “A randomised clinical trial of high-intensity focused ultrasound ablation for the treatment of patients with localised breast cancer,” *Br. J. Cancer*, vol. 89, no. 12, pp. 2227–2233, 2003.

[94] M. S. Sabel, “Cryo-immunology: a review of the literature and proposed mechanisms for stimulatory versus suppressive immune responses,” *Cryobiology*, vol. 58, no. 1, pp. 1–11, 2009.

[95] J. G. Baust and A. A. Gage, “The molecular basis of cryosurgery,” *BJU Int.*, vol. 95, no. 9, pp. 1187–1191, 2005.

[96] G. C. Van Rhoon and P. Wust, “Introduction: non-invasive thermometry for thermotherapy,” *Int. J. Hyperth.*, vol. 21, no. 6, pp. 489–495, 2005.

[97] F. Fani, E. Schena, P. Saccomandi, and S. Silvestri, “CT-based thermometry: an overview,” *Int. J. Hyperth.*, vol. 30, no. 4, pp. 219–227, 2014.

[98] B. D. de Senneville, C. Mougenot, B. Quesson, I. Dragonu, N. Grenier, and C. T. W. Moonen, “MR thermometry for monitoring tumor ablation,” *Eur. Radiol.*, vol. 17, no. 9, pp. 2401–2410, 2007.

[99] D. Tosi, E. Schena, C. Molardi, and S. Korganbayev, “Fiber optic sensors for sub-centimeter spatially resolved measurements: Review and biomedical applications,” *Opt. Fiber Technol.*, vol. 43, no. March, pp. 6–19, 2018, doi: 10.1016/j.yofte.2018.03.007.

[100] A. D. Kersey *et al.*, “Fiber grating sensors,” *J. Light. Technol.*, vol. 15, no. 8, pp. 1442–1463, 1997.

[101] E. Udd and W. B. Spillman Jr, *Fiber optic sensors: an introduction for engineers and scientists*. John Wiley & Sons, 2011.

[102] S. Elayaperumal *et al.*, “Real-Time Estimation of 3-D Needle Shape and Deflection for MRI-Guided Interventions,” *IEEE/ASME Trans. Mechatronics*, vol. 15, no. 6, pp. 906–915, 2010, doi: 10.1109/tmech.2010.2080360.

[103] D. Polito *et al.*, “A Needlelike Probe for Temperature Monitoring During Laser Ablation Based on Fiber Bragg Grating: Manufacturing and Characterization,” *J. Med. Device.*, vol. 9, no. 4, p. 041006, 2015, doi: 10.1115/1.4030624.

[104] A. TO, “Biological evaluation of medical devices-Part 1: Evaluation and testing within a risk management process.” 2016.

[105] X. Bao and L. Chen, “Recent Progress in Distributed Fiber Optic Sensors,” *Sensors (Switzerland)*, vol. 12, no. 7, pp. 8601–8639, 2012, doi: 10.3390/s120708601.

[106] A. Barrias, J. R. Casas, and S. Villalba, “A review of distributed optical fiber sensors for civil engineering applications,” *Sensors*, vol. 16, no. 5, p. 748, 2016.

[107] B. J. Soller, D. K. Gifford, M. S. Wolfe, and M. E. Froggatt, “High resolution optical frequency domain reflectometry for characterization of components and assemblies,” *Opt. Express*, vol. 13, no. 2, pp. 666–674, 2005.

[108] E. G. Macchi *et al.*, “ Optical fiber sensors-based temperature distribution measurement in ex vivo radiofrequency ablation with submillimeter resolution ,” *J. Biomed. Opt.*, vol. 19, no. 11, p. 117004, 2014, doi: 10.1117/1.jbo.19.11.117004.

[109] P. Bettini, E. Guerreschi, and G. Sala, “Development and experimental validation of a numerical tool for structural health and usage monitoring systems based on chirped grating sensors,” *Sensors*, vol. 15, no. 1, pp. 1321–1341, 2015.

[110] D. Tosi, “Review and Analysis of Peak Tracking Techniques for Fiber Bragg Grating Sensors,” *Sensors*, vol. 17, no. 10, p. 2368, 2017.

[111] D. Tosi *et al.*, “Monitoring of radiofrequency thermal ablation in liver tissue through fibre Bragg grating sensors array,” *Electron. Lett.*, vol. 50, no. 14, pp. 981–983, 2014.

[112] T. Erdogan, “Fiber grating spectra,” *J. Light. Technol.*, vol. 15, no. 8, pp. 1277–1294, 1997.

[113] P. Roriz, L. Carvalho, O. Frazão, J. L. Santos, and J. A. Simões, “From conventional sensors to fibre optic sensors for strain and force measurements in biomechanics applications: A review,” *J. Biomech.*, vol. 47, no. 6, pp. 1251–1261, 2014.

[114] N. Wu, Y. Tian, X. Zou, Y. Zhai, K. Barringhaus, and X. Wang, “A miniature fiber optic blood pressure sensor and its application in in vivo blood pressure measurements of a swine model,” *Sensors Actuators B Chem.*, vol. 181, pp. 172–178, 2013.

[115] J. W. Arkwright *et al.*, “Design of a high-sensor count fibre optic manometry catheter for in-vivo colonic diagnostics,” *Opt. Express*, vol. 17, no. 25, pp. 22423–22431, 2009.

[116] P. Roriz, O. Frazão, A. B. Lobo-Ribeiro, J. L. Santos, and J. A. Simões, “Review of fiber-optic pressure sensors for biomedical and biomechanical

applications," *J. Biomed. Opt.*, vol. 18, no. 5, p. 50903, 2013.

[117] E. G. Macchi, M. Gallati, G. Braschi, A. Cigada, and L. Comolli, "Temperature distribution during RF ablation on ex vivo liver tissue: IR measurements and simulations," *Heat Mass Transf.*, vol. 51, no. 5, pp. 611–620, 2015.

[118] C. Bortolotto, S. Macchi, L. Veronese, R. Dore, F. Draghi, and S. Rossi, "Radiofrequency ablation of metastatic lesions from breast cancer," *J. Ultrasound*, vol. 15, no. 3, pp. 199–205, 2012.

[119] M. Froggatt, "Distributed measurement of the complex modulation of a photoinduced Bragg grating in an optical fiber," *Appl. Opt.*, vol. 35, no. 25, pp. 5162–5164, 1996.

[120] C. J. Gannon, C. R. Patra, R. Bhattacharya, P. Mukherjee, and S. A. Curley, "Intracellular gold nanoparticles enhance non-invasive radiofrequency thermal destruction of human gastrointestinal cancer cells," *J. Nanobiotechnology*, vol. 6, no. 1, pp. 1–9, 2008.

[121] C. J. Gannon *et al.*, "Carbon nanotube-enhanced thermal destruction of cancer cells in a noninvasive radiofrequency field," *Cancer Interdiscip. Int. J. Am. Cancer Soc.*, vol. 110, no. 12, pp. 2654–2665, 2007.

[122] K. K. Tanabe, S. A. Curley, G. D. Dodd, A. E. Siperstein, and S. N. Goldberg, "Radiofrequency ablation: the experts weigh in," *Cancer*, vol. 100, no. 3, pp. 641–650, 2004.

[123] C. H. Moran *et al.*, "Size-dependent joule heating of gold nanoparticles using capacitively coupled radiofrequency fields," *Nano Res.*, vol. 2, no. 5, pp. 400–405, 2009.

[124] P. Cherukuri, E. S. Glazer, and S. A. Curley, "Targeted hyperthermia using metal nanoparticles," *Adv. Drug Deliv. Rev.*, vol. 62, no. 3, pp. 339–345, 2010.

[125] K. P. Tamarov *et al.*, "Radio frequency radiation-induced hyperthermia using Si nanoparticle-based sensitizers for mild cancer therapy," *Sci. Rep.*, vol. 4, no. 1, pp. 1–7, 2014.

[126] R. Mooney, E. Schena, A. Zhumkhawala, K. S. Aboody, and J. M. Berlin, "Internal temperature increase during photothermal tumour ablation in mice using gold nanorods," in *2015 37th Annual International Conference of the IEEE Engineering in Medicine and Biology Society (EMBC)*, 2015, pp. 2563–2566.

[127] A. Ashokan *et al.*, "Biomineral nano-theranostic agent for magnetic resonance image guided, augmented radiofrequency ablation of liver tumor," *Sci. Rep.*, vol. 7, no. 1, pp. 1–15, 2017.

[128] J. Cardinal *et al.*, "Noninvasive radiofrequency ablation of cancer targeted by

gold nanoparticles," *Surgery*, vol. 144, no. 2, pp. 125–132, 2008.

[129] D. Ling and T. Hyeon, "Chemical design of biocompatible iron oxide nanoparticles for medical applications," *Small*, vol. 9, no. 9-10, pp. 1450–1466, 2013.

[130] S. Laurent *et al.*, "Magnetic iron oxide nanoparticles: synthesis, stabilization, vectorization, physicochemical characterizations, and biological applications," *Chem. Rev.*, vol. 108, no. 6, pp. 2064–2110, 2008.

[131] R. Hao, R. Xing, Z. Xu, Y. Hou, S. Gao, and S. Sun, "Synthesis, functionalization, and biomedical applications of multifunctional magnetic nanoparticles," *Adv. Mater.*, vol. 22, no. 25, pp. 2729–2742, 2010.

[132] R. E. Rosensweig, "Heating magnetic fluid with alternating magnetic field," *J. Magn. Magn. Mater.*, vol. 252, pp. 370–374, 2002.

[133] M. Salloum, R. H. Ma, D. Weeks, and L. Zhu, "Controlling nanoparticle delivery in magnetic nanoparticle hyperthermia for cancer treatment: experimental study in agarose gel," *Int. J. Hyperth.*, vol. 24, no. 4, pp. 337–345, 2008.

[134] A. Tomitaka, A. Hirukawa, T. Yamada, S. Morishita, and Y. Takemura, "Biocompatibility of various ferrite nanoparticles evaluated by in vitro cytotoxicity assays using HeLa cells," *J. Magn. Magn. Mater.*, vol. 321, no. 10, pp. 1482–1484, 2009.

[135] L. Gu, R. H. Fang, M. J. Sailor, and J.-H. Park, "In vivo clearance and toxicity of monodisperse iron oxide nanocrystals," *ACS Nano*, vol. 6, no. 6, pp. 4947–4954, 2012.

[136] H. Matsuki, T. Yanada, T. Sato, K. Murakami, and S. Minakawa, "Temperature-sensitive amorphous magnetic flakes for intratissue hyperthermia," *Mater. Sci. Eng. A*, vol. 181, pp. 1366–1368, 1994.

[137] I. Hilger, R. Hergt, and W. A. Kaiser, "Towards breast cancer treatment by magnetic heating," *J. Magn. Magn. Mater.*, vol. 293, no. 1, pp. 314–319, 2005.

[138] E. J. Patterson, C. H. Scudamore, D. A. Owen, A. G. Nagy, and A. K. Buczkowski, "Radiofrequency ablation of porcine liver in vivo: effects of blood flow and treatment time on lesion size.," *Ann. Surg.*, vol. 227, no. 4, p. 559, 1998.

[139] X. Zhang, H. Gu, and M. Fujii, "Effective thermal conductivity and thermal diffusivity of nanofluids containing spherical and cylindrical nanoparticles," *Exp. Therm. Fluid Sci.*, vol. 31, no. 6, pp. 593–599, 2007.

[140] J. Xu, B. Yu, M. Zou, and P. Xu, "A new model for heat conduction of nanofluids based on fractal distributions of nanoparticles," *J. Phys. D. Appl. Phys.*, vol. 39, no. 20, p. 4486, 2006.

[141] R. N. Pedro *et al.*, “Use of tumor necrosis factor–alpha-coated gold nanoparticles to enhance radiofrequency ablation in a translational model of renal tumors,” *Urology*, vol. 76, no. 2, pp. 494–498, 2010.

[142] R. Mooney, E. Schena, P. Saccomandi, A. Zhumkhawala, K. Aboody, and J. M. Berlin, “Gold nanorod-mediated near-infrared laser ablation: in vivo experiments on mice and theoretical analysis at different settings,” *Int. J. Hyperth.*, vol. 33, no. 2, pp. 150–159, 2017.

[143] X. Yang, “Science to Practice: Enhancing Photothermal Ablation of Colorectal Liver Metastases with Targeted Hybrid Nanoparticles,” *Radiology*, vol. 285, no. 3, pp. 699–701, 2017.

[144] C. Shundo, H. Zhang, T. Nakanishi, and T. Osaka, “Cytotoxicity evaluation of magnetite (Fe3O4) nanoparticles in mouse embryonic stem cells,” *Colloids Surfaces B Biointerfaces*, vol. 97, pp. 221–225, 2012.

[145] S. Korganbayev *et al.*, “Thermal profile detection through high-sensitivity fiber optic chirped Bragg grating on microstructured PMMA fiber,” *J. Light. Technol.*, vol. 36, no. 20, pp. 4723–4729, 2018.

[146] W. Liu *et al.*, “Determination of temperature and residual laser energy on film fiber-optic thermal converter for diode laser surgery,” *Comput. Assist. Surg.*, vol. 22, no. sup1, pp. 251–257, 2017.

[147] P. Saccomandi, E. Schena, and S. Silvestri, “Techniques for temperature monitoring during laser-induced thermotherapy: an overview,” *Int. J. Hyperth.*, vol. 29, no. 7, pp. 609–619, 2013.

[148] M. Pisco, A. Iadicicco, S. Campopiano, A. Cutolo, and A. Cusano, “Structured chirped fiber Bragg gratings,” *J. Light. Technol.*, vol. 26, no. 12, pp. 1613–1625, 2008.

[149] Y. Okabe, R. Tsuji, and N. Takeda, “Application of chirped fiber Bragg grating sensors for identification of crack locations in composites,” *Compos. Part A Appl. Sci. Manuf.*, vol. 35, no. 1, pp. 59–65, 2004.

[150] S. Yashiro, T. Okabe, N. Toyama, and N. Takeda, “Monitoring damage in holed CFRP laminates using embedded chirped FBG sensors,” *Int. J. Solids Struct.*, vol. 44, no. 2, pp. 603–613, 2007.

[151] C. Li, N. Chen, Z. Chen, and T. Wang, “Fully distributed chirped FBG sensor and application in laser-induced interstitial thermotherapy,” in *2009 Asia Communications and Photonics conference and Exhibition (ACP)*, 2009, vol. 2009, pp. 1–6.

[152] D. J. Webb, “Fibre Bragg grating sensors in polymer optical fibres,” *Meas. Sci. Technol.*, vol. 26, no. 9, p. 92004, 2015.

[153] A. R. Prado *et al.*, “Polymethyl methacrylate (PMMA) recycling for the production of optical fiber sensor systems,” *Opt. Express*, vol. 25, no. 24, pp. 30051–30060, 2017.

[154] K. Peters, “Polymer optical fiber sensors—a review,” *Smart Mater. Struct.*, vol. 20, no. 1, p. 13002, 2010.

[155] C. A. F. Marques, P. Antunes, P. Mergo, D. J. Webb, and P. André, “Chirped Bragg gratings in PMMA step-index polymer optical fiber,” *IEEE Photonics Technol. Lett.*, vol. 29, no. 6, pp. 500–503, 2017.

[156] R. Min, B. Ortega, and C. Marques, “Fabrication of tunable chirped mPOF Bragg gratings using a uniform phase mask,” *Opt. Express*, vol. 26, no. 4, pp. 4411–4420, 2018.

[157] X. Hu *et al.*, “BDK-doped core microstructured PMMA optical fiber for effective Bragg grating photo-inscription,” *Opt. Lett.*, vol. 42, no. 11, pp. 2209–2212, 2017.

[158] D. Sáez-Rodríguez, R. Min, B. Ortega, K. Nielsen, and D. J. Webb, “Passive and portable polymer optical fiber cleaver,” *IEEE Photonics Technol. Lett.*, vol. 28, no. 24, pp. 2834–2837, 2016.

[159] L. Dong, J. L. Cruz, L. Reekie, and J. A. Tucknott, “Fabrication of chirped fibre gratings using etched tapers,” *Electron. Lett.*, vol. 31, no. 11, pp. 908–909, 1995.

[160] W. Zhang and D. J. Webb, “Humidity responsivity of poly (methyl methacrylate)-based optical fiber Bragg grating sensors,” *Opt. Lett.*, vol. 39, no. 10, pp. 3026–3029, 2014.

[161] H. Liu, H. Liu, G. Peng, and T. W. Whitbread, “Tunable dispersion using linearly chirped polymer optical fiber Bragg gratings with fixed center wavelength,” *IEEE photonics Technol. Lett.*, vol. 17, no. 2, pp. 411–413, 2005.

[162] A. Sophie *et al.*, “Thermal effects on the photoelastic coefficient of polymer optical fibers,” *Opt. Lett.*, vol. 41, no. 11, pp. 2517–2520, 2016.

[163] A. H. Hartog, A. P. Leach, and M. P. Gold, “Distributed temperature sensing in solid-core fibres,” *Electron. Lett.*, vol. 21, no. 23, pp. 1061–1062, 1985.

[164] A. Masoudi, M. Belal, and T. P. Newson, “A distributed optical fibre dynamic strain sensor based on phase-OTDR,” *Meas. Sci. Technol.*, vol. 24, no. 8, p. 85204, 2013.

[165] N. M. P. Pinto, O. Frazao, J. M. Baptista, and J. L. Santos, “Quasi-distributed displacement sensor for structural monitoring using a commercial OTDR,” *Opt. Lasers Eng.*, vol. 44, no. 8, pp. 771–778, 2006.

[166] I. L. Fabelinskii, *Molecular scattering of light*. Springer Science & Business

Media, 2012.

[167] D. K. Gifford *et al.*, “Swept-wavelength interferometric interrogation of fiber Rayleigh scatter for distributed sensing applications,” in *Fiber Optic Sensors and Applications V*, 2007, vol. 6770, p. 67700F.

[168] W. Blanc *et al.*, “Fabrication of rare earth-doped transparent glass ceramic optical fibers by modified chemical vapor deposition,” *J. Am. Ceram. Soc.*, vol. 94, no. 8, pp. 2315–2318, 2011.

[169] W. Blanc *et al.*, “Reconsidering nanoparticles in optical fibers,” in *Optical Components and Materials XVII*, 2020, vol. 11276, p. 112760S.